February 2021

Application of Compound-specific Stable Isotopes and Molecular Biomarkers to Paleoclimatic and Paleoecological Reconstructions

Mingqiu Hou
Louisiana State University and Agricultural and Mechanical College

APPLICATION OF COMPOUND-SPECIFIC STABLE ISOTOPES AND MOLECULAR BIOMARKERS TO PALEOCLIMATIC AND PALEOECOLOGICAL RECONSTRUCTIONS

A Dissertation

Submitted to the Graduate Faculty of the
Louisiana State University and
Agricultural and Mechanical College
in partial fulfillment of the
requirements for the degree of
Doctor of Philosophy

in

The Department of Geology and Geophysics

by
Mingqiu Hou
B.S., Missouri University of Science and Technology, 2016
May 2021

Acknowledgments

I would like to express my most profound acknowledgment to my family, who has believed in me more than I do myself. And for my husband Shuai Shao, thanks for your wise counsel and sympathetic ear. Without your unconditional love and encouragement, I would not have completed this work.

Thank you to my Ph.D. advisor, Dr. Guangsheng Zhuang, who has devoted a lot of time and effort to mentor me and has been willing and enthusiastic to support me in any way he could throughout the research project. I would like to acknowledge my committee Dr. Huiming Bao and Dr. Brooks B. Ellwood and Dean's representative Dr. Slawo Lomnicki for their thoughtful comments and recommendations on my research.

I also would like to thank my undergraduate advisor Wan Yang for his guidance and encouragement on my academic pursuit.

I would like to thank Minghao Wu, Yongbo Peng, Hui Yang, Clay Doremus, and Amber Ellwood for their laboratory assistance.

I would like to acknowledge the financial support from the US National Science Foundation (NSF) Grant EAR 2022282 to G. Zhuang and teaching assistant grants from Geology and Geophysics department in Louisiana State University.

Table of Contents

Acknowledgments ii

Abstract v

Chapter 1. Introduction 1
1.1. Last Glacial Climate in the Qaidam Basin: Implications for Westerlies-monsoon Interactions 1
1.2. Hemispherical Temperature Asymmetry Shifting the Atlantic ITCZ Northward During the Eocene-Oligocene Transition 2
1.3. Effects of Mountain Uplift and Global Cooling on the Paleoclimatic and Paleoecological Evolution in the Northern Tibetan Plateau 3

Chapter 2. Methodology 5
2.1. Long-chain *n*-alkanes Synthesized by Terrestrial Higher-plants . . 5
2.2. Compound Specific Carbon Isotope as Paleoecological Proxy . . . 6
2.3. Compound Specific Hydrogen Isotope as Paleohydrological Proxy 7
2.4. Organic Lipid Extraction 10
2.5. Compound Specific Carbon and Hydrogen Isotope Analysis . . . 11
2.6. Unsaturated Alkenone Analysis 12
2.7. Glycerol Dialkyl Glycerol Tetraethers (GDGT) Analysis 12

Chapter 3. Profiling Interactions Between the Westerlies and Asian Summer Monsoons since 45 ka: Insights from Biomarker, Isotopes, and Numerical Modeling Studies in the Qaidam Basin 14
3.1. Introduction 14
3.2. Geological Setting and Modern Climate 19
3.3. Materials and Methods 22
3.4. Results and Discussions 31
3.5. Conclusions 45

Chapter 4. Hemispherical Temperature Asymmetry Shifting the Atlantic ITCZ Northward During the Eocene-Oligocene Transition 47
4.1. Introduction 47
4.2. Lithostratigraphy, Age Constraints, and Modern Climate 50
4.3. Methods and Materials 56

4.4. Results and Discussions 69
4.5. Conclusions 86

Chapter 5. Isotopic Fingerprints of Mountain Uplift and Global Cooling in Paleoclimatic and Paleoecological Records from the Northern Tibetan Plateau 87
5.1. Introduction 87
5.2. Geological Background and Modern Climate 90
5.3. Methods and Materials 95
5.4. Results 100
5.5. Discussions 102
5.6. Conclusions 115

Chapter 6. Conclusions 116

Bibliography 119

Vita 137

Abstract

Compound-specific stable isotope analysis and biomarker-based paleothermometry have been increasingly applied to for paleoclimatic and paleoecological studies. The first project aims to reconstruct the paleoclimate in the Qaidam Basin during the last glacial period. Qaidam Basin in the Northern Tibetan Plateau is a critical eolian factory located at a unique geographic location that links the Westerlies and the Asian summer monsoons. However, how the interactions of two climatic systems influence the paleohydrology that in turn impacts the eolian production in the Qaidam Basin has been seldom explored. Our results show that the Westerlies and Asian summer monsoons alternately controlled the Qaidam Basin's climate in response to precessional forcing during the late Pleistocene. The second project studies the hydrological change in the Gulf of Mexico (GoM) region during the "greenhouse" to "icehouse" transition near the Eocene-Oligocene boundary (33.9 Ma). The geological evidence and climate model proposes that cooling in the Northern Hemisphere was delayed and weaker than in the Southern Hemisphere during the climate transition, which intensifies the Atlantic Meridional Overturning Circulation, increased precipitation in low-latitudes, and subsequent drawdown of atmospheric carbon dioxide during weathering processes. However, there are

no quantitative constraints on variations in low latitude precipitation during this interval. Our paleoclimate data from the GoM through the climate transition interval show increased precipitation up to 50%, supporting the CO_2-weathering feedback hypothesis and highlighting the low-high latitude climate and atmospheric-oceanic connection. The third project focuses on the post-middle Miocene paleoclimate and ecological change in the northern Tibetan Plateau (TP). The relative importance of high topography on the TP and the global cooling in regional climate and ecology in Central Asia has been a long-standing debate. Our carbon isotope records from Hexi Corridor, northern TP show that (1) global cooling plays a primary role in the decline in C_4 plant contribution in northern Tibetan Plateau since the ~14.8 Ma, and (2) the disparate regional climate patterns in northern Tibetan Plateau since ~12 Ma are owing to the uplift of plateau.

Chapter 1. Introduction

Over the past few decades, Liqid biomarkers from terrestrial higher plants have been increasingly used to study the paleoclimate, biochemical processes, and fossil fuel exploration. The stable carbon and hydrogen isotopic compositions of *n*-alkane derived from leaf wax lipid bears information about environment and ecology (such as photosynthetic pathways of C_3 and C_4 plant on CO_2 fixation, hydrology, and paleotemperature), which make it a critical tool in studying earth history, especially paleoclimate and tectonic process. My research shows the application of molecular biomarker approaches for studying paleoclimate and paleoecology within various geological periods and in vast regions, including Qaidam Basin and Hexi Corridor in northwestern China and the Gulf of Mexico in the United States.

1.1. Last Glacial Climate in the Qaidam Basin: Implications for Westerlies-monsoon Interactions

The Qaidam Basin is situated in a critical site that links the Westerlies and East Asian summer monsoons and hence provides a superb example for studying the interactions between two atmospheric systems in the Northern Hemisphere. A common view regarding the paleoclimate over the glacial-interglacial cycles in Asia is that climate was warm and humid when the Asian summer monsoon was strong in interglacial periods and cold and dry when

the westerlies were dominant in the glacial periods. However, sedimentary evidence indicated that paleolakes in the Tibetan Plateau, including the Qaidam Basin, were expanded with a much higher lake level (> 100 meters) than the present during the last glacial period. I am using geochemistry proxies to reconstruct hydrology and temperature history in the Qaidam Basin during the last glacial. The study will advance our knowledge of the interaction between the Westerlies and the East Asian summer monsoons and their influences on regional paleoclimate patterns since the late Pleistocene.

1.2. Hemispherical Temperature Asymmetry Shifting the Atlantic ITCZ Northward During the Eocene-Oligocene Transition

Marine sedimentary and geochemistry evidence indicate profound climate change during the Eocene-Oligocene transition, including a drop in atmospheric CO_2, cooling at high-latitude, and Antarctic glaciation. On the other hand, terrestrial paleoclimate data show a various climate responses range from aridification, stable hydrological condition, to increasing seasonality. However, few studied the connection between terrestrial and oceanic responses to this climate event. In the Gulf of Mexico region, terrestrial and oceanic records show divergent responses. Some studies suggested that the sea surface temperature in the Gulf of Mexico decreases about 3 °C during this transition, while others reported no temperature or hydrological change

on land. The discordant observations between climate records challenged our understanding of the connection among ocean, continents, and atmosphere. Hence, a synthesized record that could link terrestrial to marine realms is greatly needed. Here, I am generating two datasets of both terrestrial and oceanic records from a core drilled in Mississippi. Carbon isotopes ($\delta^{13}C_{n\text{-alk}}$) and hydrogen isotopes ($\delta^{13}C_{n\text{-alk}}$) of leaf wax long-chain *n*-alkanes are used to reconstruct hydrological and ecological systems in the terrestrial Gulf Coast. I also applied TEX_{86} paleothermometry to reconstruct surface temperature in the Gulf of Mexico.

1.3. Effects of Mountain Uplift and Global Cooling on the Paleoclimatic and Paleoecological Evolution in the Northern Tibetan Plateau

Post-middle Miocene climate and ecological changes in the northern Tibetan Plateau has been attributed to tectonic uplift and global climate change. Whether the uplift of the Tibetan Plateau or the global cooling predominantly drove the climatic and ecological changes has been a long-standing debate. Paleoclimate data from the northern Tibetan Plateau and surrounding areas show diverse climatic patterns, including (1) long-term drying event associated with global cooling after the mid-Miocene Climate Optimum (MMCO) and (2) a dynamic climate alternating between wet and dry conditions after the obtainment of high elevations at ca. 12 Ma. A decrease in C_4 plant propo-

tion in the northern Tibetan Plateau during the late Miocene has been correlated with both tectonic uplift of Tibetan Plateau and post-middle Miocene global cooling. To untangle the complex influence of global climate change versus the tectonism on climate in the northern Tibetan Plateau, we studied carbon isotopes ($\delta^{13}C_{n\text{-alk}}$) of leaf wax long-chain *n*-alkanes and oxygen isotopes ($\delta^{18}O$) of three stratigraphic successions (ca. 16 Ma to 2 Ma) in Hexi Corridor (foreland basin) and compare with paleoclimate records in the Qaidam Basin (intermontane basin). We want to establish the basin-wide paleoecology and paleoclimate records in the Hexi Corridor and understanding the linkage between climate and ecology. By comparing the paleoecology and paleoclimate records in the foreland and intermountain basins, we will be able to differentiate the basin isolation signal related to the tectonic uplift. With intra- and inter-basinal comparisons, we will advance our understanding the relative role tectonism and global cooling on regional climatic and ecological evolutions.

Chapter 2. Methodology

2.1. Long-chain *n*-alkanes Synthesized by Terrestrial Higher-plants

Leaf epicuticular wax is a layer of cuticle coated on plants' leaf surfaces that protect their leaves from external influences such as surface wetting, water loss, and ultraviolet light (Eglinton and Hamilton, 1967b; Kolattukudy, 1970). Leaf wax synthesized by terrestrial higher plants are composed of mixtures of long, straight-chain normal alkanes (*n*-alkanes) with 21-37 carbon atoms (Eglinton and Hamilton, 1967b). The strong and covalent carbon-hydrogen bonds in CH_2 and CH_3 groups of *n*-alkane compounds are barely exchangeable under 120°C (Sessions et al., 2004; Schimmelmann et al., 2006), making them an ideal approach in studying vegetational and hydrological histories. These *n*-alkane compounds are characterized by odd-over-even carbon-number predominance, also expressed as carbon preference index (CPI), for example, with higher abundances of *n*-C_{27-33} compounds than *n*-C_{26-32} compounds. The long chain *n*-alkanes are ubiquitously preserved in fluvial, lacustrine, marine and eolian sediments, where they serve as indicators of paleoclimate and vegetation cooperate in their biosynthetic processes (Hayes, 2001; Eglinton and Eglinton, 2008).

2.2. Compound Specific Carbon Isotope as Paleoecological Proxy

The $\delta^{13}C_{n\text{-alk}}$ values of leaf wax *n*-alkanes are determined by photosynthetic pathways, e.g. C_3 or C_4 biosynthetic pathways, carbon isotopic composition of atmospheric CO_2 and climatic factors (e.g. water supply) that controls plant's stomata conductance (O'Leary, 1988; Farquhar et al., 1989). C_3 plants comprise various species, including trees, shrubs and grasses, which uptake CO_2 through the most primitive biosynthetic pathways, known as Calvin-Benson cycle. C_4 plants are less abundant and are typically grasses and sedges distributed in tropical areas. C_4 photosynthesis involve Hatch-Slack pathway which firstly produce a four-carbon acid, oxaloacetate in the mesophyll cell that ultimately convert back to CO_2 used in Calvin-Benson cycle in the bundle-sheath cells (Slack and Hatch, 1967; Tipple and Pagani, 2007). Thrifty usage of CO_2 during photosynthesis allows C_4 plants adapt better to limited pCO_2, higher temperature and drier habitats than the C_3 plants. Different photosynthetic pathways result in distinct isotopic composition and distribution of *n*-alkanes in C_3 and C_4 plants. $\delta^{13}C_{n\text{-alk}}$ values of C_3 plant rang from -19 ‰ to -36 ‰ with peak values -34 % at $n\text{-}C_{31}$, while C_4 plants on average are between -8 ‰ and -16 ‰ with maxima $\delta^{13}C_{n\text{-alk}}$-22 ‰ at $n\text{-}C_{31}$ (Cerling and Harris, 1999; Eglinton and Eglinton, 2008). Hence,

these unique distribution of *n*-alkane $\delta^{13}C_{n\text{-alk}}$ in C_3 and C_4 plants have been utilized as a proxy for vegetation dominance (Ehleringer et al., 1997; Freeman and Colarusso, 2001; Edwards et al., 2010).

2.3. Compound Specific Hydrogen Isotope as Paleohydrological Proxy

The Compound specific hydrogen isotopes of plant waxes preserved in sediments have been suggested to archive the isotopic composition of meteorological water (Fig. 2.1) (Estep and Hoering, 1980; Sachse et al., 2012). δ^2H values of water vapor and precipitation varies over time and space. Their variability can be explained by Rayleigh distillation processes during evaporation and precipitation (Dansgaard, 1964; Craig and Gordon, 1965). When seawater evaporates, the water vapor with lighter isotope ($^1H_2\,^{16}O$) has higher vapor pressure and evaporates faster than $^1H^2H^{16}O$, thus the water vapor is depleted in heavy isotope (^2H). When water vapor condenses, heavier isotope leaves faster to form precipitation and result in rain water enriched in ^2H. Environmental factors control on spatial and temporal variability of precipitation δ^2H values are concluded as following:

1. Amount effect: the δ^2H values is associated with amount of precipitation in the tropical areas, where large precipitation rate leads to strong depletion in ^2H of rain water.

2. Temperature effect: In the continental interiors and high latitude regions where temperature varies distinctly through the seasons, precipitation

δ^2H values are strongly correlated with temperature. As equilibrium isotopic fractionation factor (α) is determined by temperature, decrease in temperature enlarges the fractionation of ^2H between vapor and condensate, and results in lower δ^2H values.

3. Altitude effect: as the water vapor orographically uplifted preferentially loss of heavier isotope (^2H) impels the precipitation to lower δ^2H values along elevation

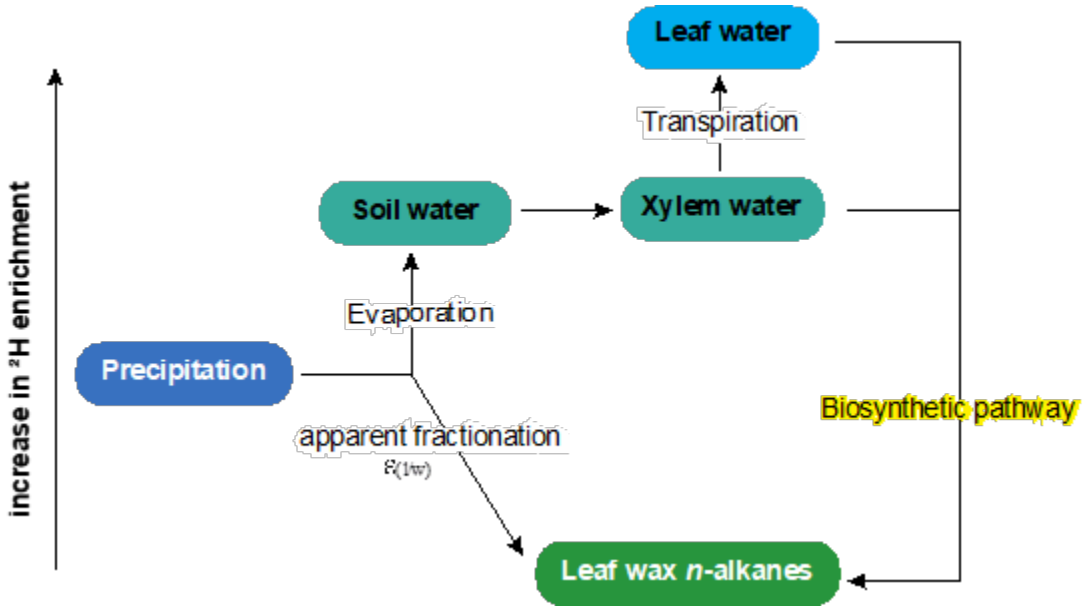

Figure 2.1. A summary of processes affecting hydrogen isotopic composition of leaf wax *n*-alkanes from terrestrial plants (modified from Sachse et al., 2012). Arrow points to the direction of ^2H enrichment. $\varepsilon_{(l/w)}$ denotes isotopic fractionation between lipids and source water.

The major water source of terrestrial plants is soil water, which ultimately comes from precipitation. Hence, isotopic composition of soil-water largely reflects that of precipitation. The fractionation between leaf wax lipids and precipitation water can be expressed as apparent fractionation $\varepsilon_{(l/w)}$. The

flow chart summarizes the factors control the δ^2H values of leaf wax *n*-alkanes by tracing the hydrogen from the water source into the organic compound (Fig. 2.1). $\varepsilon_{(l/w)}$ is mainly determined by three major factors: soil water evaporation, xylem water transpiration and biosynthetic fractionation (Sachse et al., 2012). Evaporation and transpiration enrich ^2H, while biosynthetic fractionation decrease the ^2H enrichment. There is no typical fractionation occurs during water uptake by roots, thus isotopic composition of water in roots and stems reflect isotopic signature of water incorporated in biosynthesis (Farquhar et al., 2007). However, the isotopic components of meteoric water or soil water (δ^2H) are different from that within plant leaf, since the environmental water used by plant during biosynthesis are determined by a series of environmental and physiological parameters, such as evapotranspiration of leaf. Evaporation and transpiration enrich the heavy isotope in surface waters since lighter isotopologs diffuse faster to the air. The transpiration rate is affected by temperature, relative humidity, and isotopic composition of the water vapor surrounding the leaf (Flanagan and Ehleringer, 1991; Kahmen et al., 2008). Fractionation during biosynthetic pathways can be influenced by life-form and photosynthetic pathway. For example, shrubs are isotopically enriched in heavier isotopes than trees and forbs; δ^2H of C_4 monocotyledon are 15‰ heavier

than the C_3 monocotyledon (Smith and Freeman, 2006).

2.4. Organic Lipid Extraction

All samples are grinded into small fragments and freeze dried for 48 hours before organic compound extraction. Total lipids were extracted with Soxhlet extractor using dichloromethane (DCM)/methanol 2:1 (v/v) for 48 hours. Total lipid extracts (TLE) were evaporated with a stream of purified nitrogen until dry. organic compounds in TLE were separated into apolar, intermediate and polar fractions using pipette column filled with ca. 0.5 grams activated silica gel and eluted with 2 ml hexane, 4 ml DCM and 4 ml methanol sequentially.

n-Alkanes contained in apolar fractions were re-dissolved into 1500 µL of hexane. *n*-Alkanes abundances were determined using a Thermal Trace 1310 Gas Chromatography (GC)-flame ionization detector (FID) fitted with a programmable-temperature vaporization (PTV) injector and TG-1MS column (60 m long, 0.25 mm i.d., 0.25 µm film thickness). Samples were carried by helium at a rate of 2 ml/min. GC oven temperature was ramped from 60 °C (holding for 1 min) to 320 °C at 15 °C/min (holding for 20 min). Individual *n*-alkanes were determined by comparing the elution time with a reference standard (Mix A6, Schimmelmann, Indiana University Bloomington).

2.5. Compound Specific Carbon and Hydrogen Isotope Analysis

Measurements of compound-specific carbon isotope values were measured by GC-combustion (C)-IRMS. Prior to the analysis, all samples are diluted by hexane in proper concentration. GC-C-IRMS are performed with a Thermo Trace 1310 coupled to a Thermo Delta V Advantage isotope ratio mass spectrometer (IRMS) interfaced with GC-C combustion reactor and a Trace Isolink interface. Compounds were separated on the GC through a TG-5MS column (30 m long, 0.25 mm i.d., 0.25 μm film thickness) column. Compounds were separated on the GC with a temperature programed from 60 °C (held for 2 min) to 170 °C at 14 °C/min, to 300 °C at 3 °C/min, and then to 320 °C at 14 °C/min with an isothermal holding of 5 mins.

Hydrogen isotope analysis were performed with a Trace 1310 coupled to a Thermo Delta V Advantage isotope ratio mass spectrometer (IRMS) interfaced with high temperature conversion reactor and a Trace Isolink interface. GC column and carrier flow conditions were identical to above. Compounds were separated on the GC with a temperature program from 60 °C (held for 1 min) to 170 °C at 14 °C/min, to 300 °C at 3 °C/min, and then to 325 °C at 14 °C/min with an isothermal holding of 10 mins. H3+ factor was measured daily before hydrogen isotopic analysis.

2.6. Unsaturated Alkenone Analysis

The alkenone contents have been identified according to protocols of *Emiliania huxleyi* and *Gephyrocapsa oceanica* (Volkman et al., 1980; Volkman et al., 1995; Sawada et al., 1996). Ketone fraction was analyzed on Thermal Trace 1310 Gas Chromatography (GC)-flame ionization detector (FID) fitted with a programmable-temperature vaporization (PTV) injector and TG-1MS column (60 m long, 0.25 mm i.d., 0.25 µm film thickness). Samples were carried by helium at a rate of 2 ml/min. GC oven temperature was ramped from 60 °C (holding for 1 min) to 280 °C at 20 °C/min and then to 325 °C at 2 °C/min with isothermal holding for 25 minutes. Relative abundances of $C_{37:4}$, $C_{37:3}$ and $C_{37:2}$ alkenones were measured and subsequently used in the conversion to temperature.

2.7. Glycerol Dialkyl Glycerol Tetraethers (GDGT) Analysis

TEX_{86} thermometry is founded on the expression of cyclopentane moieties of archaeal membrane lipids, glycerol dialkyl glycerol tetraethers (GDGT), primarily produced by Thaumarchaeota. The methanol fraction containing GDGTs is purified through a column of activated alumina dissolved in dichloromethane/methanol (1:1, v/v), dried under pure N_2 stream, dissolved in an azeotrope of hexane/isopropanol (99:1, v/v), filtered through 0.7 µm

glass microfiber filter. GDGTs were analyzed on 1290series UPLC system that was coupled to an Agilent 6530 qTOF mass spectrometer through an Aglient jet stream dual electrospray ionization (AJS-ESI) interface, following the methodology of Liu et al. (2019).

Chapter 3. Profiling Interactions Between the Westerlies and Asian Summer Monsoons since 45 ka: Insights from Biomarker, Isotopes, and Numerical Modeling Studies in the Qaidam Basin

3.1. Introduction

The Westerlies and the Asian summer monsoons play essential roles in controlling the paleoclimate in Central Asia. The Qaidam Basin is situated in a critical climate region that separates the Westerlies-influenced arid Central Asia to the west and the Asian summer monsoons-controlled East Asia to the east (Fig. 3.1). As one of the world's highest and driest places with extremely high ratios of evaporation (>3000 mm) versus precipitation (<180-220 mm) (Tian et al., 2001; Yao et al., 2013), the Qaidam Basin potentially contributes a significant amount of eolian dust transported by Westerlies to the down-wind areas in the Chinese Loess Plateau (Kapp et al., 2011; Pullen et al., 2011; Lin et al., 2020) and North Pacific (Li et al., 2011a). The unique geographical location of the Qaidam Basin makes its hydrological changes sensitive to the relative strength of the Westerlies and Asian summer monsoons. However, the interactions between two climate systems and the influences on the eolian dust production in the Qaidam Basin at orbital- and millennial-scales are not well understood.

Paleoclimate in Central Asia was thought to have alternated between

the warm-humid interglacial periods with the strong influence of the Asian summer monsoons and the cold-dry glacial periods with the dominant influence from the Westerlies (An et al., 2012). This alternating climate pattern has been manifested by the loess/paleosol sedimentary sequences from Tianshan in Central Asia (Li et al., 2016) and on the Chinese Loess Plateau in East Asia (Kukla and An, 1989; An et al., 1990; Porter and An, 1995). In the Qaidam Basin, sedimentary records and modeling studies reveal that the cold-dry climate during the glacial and stadial periods results in subaerial exposure and intensive erosion of lacustrine strata when the main axis of the Westerly jet shifts toward the equator (Kapp et al., 2011; Pullen et al., 2011; Heermance et al., 2013; Rohrmann et al., 2013). High eolian fluxes recorded in sedimentary successions, ranging from Central Asia to the North Pacific, indicate strong wind erosion associated with Westerlies (Hovan et al., 1991; An et al., 2012; Li et al., 2016). Isotope proxy and pollen studies from the northern Tibetan Plateau suggest that precipitation decreased during the Last Glacial Maximum (LGM) (Wang et al., 2014; Thomas et al., 2016).

Paleoshoreline records from the Qaidam Basin, particularly freshwater mollusks in lacustrine strata, indicate the expansion of paleo-lakes from ca. 30-40 ka to ca. 15 ka (Li and Zhu, 2001; Zhang et al., 2008). This lake expan-

sion coincides with the interglacial temperature conditions during the late Marine Isotope Stage 3 (MIS 3), which is supported by the Guliya ice-core $\delta^{18}O$ record and the pollen record from the adjacent Qilian Shan (Thompson et al., 1997; Herzschuh et al., 2006). There are disparate interpretations of the highstand or lake expansion through the late MIS 3. One interpretation invokes the inland penetration of Asian summer monsoons (Shi et al., 2001). The other attributes the increase of precipitation during the late MIS 3 to the strong Westerlies circulation (Yang et al., 2004).

Previous studies using geochemical, biomarker, and isotopic proxies and numerical simulations have provided insights into the variations of the Westerlies and the Asian summer monsoons and their influences on the paleohydrology, but most studies focus on either the core area of the Westerlies to the further west (e.g., speleothem from Kesang Cave and Ton Cave in the Tian Shan and lacustrine records from the Lake Karakul in Pamirs, Fig. 3.1) (Cheng et al., 2016; Aichner et al., 2019) or the Asian summer monsoons-influenced regions to the east (e.g., lacustrine records from Lake Qinghai) (An et al., 2012; Thomas et al., 2016). Despite active research that has reconstructed the paleoclimatic evolution in northern Tibetan Plateau during the Holocene (An et al., 2012; Thomas et al., 2016), studies of past climate in the Qaidam Basin

on orbital timescales (e.g., precession cycles) are not available. In this study, we aim to resolve how and at what timescale the paleoclimate in the Qaidam Basin responds to the relative strength of the Westerlies and the Asian summer monsoons. We focus on the three linked questions: (i) Does the high summer insolation period (corresponding to the Marine Isotope Stage 3) cause strong summer monsoons with high temperatures and increased precipitation? (ii) Does the transition from high to low summer insolation into the LGM weaken the summer monsoons? (iii) Is the evaporation reduced during the LGM relative to the present? To answer these questions, we conduct an integrated study using organic biomarker-proxies coupled with climate modeling to examine the paleoclimate history in the Qaidam Basin during the last glacial period. We apply hydrogen isotopic analysis to terrestrial higher-plant n-alkanes and use the locally calibrated alkenone-based paleothermometry (U^{K}_{37}) to lacustrine sediments recovered from a drill core in the western Qaidam Basin. Reconstructed paleoclimate history, along with numerical modeling studies using Community Earth System Model (CESM) version 1.3, is compared with the Holocene regional paleoclimatic proxy records in the Asian summer monsoons- and Westerlies-dominated areas.

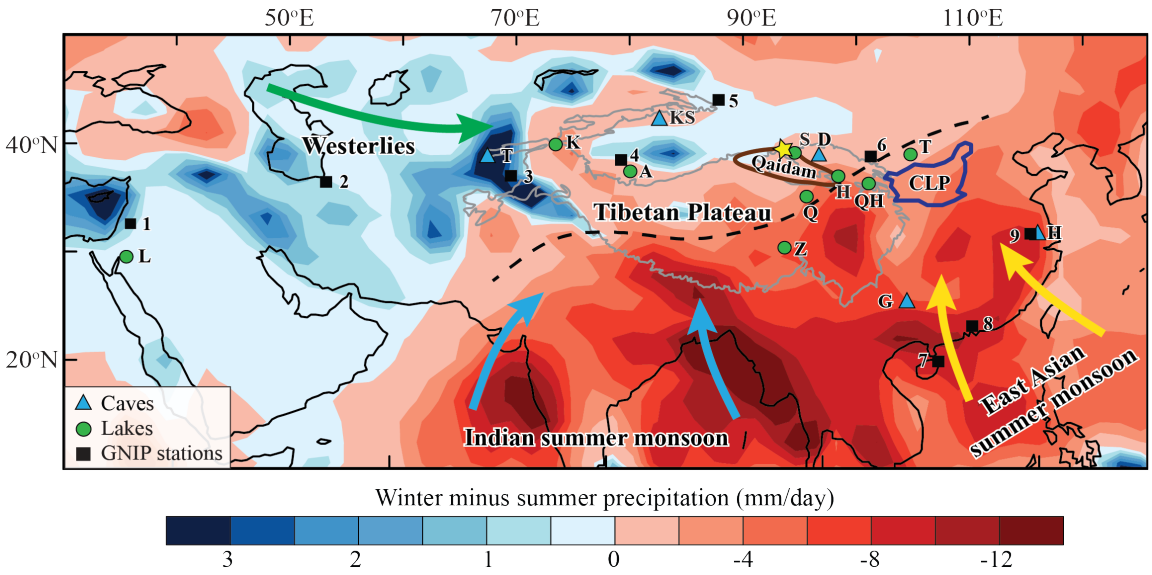

Figure 3.1. 30 years (1981-2010) record of winter (December-January-February) minus summer (June-July-August) precipitation (mm/day). Blue color represents greater precipitation in winter (December-January-February), while red color indicates greater precipitation in summer (June-July-August). Data are derived from NCEP Reanalysis provided by NOAA ESRL PSD at Colorado, Boulder, USA (https://www.esrl.noaa.gov/psd/data). The gray line outlines the 3000 m-contour on the Tibetan Plateau and surrounding mountain (adapted from Li et al., 2018). The Qaidam Basin (brown outline), core site (yellow star), and the Chinese Loess Plateau (CLP; dark blue outline) are noted. Arrows highlight the moisture transport via the Westerlies (green), Indian summer monsoon (blue), and East Asian summer monsoon (yellow). The black dashed line represents the modern boundary between the Asian summer monsoons (East Asian and Indian summer monsoons) and the Westerlies. Blue triangles are the locations of isotope reconstruction of paleometeoric waters in the Hulu (H) (Wang et al., 2008), Dongge (G) (Dykoski et al., 2005), Ton (T), and Kesang (KS) (Cheng et al., 2012) caves and the Dunde Ice core (D) (Thompson et al., 1989). Green circles denote the lakes and paleo-lakes discussed in the text: Lake Qinghai (QH) (Hou et al., 2016), Lake Sugan (S) (He et al., 2013; Wang et al., 2013), Lake Keluke (H) (Rao et al., 2014), Tengger Desert (T), Qarhan (Q), Zabuye (Z), Aksayqin (A) (Yu et al., 2003), Karakul (K) (Aichner et al., 2019) and Lisan (L) (Bartov et al., 2003). Black squares indicate the Global Network of Isotope in Precipitation (GNIP) meteorological stations (IAEA/WMO, 2006) (numbers are correlated with stations in Fig. S1).

3.2. Geological Setting and Modern Climate

The Qaidam Basin is an intermontane basin at the northern margin of Tibetan Plateau. It is bounded by the Qilian Shan fold-thrust belt to the northeast, the Altun Shan range to the northwest, and the East Kunlun Shan range to the south (Fig. 3.2a). The Qaidam basin is ca. 700 km in length with a maximum width of about 300 km, occupying $\sim$ 120,000 km^2 with a mean elevation of 2700 m (Chen and Bowler, 1986). The geomorphology of the Qaidam Basin is characterized by widespread eolian features, including migrating dunes, deflecting pans, and mega-yardangs, due to extremely arid climate and severe wind erosion (Goudie, 2007). The lake system in the modern Qaidam Basin comprises more than 20 discrete salt lakes and playas, occupying a quarter of the total basin area (Chen and Bowler, 1986).

In the Qaidam Basin, more than 90 % of the annual rainfall occurs during spring and summer seasons (Tian et al., 2001), with the average temperatures for January and July and the mean annual temperature being -12, 16, and 2 °C, respectively (Zhang et al., 2008) (Fig. 3.2b). Water vapor is transported mainly by Westerlies with a substantial amount coming from local recycling (Bershaw et al., 2012; Li and Garzione, 2017); moisture from the Asian summer monsoons reaches the eastern part of the basin (Araguás-Araguás et

al., 1998; Tian et al., 2001; Yao et al., 2012; Caves et al., 2015). We use HYbrid Single-Particle Lagrangian Integrated Trajectory Model (HYSPLIT) to track the air masses of the study area in the western Qaidam Basin and a selected site in the eastern Qaidam Basin, respectively. The modeled air masses indicate that the eastern Qaidam Basin receives moisture from Asian summer monsoons during summer and from the Westerlies for other seasons. The western Qaidam Basin is influenced by Westerlies all year round (Fig. 3.2c).

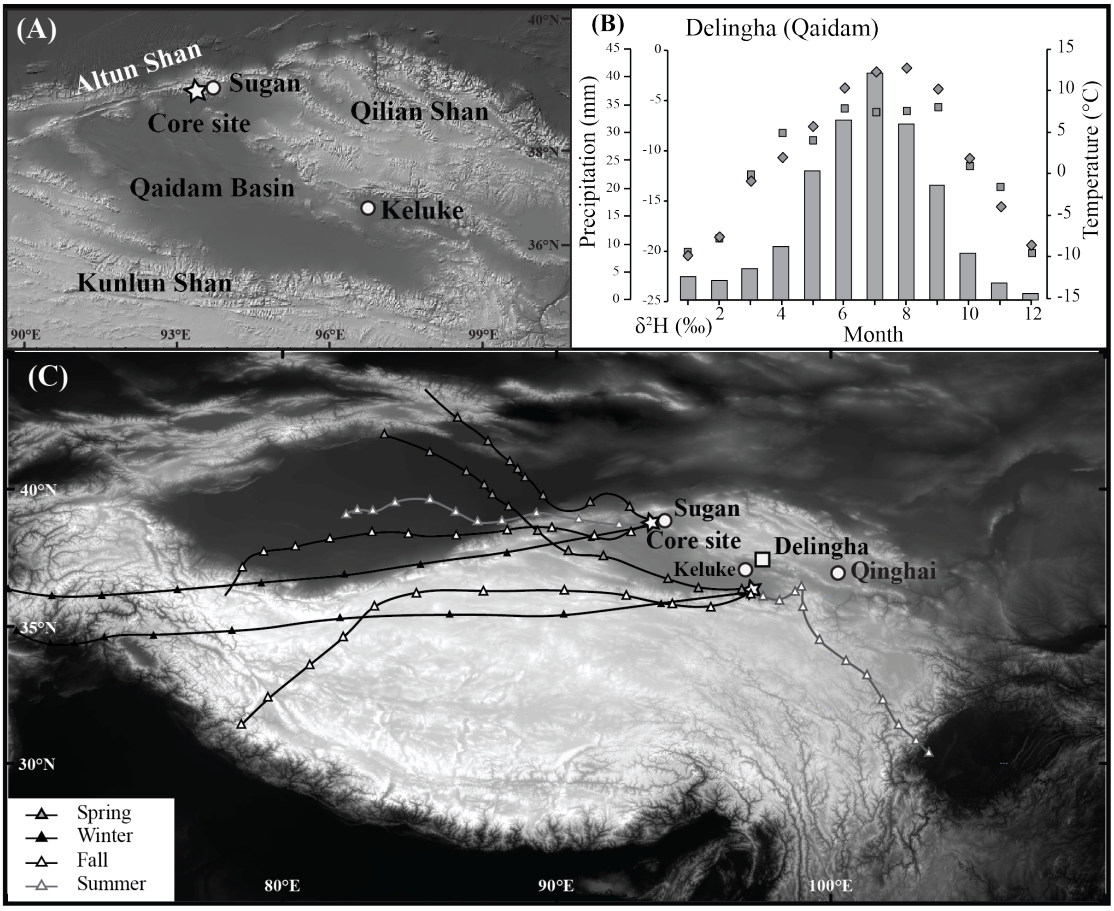

Figure 3.2. (a) Topographic map of northern Tibetan Plateau showing the coring site (star, this study) in the Qaidam Basin and locations of the Lake Sugan (Wang et al., 2013) and Lake Keluke (Rao et al., 2014) discussed in the text. (b) Meteorological data from Tibetan Network of Isotopes in Precipitation (TNIP) at the Delingha station (monthly mean precipitation amount, column; monthly mean temperature, diamond; monthly mean hydrogen isotope (δ2H) values of precipitation, square) (Yao et al., 2013). (c) HYbrid Single-Particle Lagrangian Integrated Trajectory Model (HYSPLIT) trajectories for summer, fall, winter, and spring air masses 72 hours before the arrival at the core site and a site (black star) in the eastern Qaidam Basin. The HYSPLIT model is based on NCEP Reanalysis data from 2018 to 2019 (https://www.arl.noaa.gov/hysplit). The TNIP station in Delingha (square) and lakes (circles) in the northern Tibetan Plateau discussed in the text are noted.

3.3. Materials and Methods

Sediment samples are obtained from a 42-meter-long core in the western Qaidam Basin (38°4'N, 93°0'E, 2754 m above sea level; Figs. 3.1 and 3.2). The core is composed of the late Pleistocene lacustrine sediments, which is overlain by Holocene evaporites. Sediments consist of primarily unconsolidated clay and silt, with sparse interbedded gypsum and halite. We reconstruct the paleohydrology of the Qaidam Basin by studying the compound-specific hydrogen isotopes of long-chain n-alkanes ($\delta^2H_{n\text{-alk}}$) with 29 and 31 carbon atoms (n-C_{29} and n-C_{31}) derived from terrestrial higher plants (Eglinton and Hamilton, 1967a). $\delta^2H_{n\text{-alk}}$ reflects the change in precipitation δ^2H and has been increasingly used in paleohydrology studies (Sachse et al., 2012). We compare the new isotope data with the Holocene records from Lake Keluke (Rao et al., 2014) and Lake Sugan (Wang et al., 2013) in the same basin to understand the temporal and spatial variations of climate. The relative input of aquatic versus terrestrial organic materials is evaluated by the biomarker proxy P_{aq} (Ficken et al., 2000) that provides ancillary information on the depositional facies associated with expansion and shrink of lake volume. Lake surface temperatures are reconstructed by the alkenone-unsaturation index (U^K_{37}) (Brassell et al., 1986; Prahl and Wakeham, 1987; Schouten et al., 2002) — a tempera-

ture proxy that has been used for estimating temperature variation of the Lake Qinghai during the Holocene (Hou et al., 2016). The CESM 1.3 climate models are used to examine the differences between the pre-industrial period and the LGM in precipitation, evaporation, and surface runoff during summer, in which the major rainfall occurs.

3.3.1. Radiocarbon Dating

Eight fine-grained clays were selected at specific depths and analyzed for ^{14}C ages (Fig. 3.3). Bulk sediments were analyzed for ^{14}C ages by accelerator mass spectrometry (AMS) at Beta Analytic Testing Laboratory. Sediments were grounded and sieved to <180 microns, and then treated with HCl acid to remove inorganic carbon before the analysis. A major issue in radiocarbon dating is the reservoir effect that introduces inherited age and residence age (Hendy and Hall, 2006). The inherited age can derive from the input of old carbon by river water that carries dissolved carbonate from the drainage system, while the residence age is caused by a delay in CO_2 exchange rates between the atmosphere and lake bottom water. A review paper on the reservoir effect on the Tibetan Plateau reveals that reservoir ages vary spatially and temporally over the Tibetan Plateau (Hou et al., 2012). The standard approach to derive the reservoir age is to compare the ^{14}C ages of modern in-situ

carbon (e.g., extant plant materials and organic matter of surface sediments) and/or the coexistent plant remains with measured ^{14}C ages. The overlying Holocene succession in the core site is eroded due to subaerial exposure, and thus the reservoir age cannot be obtained with modern lake surface sediments. We hence use the reservoir age derived from the adjacent Lake Sugan in the western Qaidam Basin (Fig. 3.1) to calibrate our sample ages. The reservoir age of Lake Sugan is estimated to 2627 years that is determined by the age difference between varve based ages and coexisting plants (Zhou et al., 2009). The varve-based ages are determined by the number of dark and light laminae couplets that characterize the seasonal variation of limnological conditions (Zhou et al., 2007). We subtract the reservoir age from the measured ^{14}C ages to derive the reservoir-corrected ^{14}C ages that are subsequently calibrated by Calib 7.0.4 software (Fig. 3.3).

3.3.2. Lipid Extraction

Total lipids were extracted with Soxhlet extractor using the azeotrope of dichloromethane/methanol (DCM/MeOH; 2:1 v/v) for 48 hours. The lipid extracts were evaporated under a stream of pure nitrogen until dry. Organic compounds in total lipid extracts were separated into apolar, intermediate, and polar fractions using a pipette column filled with ca. 0.5 grams of activated

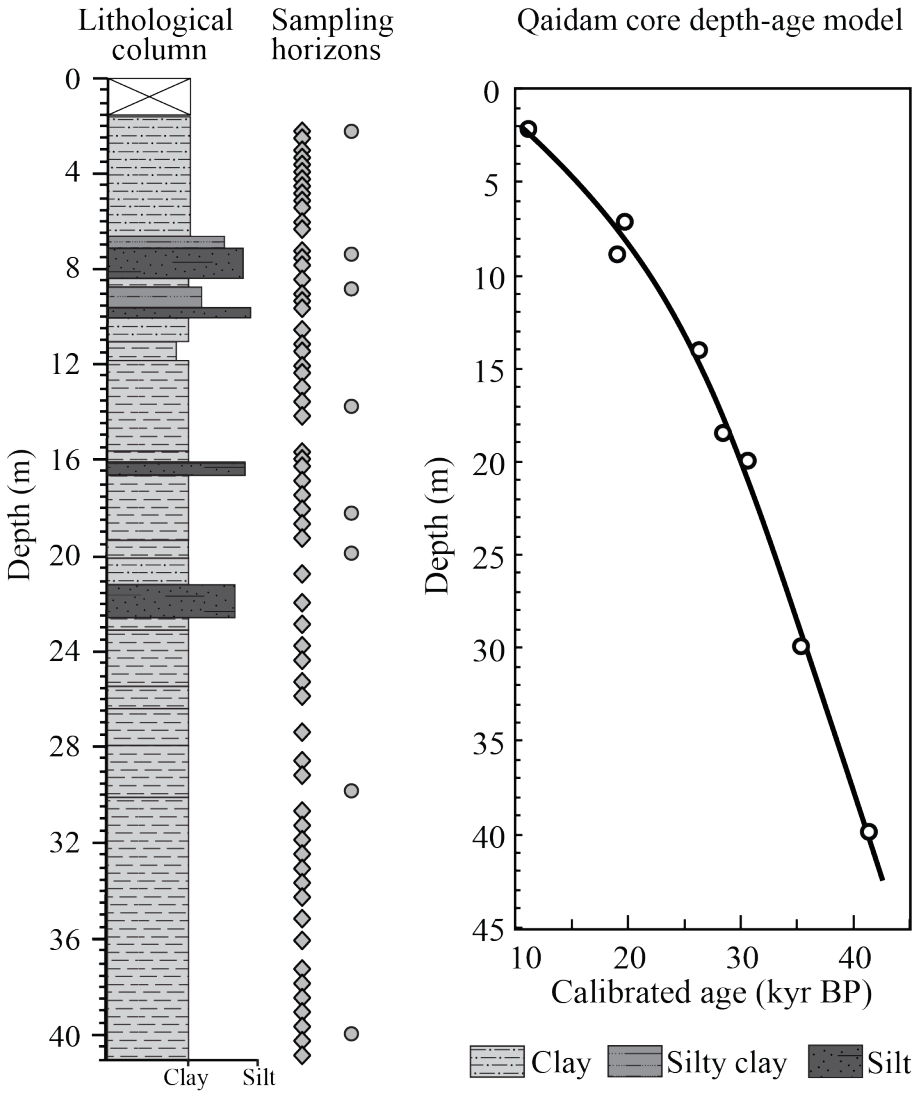

Figure 3.3. The lithostratigraphic column and the chronology of the core in the western Qaidam Basin. The age model is constructed by applying the 3rd order-polynomial correlation of 8 radiocarbon ages with the corresponding depth. Samples are analyzed for leaf wax hydrogen isotopes and U^{K}_{37} temperatures (diamond) and ^{14}C ages (circles).

silica gel and eluted with 2 ml hexane, 4 ml DCM and 4 ml methanol sequentially.

n-Alkanes contained in the apolar fractions were re-dissolved into 1500 µL of hexane and *n*-alkane abundances are determined using a Thermal Trace 1310 Gas chromatography (GC)-flame ionization detector (FID) fitted with programmable-temperature vaporization (PTV) injector and TG-1MS column (60 m long, 0.25 mm i.d., 0.25 µm film thickness). Samples were carried by helium at a rate of 2 ml/min. GC oven temperature is ramped from 60 °C (holding for 1 min) to 320 °C at a rate of 15 °C/min (holding for 20 min). Individual *n*-alkanes were identified by comparing the elution time with a reference standard (Mix A6, Schimmelmann, Indiana University Bloomington).

The carbon preference index (CPI) of n-alkanes are determined using the equation:

$$\mathrm{CPI} = \frac{1}{2}\frac{\sum \mathrm{A}(23+25+27+29+31+33) + \sum \mathrm{A}(25+27+29+31+33+35)}{\sum \mathrm{A}(24+26+28+30+32+34)} \quad (3.1)$$

Where A in the above equation stands for the areas of the individual n-alkanes that are estimated by using the software Xcalibur for chromatography analysis. The numbers 23 – 35 represent the chain length of *n*-alkanes.

The *n*-alkane distributions of terrestrial higher plants are maximized at

n-C_{29} and n-C_{31}, while submerged/floating plants are predominant by n-C_{23} and n-C_{25}. P_{aq} index is defined by the relative proportion of mid-chain (n-C_{23} and n-C_{25}) to long-chain n-alkanes (n-C_{29} and n-C_{31}) homologs (Ficken et al., 2000):

$$P_{aq} = \frac{A(23+25)}{A(23+25+29+31)} \tag{3.2}$$

Where A is identical to that in the equation for CPI, and the numbers indicate the chain length of odd-numbered n-alkanes.

3.3.3. Compound-Specific Hydrogen Isotope Analysis

Compound-specific hydrogen isotopes were measured using a Trace Gas chromatography (GC) 1310 coupled to a Thermo Delta V Advantage isotope ratio mass spectrometer (IRMS) interfaced with a Thermo Isolink interface. The GC column and carrier gas flow rate were identical to the GC-FID conditions. Compounds were separated on the GC with the temperature being programmed from 60 °C (held for 1 min) to 170 °C at 14 °C/min, to 300 °C at 3 °C/min, and then to 325 °C at 14 °C/min with an isothermal holding of 10 mins. H_3^+ factor was measured daily before isotopic analysis, with an average of 8.5 ppm (n = 3). Samples were analyzed in duplicate with a mean analytical precision of 1.5 ‰. Hydrogen isotope ratio values were determined

relative to the reference gas, calibrated against Mix A6 (n-C_{16} to n-C_{30}; Arndt Schimmelmann, Indiana University), and reported relative to VSMOW with two standard errors using the equation:

$$\delta^2\mathrm{H} = \left(\frac{\mathrm{R_{sample}}}{\mathrm{R_{standard}} - 1}\right) \times 1000 \tag{3.3}$$

Where R stands for the ^{2}H/H ratios of samples and reference materials. The $\delta^2\mathrm{H}_{n\text{-alk}}$ values are reported to Vienna Standard Mean Ocean Water (VSMOW) and expressed in per mil (‰).

We focus discussions on the weighted mean $\delta^2\mathrm{H}_{n\text{-alk}}$ values of n-C_{29} and n-C_{31}, which is calculated using the equation:

$$\delta^2\mathrm{H}_{n\text{-alk}} = \frac{\sum \mathrm{A}_i \times \delta^2\mathrm{H}_i}{\sum \mathrm{A}_i} \tag{3.4}$$

Where A stands for the areas of individual n-alkanes, and i (29 and 31) indicates carbon-chain-lengths.

3.3.4. Alkenone Analysis

The solvent fraction containing alkenones was analyzed on Thermal Trace 1310 Gas chromatography (GC)-flame ionization detector (FID) fitted with programmable-temperature vaporization (PTV) injector using a TG-1MS column (60 m long, 0.25 mm i.d., 0.25 µm film thickness) and a helium flow

rate of 2 ml/min. The GC oven temperature was ramped from 60 °C (holding for 1 min) to 280 °C at 20 °C/min and then to 325 °C at 2 °C/min with isothermal holding for 25 minutes. $C_{37:4}$, $C_{37:3}$, and $C_{37:2}$ methyl alkenones display typical peak clusters that can be identified by the identical retention time to the internal laboratory reference sample on GC-FID. Typical samples were analyzed on Gas chromatography-mass spectrometry (GC-MS) at MIT to confirm the identification of alkenones. On GC-MS, alkenones are identified by the major ion fragment of m/z 81, and molecular ions of m/z 530.5, 528.5, and 526.5 for $C_{37:2}$, $C_{37:3}$, and $C_{37:4}$, respectively. The GC retention time and mass spectrum of the representative sample (ZK1405-3-4) are shown in Fig. S2. Relative abundances of $C_{37:4}$, $C_{37:3}$, and $C_{37:2}$ alkenones were calculated using integrated areas determined through the Xcalibur software. Alkenone unsaturation indices (U^K_{37}) were determined by the equation (Prahl and Wakeham, 1987):

$$U^K_{37} = \frac{C_{37:2} - C_{37:4}}{C_{37:2} + C_{37:3} + C_{37:4}} \tag{3.5}$$

The conversion of U^K_{37} to temperature is based on calibration using modern lake surface sediments in the Tibetan Plateau that constructs a relationship between U^K_{37} and summer lake surface temperature (Wang and Liu,

2012; Hou et al., 2016):

$$T = 17.571 \times U_{37}^{K} + 20.849 \; (R^2 = 0.8059, n = 26) \tag{3.6}$$

We apply this relationship to convert our U_{37}^{K} data to lake temperature.

3.3.5. Climate Simulation during the LGM

We use the Community Earth System Model (CESM) version 1.3 to examine changes in precipitation, evaporation, runoff, and effective precipitation during the LGM relative to pre-industrial (PI) levels in summer. Effective precipitation is expressed as the following equation:

$$P_e = P_t - E - R \tag{3.7}$$

Where P_e represents effective precipitation, which equals total precipitation (P_t) minus evaporation (E) and runoff (R) (Oleson et al., 2010). Models include the coupler, and active atmosphere, land, ocean, and ice components. We examine two fully coupled experiments, each representing the simulated climate in the PI and the LGM, to further test changes in precipitation, evaporation, runoff, and effective precipitation during the summer of the LGM (21 ka) relative to the PI. The PI simulation is performed by Zhu et al. (2017), and all climatic forcing for the PI is fixed at values from A.D. 1850. The LGM is an ex-

tension of the simulation in Zhu et al. (2017), and the results of this extended LGM experiment is recently reported in (Tierney et al., 2019). Boundary conditions of the LGM, including greenhouse gases (GHGs), orbital parameters, and ice sheets, follow the PMIP4 protocol (Kageyama et al., 2017). Specifically, CO_2, CH_4, and N_2O are set to 190 ppm, 375 ppb, and 200 ppb in simulations, respectively. The ICE-6G reconstruction 6G (Peltier et al., 2015) is used for the ice sheet, and the associated changes in surface elevation, albedo, and land-ocean distribution are derived from the ICE-6G reconstruction. This LGM simulation well captures the global cooling estimated from proxy data synthesis (Tierney et al., 2019).

3.4. Results and Discussions

3.4.1. ^{14}C Ages of the Qaidam Core

We obtained eight radiocarbon ages from bulk sediments. The chronology of eight radiocarbon dating ages is best modeled with the 3rd order polynomial curve that is extrapolated to derive the youngest (ZK1405-2-1; 10,878 yrs) and oldest (ZK1405-44-24; 45,648 yrs) ages. Ages for samples between dating points are derived from interpolation. The established chronology enables us to interpret biomarker and isotope proxy records on the millennial time scale.

3.4.2. Lake Temperature Reconstructions

The evolution trend of lake temperatures (Fig. 3.4a) broadly follows the Northern Hemisphere summer insolation, with high (low) temperatures corresponding to high (low) summer insolation (Fig. 3.4c). The lake temperatures are warm at 45-39 ka and 37-33 ka (Fig. 3.4a), which are similar to the temperatures in the Lake Qinghai during the early Holocene (9-5 ka) and the late Holocene (since ca. 3 ka) (Hou et al., 2016). Our lake temperature reconstructions agree with the pollen records in the Qilian Shan that suggest an interglacial temperature condition with the higher tree line during the MIS 3 (Herzschuh et al., 2006). Low temperatures during 39-37 ka coincide with the Heinrich 4 (H4) event that occurs at ~ 38 ka in the Greenland ice core record (Hemming, 2004). The lake temperatures decrease and reach the second low stage during 21-19 ka, which is within the duration of global LGM (26.5-18 ka) (Mix et al., 2001; Clark et al., 2009); the average lake temperature is lower than the early Holocene Climate Optimum (9-5 ka) by > 6 °C (Fig. 3.4a). Lake temperatures increase after the LGM, which is synchronous with Northern Hemisphere warming (Shakun et al., 2012) and interrupted by another significant cooling during the Younger Dryas (YD) at ca. 13 ka (Alley, 2000).

3.4.3. Distribution of *n*-Alkanes

The *n*-alkanes (from *n*-C_{23} to *n*-C_{35}) preserved within the sediment core have CPI values ranging from 1 to 12.8, with a mean of ~3.7 (Supplementary Table), indicating the least possibility of thermal alteration after deposition (Eglinton and Hamilton, 1967a). In addition, sediments have never been significantly buried or heated. The P_{aq} values the proxy measuring the inputs of submerged/floating aquatic macrophytes relative to emergent and terrestrial species (Ficken et al., 2000) - vary from 0.05 to 0.63 with a mean value of ~0.39.

3.4.4. Paleohydrology Reconstructions

$\delta^2H_{n\text{-alk}}$ values during the last glacial period are generally lower than the late Holocene values from the Lake Sugan (Wang et al., 2013), except the three excursions with high isotopic values (Fig. 3.4b). The $\delta^2H_{n\text{-alk}}$ values vary between -181 ‰ and -199 ‰ at 45-39 ka, followed by a positive shift with the highest value of -167 ‰ at 37 ka. After the excursion, the $\delta^2H_{n\text{-alk}}$ values shift to a low value of -192 ‰ at 35 ka. The low $\delta^2H_{n\text{-alk}}$ values persist until the second excursion occurs at 22 ka with the highest $\delta^2H_{n\text{-alk}}$ value (-152 ‰) for the whole time series. The $\delta^2H_{n\text{-alk}}$ values shift from –152 ‰ at 22 ka to -204 ‰ at 20 ka and gradually increase until the end of the last glacial period.

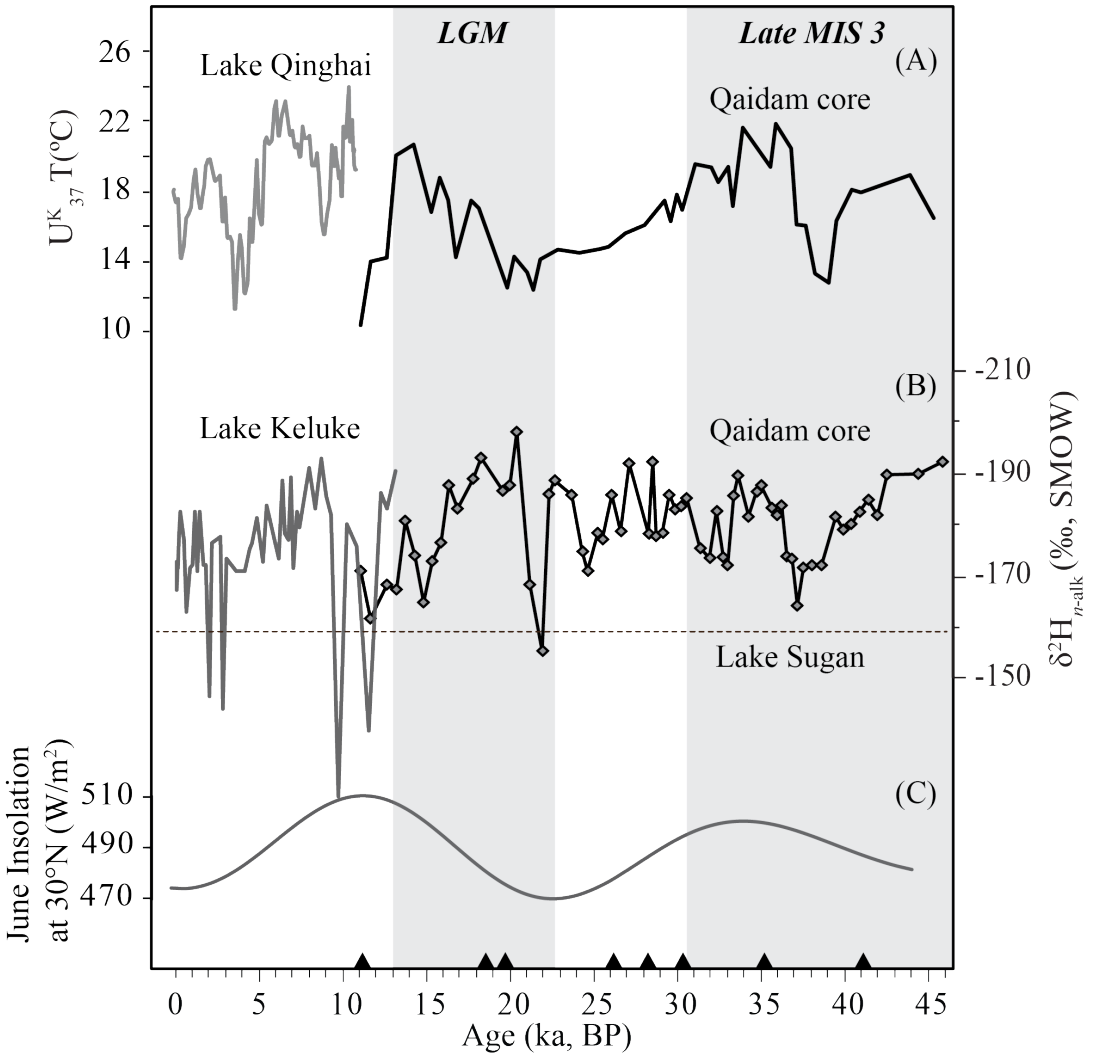

Figure 3.4. U^K_{37} temperatures and $\delta^2H_{n\text{-alk}}$ records since 45 ka. (a) The alkenone-based U^K_{37} temperature records for the core between ca. 45 ka and 11 ka (black line; this study) and the Lake Qinghai in Holocene (gray line; Hou et al., 2016). (b) The weighted-mean n-alkane hydrogen ($\delta^2H_{n\text{-alk}}$) isotope records of n-C_{29} and n-C_{31} from the core (diamonds; this study); $\delta^2H_{n\text{-alk}}$ record from Lake Keluke during the Holocene (gray line; Rao et al., 2014). The dashed line represents the mean $\delta^2H_{n\text{-alk}}$ value from a 1700-year-long record of $\delta^2H_{n\text{-alk}}$ for Lake Sugan (Wang et al., 2013). (c) June insolation at 30 °N (Berger, 1978). Shaded bars show the intervals of LGM and late MIS 3. Black triangles along the horizontal axis represent ^{14}C ages used for the age model of the Qaidam core.

3.4.5. Removal of Temperature Effect from $\delta^2H_{n\text{-alk}}$

Variation of modern precipitation δ^2H values in arid central Asia, including the Qaidam Basin, are driven predominantly by temperature (Araguas-Araguas et al., 1998) (Fig. 1 and S1). Colder regional temperatures result in ^2H-depleted precipitations (hence low δ^2H values) due to the larger isotopic fractionation effect. However, low $\delta^2H_{n\text{-alk}}$ values during the MIS 3 and the deglaciation are unlikely to be the result of high lake temperatures, as indicated by the U^K_{37} record (Fig. 4a). To investigate the non-thermal factors on the hydrogen isotopic compositions, we first remove the effect of temperature on the $\delta^2H_{n\text{-alk}}$ record by subtracting the ^2H depletion and enrichment induced by temperature variations. The adjusted $\delta^2H_{n\text{-alk}}$ values are represented by $\delta^2H_{n\text{-alk-T}}$, reflecting the change of moisture source and water balance between precipitation and evaporation. To apply a reasonable comparison between hydrological conditions during the last glacial period and the Holocene, we use the same strategy to remove the temperature effect on the Holocene record of Lake Keluke (also called Lake Hurleg) in the eastern Qaidam Basin (Fig. 4b). The late Holocene alkenone based U^K_{37} temperatures from Lake Qinghai (Hou et al., 2016) are considered feasible to imply the contemporary temperature in the Qaidam Basin, as the annual temperatures of the Lake Qinghai (0.1°C) (An

et al., 2012) is close to that of the Qaidam Basin (2°C) at present (Yao et al., 2013). The detail procedures to remove the temperature effect are as follows:

1. We calculate the temperature differences (ΔT) for samples of the Qaidam Basin during the last glacial period relative to the latest Holocene temperature (18°C) of the Lake Qinghai (Hou et al., 2016).

2. δ^2H_p-$\delta^{18}O$ relationship from the meteorological station at Delingha is used to obtain the δ^2H_p-temperature relationship. The slope of the $\delta^{18}O$-temperature relationship is 0.65‰/°C, and the slope of the local meteoric water line is 6.8 (Tian et al., 2003). The calculated slope of the δ^2H_p-temperature is 4.4 ‰/°C. The Δ T calculated in step (1) is then converted to the difference in δ^2H_p.

3. The relationship between δ^2H_p and $\delta^2H_{n\text{-alk}}$ is expressed by the equation: $\varepsilon_{n-\text{alk/p}} = \frac{\delta^2H_{n\text{-alk}}+1}{\delta^2H_p+1} - 1$. $\varepsilon_{n-\text{alk/p}}$ is defined as the apparent fractionation factor (Polissar et al., 2009). Regional compilations on the apparent fractionation across the Tibetan Plateau show $\varepsilon_{n-\text{alk/p}}$ is invariant despite significant changes in climate and ecology across the plateau (Zhuang et al., 2014; Zhang et al., 2017). We use the $\varepsilon_{n-\text{alk/p}}$ values of -102 ‰ in the Qaidam Basin (Zhuang et al., 2014) to convert the temperature-dependent difference in δ^2H_p ($\Delta\ \delta^2H_p$) to that difference in $\delta^2H_{n\text{-alk}}$ ($\Delta\ \delta^2H_{n\text{-alk}}$).

4. For comparison, we process the $\delta^2H_{n\text{-alk}}$ record of Lake Keluke and Lake Sugan in the same way (Fig. 3.6b).

The temperature-corrected $\delta^2H_{n\text{-alk-T}}$ record of the Qaidam core shows the larger amplitude and different structure of the isotope pattern as compared to the uncorrected $\delta^2H_{n\text{-alk}}$ record. This suggests a strong temperature control on terrestrial biomarker $\delta^2H_{n\text{-alk}}$ values in this area. The removal of temperature effect shifts $\delta^2H_{n\text{-alk-T}}$ values to more negative values between 30-37 ka

with a minimum value of -203 ‰, while producing more positive values between 11-30 ka with a maximum value of -135 ‰ (Fig. 3.6b). After removing the temperature effect, our discussions focus on the temperature-corrected $\delta^2H_{n\text{-alk-T}}$ records for understanding the evolution of moisture source and precipitation/evaporation balance.

$\delta^2H_{n\text{-alk-T}}$ values vary in a wide range of ~70 ‰, reflecting dramatic changes in hydrology during the last glacial period. Data shows low values during the late MIS 3 and the deglaciation (20-11 ka), and high values during the LGM (27-18 ka) (Fig. 3.6b). The extreme aridity in the three short periods (39-37 ka, 22-21 ka, and 13-11 ka) is inferred by the positive excursions, corresponding to the H4, H2, and YD, respectively. The H1 and H3 events are not prominent as the YD, H2, and H4 in the new isotopic record.

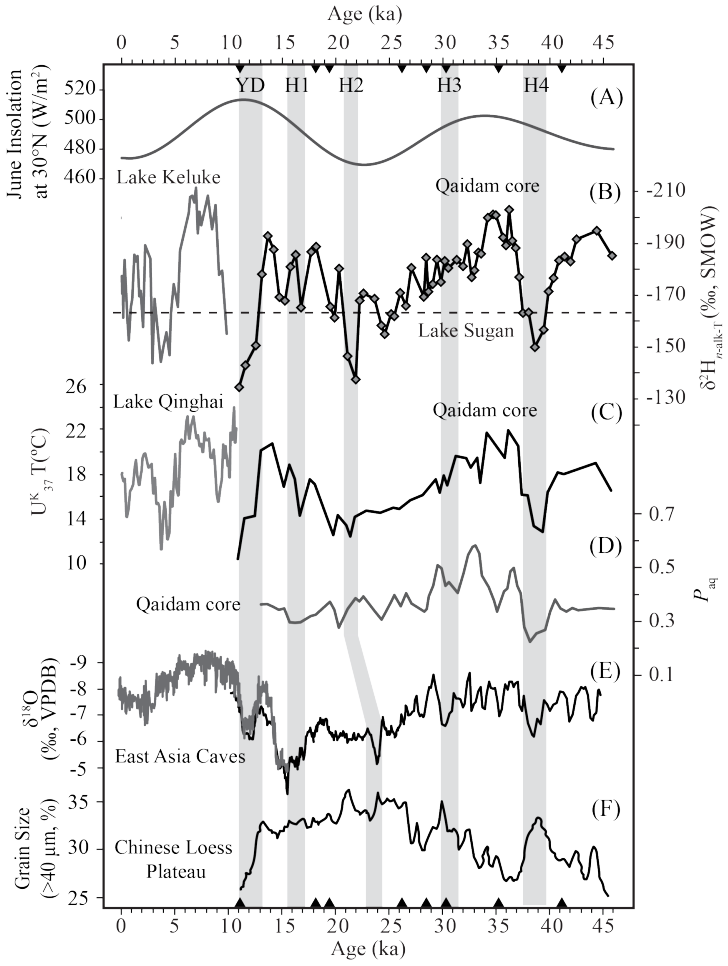

Figure 3.5. Regional paleoclimatic records since 45 ka. (a) The insolation at 30°N in June (Berger, 1978). (b) Calculated $\delta^2H_{n\text{-alk-T}}$ values corrected for temperature effect on precipitation δ^2H for core samples in the western Qaidam Basin (diamonds; this study) and the Lake Keluke in the eastern Qaidam Basin (gray line) (Rao et al., 2014). The dashed line represents mean $\delta^2H_{n\text{-alk-T}}$ values from Lake Sugan (Wang et al., 2013). (c) The U^K_{37}-based temperatures for the core (black line; this study) between 45 ka and 11 ka and the Lake Qinghai in the Holocene (gray line; Hou et al., 2016). (d) Submerged aquatic macrophyte versus terrestrial higher plants (Paq) ratio for the study core. (e) Speleothem $\delta^{18}O$ records from the Dongge (gray line; Dykoski et al., 2005) and Hulu caves (black line; Wang et al., 2008). (f) Grain-size data from eolian deposits on the Chinese Loess Plateau (Rao et al., 2013). Gray bars denote the Younger Dryas (YD) and Heinrich events (H1 to H4).

3.4.6. Strong Asian Summer Monsoons During the Late MIS 3

New $\delta^2H_{n\text{-alk-T}}$ values and U^K_{37}-based lake temperatures co-vary with the summer insolation during the last glacial period. Low isotopic values and warm temperatures occur during the high summer isolation period, while the high isotopic values and cold temperatures occur during the low summer insolation period (Figs. 5a, b, and c). Speleothem $\delta^{18}O$ records from Dongge and Hulu caves in East Asia show similar isotopic patterns, with low precipitation $\delta^{18}O$ values corresponding to enhanced rainfall during high summer insolation and high $\delta^{18}O$ values corresponding to reduced rainfall during low summer insolation (Fig. 3.6e) (Dykoski et al., 2005; Wang et al., 2008). The intensity of the Asian summer monsoons is primarily controlled by land-ocean thermal contrast, latent heating over the Tibetan Plateau, and equatorial Pacific sea surface temperature at both the millennial and precessional scale (Webster et al., 1998; Molnar et al., 2010; Wu et al., 2012; Caley et al., 2014). Plant wax $\delta^2H_{n\text{-alk}}$ records (Thomas et al., 2016; Hou et al., 2017) and ostracod $\delta^{18}O$ record (Chen et al., 2016) from the Lake Qinghai indicate the Asian summer monsoons are strong during the early Holocene when summer insolation is high. Our new $\delta^2H_{n\text{-alk-T}}$ records from the drill core during the late MIS 3 (30-45 ka), except for the H4 event (Fig. 3.6b), have similar isotopic values to that

of Lake Keluke during the early Holocene (Rao et al., 2014). Given that the Qaidam Basin lies on the boundary between the Westerlies and the Asian summer monsoons, we argue that the strong Asian summer monsoons that are driven by precessional forcing penetrate further into Central Asia during the warm late MIS 3, resulting in increased precipitation and lower $\delta^2H_{n\text{-alk-T}}$ values are demonstrated in the Qaidam core.

The isotopic records from Central Asia support our interpretation of enhanced northward penetration of Asian summer monsoon moisture associated with migration of the climatic boundary into the Asian interior during the MIS 3. Speleothem $\delta^{18}O$ records from the Ton cave and Kesang cave in the area of the present Westerlies area further to the west of our study area (Fig. 1) show the cyclic incursions of Asian summer monsoons into Central Asia since ca. 500 ka (Cheng et al., 2012). Leaf wax $\delta^2H_{n\text{-alk}}$ record from the Pamirs in the southwestern border of the Westerlies-influencing region reveals a similar pattern during the early Holocene when summer insolation is high and the strong Asian summer monsoons penetrate deep into Central Asia (Aichner et al., 2019).

Low $\delta^2H_{n\text{-alk-T}}$ values are concurrent with peak P_{aq} ratios between 30 ka and 37 ka. (Fig. 3.6d). The high P_{aq} values could result from either an increase

of aquatic macrophytes and/or a decrease of terrestrial plant input. Paleo-shoreline records from the Tibetan Plateau and adjacent desert regions show that the paleo-lakes (Fig. 1) expanded ~40-30 ka with lake levels 30 to 280 m higher than the present (Chen and Bowler, 1986; Zhang et al., 2008). Given that the terrestrial plants have expanded during the MIS 3 in the northern Tibetan Plateau (Herzschuh et al., 2006), we suggest that the variations of P_{aq} values reflect the changes in local hydrological conditions, which results in a substantial increase in the proportion of biomarkers produced by the aquatic plants relative to the terrestrial plants and preserved in the sediment core. High P_{aq} values at ca. 37-30 ka are likely to reflect a shift in the paleohydrological condition of paleolake from shallow and proximal to the deep and distal lacustrine environment, accompanied by enhanced lake production during the strong Asian summer monsoon period.

Previous results are interpreted to show that the wet climate during the late MIS 3 in northwestern China is linked with the increasing Westerlies circulation during the glacial period (Yang et al., 2004). The Westerlies wind index of grain-size data from Tianshan and Chinese Loess Plateau along the Westerlies route supports the argument that the strength of Westerlies during MIS 3 is higher than the present but weaker than the LGM (Fig. 3.6f)

(Sun et al., 2012; Rao et al., 2013; Li et al., 2016). However, in the Westerlies-controlled Mediterranean region, the lake levels during the MIS 3 is lower than the LGM due to the weaker Westerlies storm track (Bartov et al., 2003; Torfstein et al., 2013). Our low $\delta^2H_{n\text{-alk-T}}$ values suggest that the late MIS 3 is wetter than the LGM, which is different from hydrologic patterns in the core area of the Westerlies-influenced region. Hence, we infer that the warm-wet paleoclimate is associated with intensified Asian summer monsoons rather than the Westerlies.

3.4.7. High Effective Precipitation and Reduced Evaporation during the LGM

$\delta^2H_{n\text{-alk}}$ values increase from the end of MIS 3 to the LGM (Fig. 3.6b). We interpret that increasing $\delta^2H_{n\text{-alk}}$ values indicate that the climate becomes drier as the Asian summer monsoons retreat from Central Asia when summer insolation declines. As a result, the Westerlies advance and act as the primary moisture source to the Qaidam Basin during the LGM. A southward extension of the ice sheet in the Northern Hemisphere during the LGM potentially enlarges the meridional thermal gradient and strengthens the mid-latitude Westerlies (COHMAP members, 1988; Toggweiler and Russell, 2008; Sun et al., 2012; Wang et al., 2018). Grain-size analysis and hydrology reconstruction of lacustrine sediments from the northeastern Tibetan Plateau supports cold

and dry climate associated with the enhanced Westerlies during the LGM (An et al., 2012; Wang et al., 2014; Thomas et al., 2016). Pollen records also show an increase in the components of cold- and arid-tolerant plants, represented by alpine desert and alpine sparse during the LGM in the nearby Qilian Shan (Herzschuh et al., 2006).

During the LGM, $\delta^2H_{n\text{-alk-T}}$ values of the Qaidam core are lower than that of the Lake Sugan (Fig. 3.6b), implying a less arid climate. The $\delta^2H_{n\text{-alk-T}}$ values are comparable to that of Lake Keluke since the late Holocene, indicating that the LGM hydrological condition in the Western Qaidam is similar to that in the eastern part at present. Our climate simulations of the LGM shows that the summer precipitation decreases in the western Qaidam Basin by 0.25-0.5 mm/day than the PI (Fig. 6a). The modeled evaporation is also reduced during the LGM relative to the PI, likely resulting from low temperatures due to minimal summer insolation (Fig. 6b) (Allen et al., 1998). The runoff also declines during the LGM, reflecting a reduction in soil water infiltration and recharge (Fig. 6c). The reduction in evaporation and runoff surpasses that in precipitation, leading to an increase in effective precipitation (P_e) during the LGM relative to the PI (Fig. 6d). Recent isotope proxy data and climate simulation result from the Pamirs also highlight the importance of decreased sum-

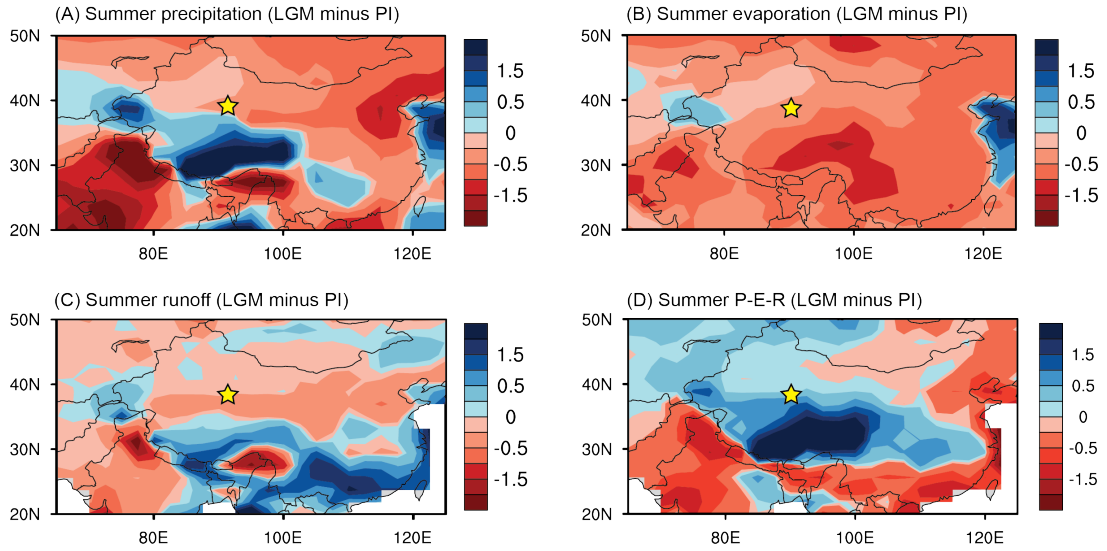

Figure 3.6. Numerical modeling results plotted on the Hovmoller diagrams for precipitation (a), evaporation (b), runoff (c), and effective precipitation (Pe; calculated from equation 7) (d) during summer. Model results for precipitation include both liquid (rain) and solid (snow). The yellow star indicates the Qaidam Basin. Units: mm/day.

mer evaporation in triggering the lake transgression during the last glacial period (Aichner et al., 2019). The climate simulation results support our interpretation of $\delta^2H_{n\text{-alk-T}}$ records that an overall cold-arid climate but wetter than the present during the LGM.

3.4.8. Short-period Aridity during Extreme Cold Events

Three pronounced positive $\delta^2H_{n\text{-alk}}$ excursions and the cold U^K_{37} temperatures during YD, H2, and H4 events indicate millennial-scale pulses of aridity (Fig. 5). Proxy records and climate models suggest that the freshwater discharge from the Laurentide ice sheet during the Heinrich stadials slows

down the Atlantic meridional overturning circulation and reduces the northward ocean heat transport, which cools the Northern Hemisphere (Bond et al., 1997; Kageyama et al., 2010; Sun et al., 2012; Henry et al., 2016). The change in Atlantic circulation drives the short period of aridity in both the Westerlies- and the monsoons-areas. For example, the shoreline record of paleo-lake Lisan in the eastern Mediterranean region shows the general high lake level during the LGM was interrupted by drought phases during the Heinrich events, which results from a short-period shutdown of Mediterranean storm due to the cooler ocean temperature (Bartov et al., 2003; Torfstein et al., 2013). Pollen records from the Yili basin in Central Asia suggest an arid climate during the YD associated with cooling in the North Atlantic surface temperature (Li et al., 2011b). In East Asia, climate models indicate that cooling in the North Atlantic shifts the intertropical convergence zone southward and weakens the summer monsoons (Zhang and Delworth, 2005; Sun et al., 2012), which agrees with the speleothem and loess/paleosol records (Dykoski et al., 2005; Wang et al., 2008; Rao et al., 2013).

3.5. Conclusions

New biomarker and isotope proxy studies show that the paleohydrology and lake temperatures in the Qaidam Basin vary in response to precessional

forcing during 45-11 ka. A new $\delta^2H_{n\text{-alk-T}}$ record shares similar characteristics to the isotopic signatures from Asian summer monsoon-influenced regions, with the lower $\delta^2H_{n\text{-alk-T}}$ values and enhanced precipitation during high summer insolation. We suggest that the enhanced northward penetration of Asia summer monsoon moisture produced a wetter climate during the late MIS 3 (45-39 ka and 37-33 ka) with the climate boundary between the Westerlies and the Asian summer monsoons penetrating further into Central Asia under high summer insolation. A cold-arid climate dominates the region during the LGM when the Asian summer monsoons retreat, but with a substantial reduction in evaporation and surface runoff. We ascribe this to the unique location of the Qaidam Basin that links the Westerlies and Asian summer monsoons in the Northern Hemisphere. The two atmospheric systems alternately control the climate in the Qaidam Basin as a result of their relative strength. Extreme aridity is induced by the interruption of moisture transport from the Westerlies and Asian summer monsoons during the North Atlantic events. New isotope and temperature data support the cold-dry climate in glacial/stadial periods and warm-wet climate in interglacial/interstadial periods. These new results provide evidence that the paleo-lake may expand during the LGM due in large part to the effect of reduced evaporation.

Chapter 4. Hemispherical Temperature Asymmetry Shifting the Atlantic ITCZ Northward During the Eocene-Oligocene Transition

4.1. Introduction

The abrupt shift in the global climate at the Eocene-Oligocene (E-O) boundary marks a transition from ice-free "greenhouse" conditions to glacial "icehouse" conditions. The Eocene-Oligocene Transition (EOT) (~34.1–33.6 Ma) is characterized by the reduction in atmospheric pCO_2 (Pearson et al., 2009; Pagani et al., 2011), the onset of continental-scale Antarctic glaciation (Coxall et al., 2005), cooling in high-latitude (Liu et al., 2009), and massive biotic extinctions and evolutionary turnover (Wade and Pearson, 2008). Climate simulation and proxy studies have proposed that the decrease in pCO_2 and opening of Southern Ocean gateways have triggered feedback among continental weathering, reorganization in ocean structure and circulation, and Antarctic glaciation (DeConto et al., 2008; Lear et al., 2008; Pearson et al., 2009; Elsworth et al., 2017).

Although there is a consensus indicating global cooling from the late Eocene to the early Oligocene time, the magnitude and timing of cooling appear different between the two hemispheres. Sea surface temperature (SST) decreases more substantially at higher-latitudes relative to low-latitudes (Liu

et al., 2009; Wade et al., 2012). The Northern Hemisphere SSTs do not decrease until the onset of the Early Oligocene Glacial Maximum (EOGM) but is cooling delayed in the Southern Hemisphere during the EOT (Cramer et al., 2009; Liu et al., 2018). This interhemispherical asymmetry in temperatures has been linked to changes in ocean circulation due to Antarctic glaciation and deepening of ocean gateways (Goldner et al., 2014; Abelson and Erez, 2017; Elsworth et al., 2017). A coupled ocean-atmosphere model hypothesis is that the growth of the Antarctic ice sheet during the EOT has increased meridional temperature gradients in the ocean and atmosphere, which then enhances the northward heat transport in Antarctic intermediate water and invigorates the formation of Atlantic deep water (Goldner et al., 2014). As increasing evidence on the timing of North Atlantic deep water (NADW) formation, benthic foraminifera $\delta^{18}O$ and $\delta^{13}C$ records from North Atlantic indicate that the export of northern component water (precursor to the NADW) precedes Antarctic glaciation by ca. 1 Ma (Coxall et al., 2018). This observation is supported by model simulations that posit an invigorated modern-like Atlantic Meridional Overturning Circulation (AMOC) associated with the deepening of Drake Passage in the late Eocene (Elsworth et al., 2017). The inception of AMOC enhances precipitation at low-latitudes on continents, trigger-

ing positive feedback between continental weathering and drawdown of pCO_2 (Elsworth et al., 2017). Climate model and proxy data have built up a linkage among change in ocean circulation, low-latitude precipitation, weathering processes, and consumption of atmospheric CO_2. However, proxy data that characterize the AMOC effect across the EOT in tropical-subtropical regions are lacking.

The Gulf of Mexico (GoM) is part of the Western Hemisphere warm pool, by which ocean heat transport impacts the hydrological conditions in subtropical coastal regions (Wang and Enfield, 2001). Multi-proxy studies show a ~3°C cooling within the GoM during the late Eocene and a significant sea-level fall of ~80 m during the EOGM (Katz et al., 2008; Miller et al., 2008; Wade et al., 2012). However, pollen records from the Gulf Coast region suggest a gradual cooling and drying from late Eocene to the early Oligocene time, with no significant change in hydrology or ecology near the E-O boundary (Oboh-Ikuenobe and Jaramillo, 2003). Coastal regions tend to present a stronger climatic response that mimics the change in the marine realm due to its proximity to the marine moisture source (e.g., Hampshire Basin in the UK; Sheldon et al., 2016), while it is difficult to explain the discordant paleoclimatic data between terrestrial and oceanic systems in the

GoM (Oboh-Ikuenobe and Jaramillo, 2003; Wade et al., 2012). This highlights the necessity of high-resolution paleohydrological reconstruction across the EOT. To fill this gap, we measured carbon ($\delta^{13}C_{wax}$) and hydrogen ($\delta^{2}H_{wax}$) isotopes of terrestrial leaf waxes from a Gulf Coast drill core and thus have quantified the paleohydrology across the EOT. We also measured the tetraether index (TEX86) (Schouten et al., 2002) to reconstruct the SSTs in the GoM. This reconstructed paleoclimate is compared to contemporaneous terrestrial and oceanic proxy data, thus making it possible to understand how the continental hydrology interacts with the change in ocean and atmosphere systems across the EOT.

4.2. Lithostratigraphy, Age Constraints, and Modern Climate

Ellwood et al. (2019) used lithostratigraphy, biostratigraphy, geochemical, and geophysical methods to correlate five Eocene-Oligocene boundary successions in the southeastern United States, and these results were compared to the Global Boundary Stratotype Section and Point (GSSP) near Massignano in central Italy. The Hiwannee (HIW) core (31.83°N; 88.69°W; Fig. 4.1) is one of the five sites in southeastern Mississippi. The whole succession is ~60 m in length, covering from the upper Eocene North Twistwood Creek Formation to the lower Oligocene Forest Hill Formation. The Eocene-Oligocene bound-

ary in the study site is placed between the uppermost Eocene Shubuta Clay Member of the Yazoo Formation to the lowermost Oligocene Red Bluff Formation of the Vicksburg Group (Ellwood et al., 2019) (Fig. 4.3). These units were deposited in a shallow marine to the marginal marine environmental setting. The Shubuta Clay Member sampled here is ~25 m thick and is composed of greenish glauconitic clay that grades upward into a bluish and phosphate-rich glauconitic marl. The Red Bluff Formation is tan to brownish, glauconitic-rich, marly clay, with abundant pyrite-filled burrow. This unit is interbedded with sideritic-carbonate beds that were latterly altered into ion-oxides. Due to the variation of bed hardness, the contact between the Red Bluff and the overlying Forest Hill formation was washed out during the drilling process. Studies of the lithostratigraphy of Eocene-Oligocene units in southeastern Mississippi indicate that the Red Bluff Fm. thickness is ~3 m (Oboh-Ikuenobe and Jaramillo, 2003). We recovered a ~2.5 m thick succession in the core, but the uppermost part of the Red Bluff Formation was lost during the drilling process.

The age of the HIW core is constrained by the lithostratigraphy, biostratigraphy and magnetostratigraphy (Ellwood et al., 2019). The Eocene-Oligocene boundary within the HIW core is identified by the last appearance of *Hantkeninidae* in the uppermost Shubuta Clay (Ellwood et al., 2019). Thus,

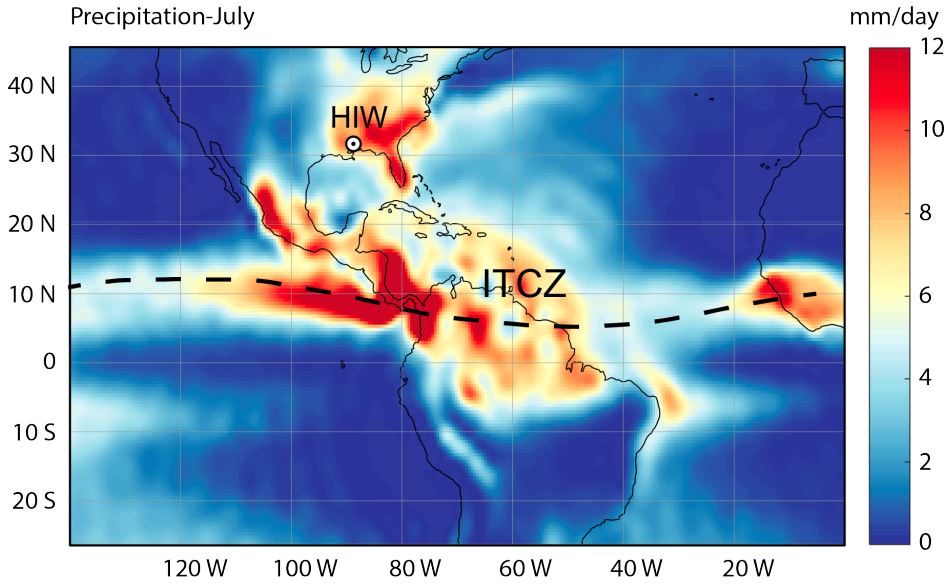

Figure 4.1. Modern boreal summer precipitation. The Hiwannee (HIW) core site (circle) and northernmost position of Atlantic Intertropical Convergence Zone (dashed line). Precipitation data (mm/day) are derived from NCEP/NCAR Reanalysis dataset for the period 1981 – 2010. Insert shows the locations of sea surface temperature records (circles) from IODP Sites 511 and 1404 (Liu et al., 2009; Liu et al., 2018), and terrestrial paleoclimate records (stars) from the western United States (WUS) (Zanazzi et al., 2007; Fan et al., 2017), St. Stephens Quarry (SSQ) (Katz et al., 2008; Miller et al., 2008; Wade et al., 2012; Houben et al., 2019) and the United Kingdom (UK) discussed in the text (Hren et al., 2013).

the boundary is placed at the transition from the Shubuta Clay into the base of the Red Bluff Fm. The age model is based on the correlation of magnetic susceptibility data (χ) to the St. Stephens Quarry (SSQ) section (Fig. 4.3), which presents strong ~100 kyr eccentricity cycles that are comparable to the GSSP in Italy (Ellwood et al., 2019). The χ data for the Oligocene Red Bluff member within the HIW core shows the same 100-kyr-cyclicity as that at the

SSQ. However, the cyclicity of the Late Eocene Shubuta in the HIW core is twice that in the SSQ, indicating that the Shubuta Clay sediment accumulation rate in the HIW core is double that in the Eocene SSQ sequence (Ellwood et al., 2019) (Fig. 4.2). We compared the χ data from HIW core to that at the SSQ to derive the top (33.45 Ma) and bottom (34.13 Ma) ages for the HIW samples. Ages for HIW core samples within each χ zone were determined using linear interpolation, with each χ zone representing ~50 kyrs of time (Fig. 4.3). In this study, we place the E-O boundary at 33.8 Ma for comparing the our records with published proxy data, but it should be noted that the newest Geological Time Scale placed the E-O boundary at 33.9 Ma (Ogg et al., 2016).

The HIW core site, situated in the eastern part of Gulf Coastal Plain, is fed by the tropical maritime air masses (Joe Lambert and Aharon, 2010). The study area experienced moderate seasonality with an average monthly temperature ranging from ~9°C to 28°C, with an average monthly precipitation range from ~85 mm (fall) to ~185 mm (spring) (www.ncdc.noaa.gov). Convectional rainfall events (hurricanes, tropical storms) are dominant during summers, while a frontal style weather system controls the fall, winter, and spring precipitation due to the jet stream (Joe Lambert and Aharon, 2010). Interannual

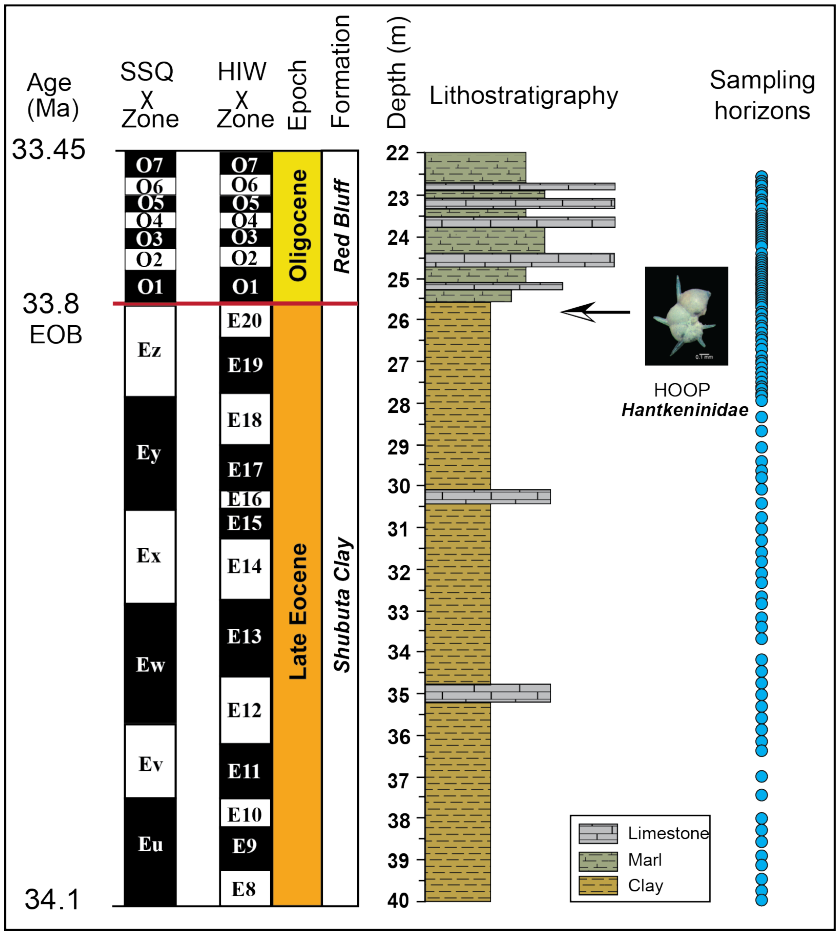

Figure 4.2. Age-depth relationship for the HIW core, from the late Eocene to the early Oligocene. The magnetic susceptibility data are from (Ellwood et al., 2019)

change in atmospheric circulation has been linked to the El Ninõ-Southern Oscillation and position of the Bermuda High that influences moisture transport during winter/early spring and summer/early fall seasons, respectively (Katz et al., 2003; Mo and Schemm, 2008; Joe Lambert and Aharon, 2010).

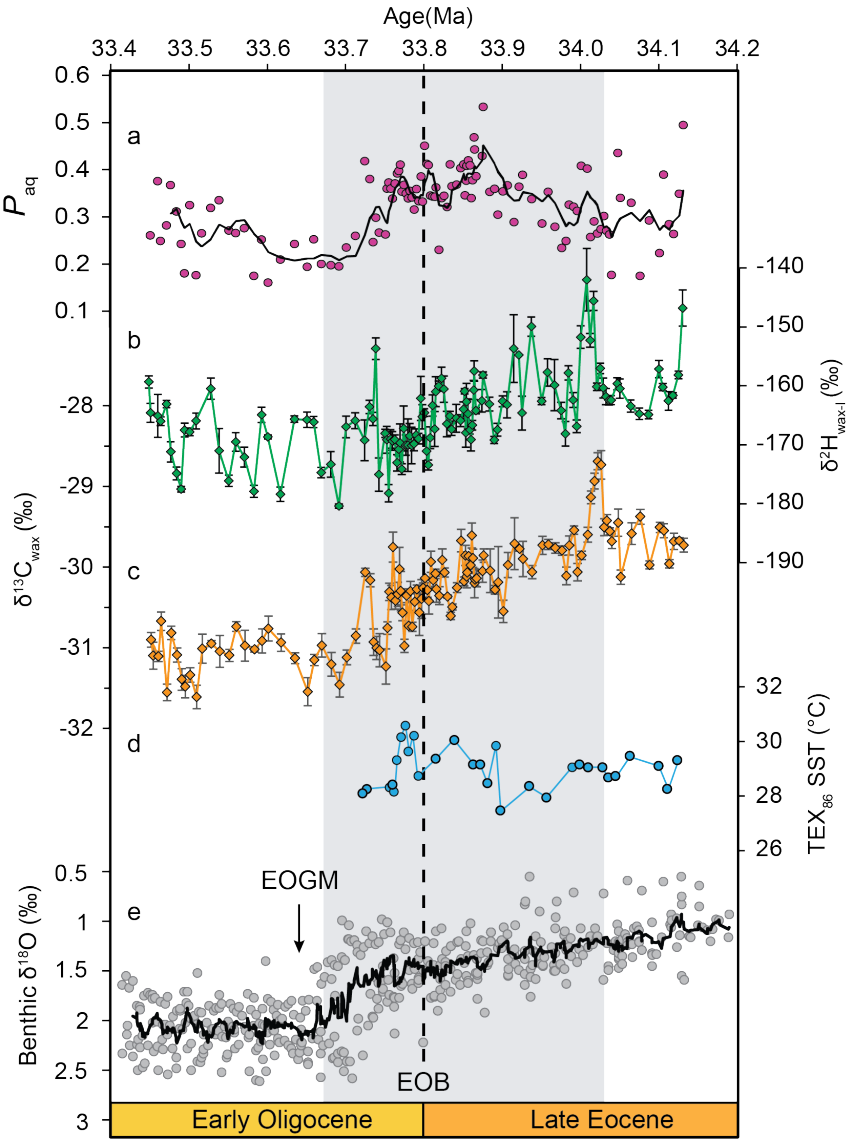

Figure 4.3. Lithostratigraphy and sampling horizons for the HIW core in the Mississippi, southeastern United States. Magnetic susceptibility data, interpretation of chronology, and fossil photos are adapted from Ellwood et al. (2019).

4.3. Methods and Materials

The HIW core was sampled at a 5 to 10 cm interval (119 samples) covering ~700 kyr from the uppermost Eocene Shubuta Clay Member to the lowermost Oligocene Red Bluff Formation of the Vicksburg Group (Ellwood et al., 2019). We studied the weighted-mean δ^2H_{wax} and $\delta^{13}C_{wax}$ values of long-chain n-alkanes (*n*-C_{27}, *n*-C_{29}, and *n*-C_{31}) from the Hiwannnee (HIW) core collected at the town of Haiwannee in Wayne county, southern Mississippi, United States (31.83°N; 88.69°W; Fig. 4.1). Given that the Antarctic ice sheet rapidly grows during the EOGM leading to an increase in seawater oxygen and hydrogen values, we subtracted the δ^2H enrichment caused by ice sheet growth to generate a record with the ice volume effect being removed ($\delta^2H_{wax\text{-}I}$). We then used $\delta^2H_{wax\text{-}I}$ and δ^2H_{wax} to quantify the change in mean annual precipitation (MAP) across the EOT, based on the empirical equations generated by the modern leaf carbon discrimination (Δleaf) –MAP relationship (Diefendorf et al., 2010) and precipitation δ^2H – MAP relationship (Joe Lambert and Aharon, 2010), respectively. We also measured the tetraether index (TEX_{86}) (Schouten et al., 2002) to reconstruct the SSTs of the GoM. The reconstructed hydrology and SST history are compared to contemporaneous terrestrial and oceanic proxy data to address the interaction between the ocean and atmosphere sys-

tems across the EOT.

4.3.1. Total Lipid extraction, Column Chromatography, and Characterization

Samples were broken and ground with mortar and pestle to a coarse-sand size and freeze-dried for 48 hours before extraction. Total lipids were extracted with Soxhlet extractors using the azeotrope of dichloromethane (DCM)/methanol 2:1 (v/v) for 48 hours. Total lipid extracts (TLE) were evaporated dry under a stream of purified nitrogen. Organic compounds in TLE were separated into apolar, intermediate, and polar fractions using a pipette column filled with ca. 0.5 grams of activated silica gel and sequentially eluted with 2 ml hexane, 4 ml DCM and 4 ml methanol.

n-Alkanes contained in apolar fractions were re-dissolved into 1500 µL of hexane. *n*-Alkanes abundances were determined using a Thermal Trace 1310 Gas Chromatography (GC)-flame ionization detector (FID) fitted with programmable-temperature vaporization (PTV) injector and TG-1MS column (60 m long, 0.25 mm i.d., 0.25 µm film thickness). Samples were carried by helium at a rate of 2 ml/min. GC oven temperature was programmed to ramp from 60 °C (thermal holding for 1 min) to 320 °C at 15 °C/min (holding for 20 min). Individual *n*-alkanes were identified by comparing the elution time with a reference standard (Mix A6, Schimmelmann, Indiana University Blooming-

ton).

Terrestrial vascular plants produced long-chain n-alkanes are dominated by a homologous series from *n*-C_{25} to *n*-C_{33}, with odd-over-even carbon number predominance (Eglinton and Hamilton, 1967a), expressed by the carbon preference index (CPI) :

$$\mathrm{CPI} = \frac{1}{2}\frac{\sum \mathrm{A}(23-33)\mathrm{odd} + \sum \mathrm{A}(25-35)\mathrm{odd}}{\sum \mathrm{A}(24-34)\mathrm{even}} \tag{4.1}$$

where A stands for the areas of individual *n*-alkane compounds, which are calculated by the integrating ion trace peaks from Gas Chromatography with the software Xcalibur.

P_{aq} index is used to reflect the relative contribution of leaf wax n-alkanes from aquatic macrophytes (*n*-C_{23} and *n*-C_{25}) versus terrestrial vascular plants (*n*-C_{29} and *n*-C_{31}) (Ficken et al., 2000). P_{aq} values were determined using the equation:

$$P_{\mathrm{aq}} = \frac{\mathrm{A}(23+25)}{\mathrm{A}(23+25+29+31)} \tag{4.2}$$

where A stands for the areas of individual *n*-alkane compounds in chromatography.

4.3.2. Leaf Wax Carbon Isotope Analysis

Leaf wax carbon isotope values were measured using Trace 1310 GC coupled to a Thermo Delta V Advantage isotope ratio mass spectrometer (IRMS) with a Thermo Isolink interface. Trace 1310 GC was fitted with PTV injector and TG-5MS column (30 m long, 0.25 mm i.d., 0.25 µm film thickness). Samples were carried by helium at a rate of 2 ml/min. Compounds were separated by the GC with the temperature being programmed to ramp from 60 °C (held for 2 min) to 170 °C at 14 °C/min, to 300 °C at 3 °C/min, and then to 320 °C at 14 °C/min with an isothermal holding of 5 mins. The duplicate analysis was applied to each sample with a mean analytical precision of 0.1‰ for $\delta^{13}C$. The n-alkane reference materials Mix A6 (n-C_{16} to n-C_{30}; Arndt Schimmelmann, Indiana University) were measured every four to six analyses to monitor instrumental drift. Carbon isotope ratio values were calibrated relative to Mix A6 and reported relative to Vienna Pee Dee Belemnite (VPDB) and expressed in per mil (‰):

$$\delta^{13}C = \left(\frac{R_{sample}}{R_{reference}} - 1\right) \tag{4.3}$$

where R represents the $^{13}C/^{12}C$ ratios in samples and standard reference materials. The weighted mean $\delta^{13}C$ values of n-C_{27}, n-C_{29}, and n-C_{31} are calculated

as follows:

$$\delta^{13}C_{wax} = \frac{\sum A_i \times \delta^{13}C_i}{\sum A_i} \tag{4.4}$$

where A stands for the areas of n-alkanes with i (27-31) indicating carbon chain-length.

4.3.3. Leaf Wax Hydrogen Isotope Analysis

Leaf wax hydrogen isotope values were measured by the same GC-Isolink-IRMS system with the High Temperature Conversion (HTC) configuration. GC and column settings were identical to those used in the carbon isotope analysis. H_3^+ factor was measured three times daily before the isotopic analysis. The duplicate analysis was applied to each sample with a mean analytical precision of 1.6 ‰ for δ^2H. The *n*-alkane reference materials (Mix A6) were measured every four to six analyses for monitoring instrumental drift. Hydrogen isotope ratio values were calibrated relative to Mix A6 and reported relative to Vienna Standard Mean Ocean Water (VSMOW). Hydrogen isotopic compositions were determined using the following equation and expressed in per mil (‰):

$$\delta^2H = \left(\frac{R_{sample}}{R_{reference}} - 1\right) \tag{4.5}$$

where R represents the $^{2}H/H$ ratios in samples and reference materials. The weighted mean $\delta^{2}H$ values of *n*-C_{27}, *n*-C_{29}, and *n*-C_{31} are calculated as follows:

$$\delta^{2}H_{wax} = \frac{\sum A_i \times \delta^{2}H_i}{\sum A_i} \tag{4.6}$$

where A stands for the areas of *n*-alkanes with *i* (27-31) indicating carbon chain-length.

4.3.4. GDGTs Analysis

Methanol fraction containing GDGTs was analyzed using an Agilent 1290series UPLC system that was coupled to an Agilent 6530 qTOF mass spectrometer through an Aglient jet stream dual electrospray ionization (AJS-ESI) interface, following the methodology of Liu et al. (2019). We used the relative abundance of GDGTs to derive the TEX_{86} index values that were converted to the SSTs by applying a linear $TEX_{86}{}^{H}$-SST relationship (Kim et al., 2010). We also provide calibration results, using a linear relationship as done by Schouten et al. (2002), and a Bayesian regression model (BAYSPAR) (Tierney and Tingley, 2014).

4.3.5. Removal of Ice Volume Effects from $\delta^{2}H_{wax}$ Records

The rapid growth of the Antarctic ice sheet during the EOGM (~33.65 Ma) causes the enrichment of $\delta^{2}H$ in seawater and thus influences leaf wax

δ^2H_{wax} values for samples younger than 33.65 Ma. Previous studies of marine $\delta^{18}O$ records reveal a 0.6‰ enrichment in seawater $\delta^{18}O$ due to the Antarctic Glaciation (Katz et al., 2008; Miller et al., 2008). Hence, we corrected the ice volume effects on our δ^2H_{wax} record as follows:

1. We use the slope of the local meteoric water line (7.2) from the IAEA station in Alabama (Joe Lambert and Aharon, 2010) to convert the changes in seawater $\delta^{18}O$ to δ^2H. The change of 0.6‰ in seawater $\delta^{18}O$ is equivalent to a 4.3‰ change in δ^2H. We assume that change in seawater δ^2H is reflected in precipitation δ^2H_p.

2. The relationship between hydrogen isotopic composition of leaf waxes (δ^2H_{wax}) and precipitation water (δ^2H_p) is defined by the equation:

$$\varepsilon_{wax/p} = \frac{\delta^2H_{wax} + 1}{\delta^2H_p + 1} - 1 \tag{4.7}$$

   $\varepsilon_{wax/p}$ is used to characterize the apparent fractionation δ^2H_{wax} and δ^2H_p, and are reported as per mil (‰) (Sachse et al., 2012). During the late Eocene and early Oligocene, warm temperate forests are predominant in the southeastern United States (Oboh-Ikuenobe and Jaramillo, 2003), and there is little C_4 grassland before the early Miocene (Tipple and Pagani, 2010). Thus, we use the average $\varepsilon_{wax/p}$ value (~130‰) derived from *n*-C_{29} of North America C_3 forest (Hou et al., 2007) to convert the change in δ^2H_p to the equivalence of 4.9‰ in δ^2H_{wax}.

3. We subtract the ice volume induced δ^2H_{wax} enrichment (4.9‰) from samples that are younger than 33.8 Ma to obtain an ice-volume corrected $\delta^2H_{wax\text{-}I}$ record.

4.3.6. Evaluation of TEX_{86} Based SSTs

TEX_{86} (TetraEther indeX with 86 carbon atoms) paleothermometry is based on the cyclicity of membrane lipids in marine archaea - glycerol di-

alkyl glycerol tetraethers (GDGTs) that can be converted to SST (Schouten et al., 2002). TEX_{86} has been extensively used for paleoclimatic reconstruction because of its ubiquitous occurrence in marine sediments and robustness to diagenesis (Huguet et al., 2009; Kim et al., 2009). Reconstruction of SST from TEX_{86} requires tests to justify that temperature is a primary control on GDGT distribution. Non-thermal factors, including input of terrigenous organic matter and methanogenic archaeal communities and growth phases of archaea, can influence GDGT distribution and lead to a considerable error in SST estimation (Hopmans et al., 2004; Liu et al., 2011; Elling et al., 2014). To validate the reliability of TEX_{86}^{H} - based SST reconstruction, we use the Branched and Isoprenoid Tetraethers (BIT) index (Hopmans et al., 2004), Methane Index (MI) (Zhang et al., 2011), ΔRing Index (ΔRI) (Zhang et al., 2016), and %GDGT-0 (Inglis et al., 2015) to evaluate the potential impacts of non-thermal factors and applicability of the TEX_{86} - SST relationship.

The BIT index is based on the relative abundance of terrestrially derived tetraether lipids (branched GDGTs) versus the *crenarchaeol* (isoprenoid GDGT) produced by marine or lacustrine organic matter (Hopmans et al., 2004). A BIT value of 0.4 is recommended as the limit to differentiate a marine source with soil bacteria-derived GDGTs (Weijers et al., 2006). Samples with high BIT

values (BIT > 0.4) are possibly influenced by substantial input of terrestrial organic matter and thus are not used for SST reconstruction. The BIT index is calculated using the following equation:

$$\mathrm{BIT} = \frac{[\mathrm{GDGT–I}] + [\mathrm{GDGT–II}] + [\mathrm{GDGT–III}]}{[\mathrm{GDGT–I}] + [\mathrm{GDGT–II}] + [\mathrm{GDGT–III}] + [\mathrm{Crenl}]} \tag{4.8}$$

Methanotrophic archaea *Euryarchaeota* that live in both moderate and extreme environments, in terms of temperature and salinity, also produce GDGTs. The methane index is used to differentiate the input of methanotrophic archaea from normal marine communities (Zhang et al., 2011). An MI value < 0.3-0.5 indicates a normal marine setting, while an MI value of > 0.5 suggests a methane hydrate-impacted setting. The methane index is calculated using the following equation:

$$\mathrm{MI} = \frac{[\mathrm{GDGT–1}] + [\mathrm{GDGT–2}] + [\mathrm{GDGT–3}]}{[\mathrm{GDGT–1}] + [\mathrm{GDGT–2}] + [\mathrm{GDGT–3}] + [\mathrm{Cren}] + [\mathrm{Cren'}]} \tag{4.9}$$

where RI is defined as the weighted average of ring (cyclopentane) numbers in the GDGTs.

Modern marine measurements indicate a significant correlation between RI and TEX_{86}. A deviation (ΔRI) from the modern TEX_{86}-RI relationship can be used to detect non-thermal factors that are incorporated in the TEX_{86}

index. Samples with ΔRI > 0.3 are likely to be influenced by additional tetraether input. ΔRI is expressed as follows:

$$\mathrm{RI} = 0 \times [\mathrm{GDGT{-}0}] + 1 \times [\mathrm{GDGT{-}1}] + 2 \times [\mathrm{GDGT{-}2}] + 3 \times [\mathrm{GDGT{-}3}] + 4 \times [\mathrm{Cren}] + 4 \times [\mathrm{Cren'}] \tag{4.10}$$

$$\mathrm{RI_{TEX}} = -0.77(\pm 0.38) \times \mathrm{TEX_{86}} + 3.32(\pm 0.34) \times (\mathrm{TEX_{86}})^2 + 1.59(\pm 0.10) \tag{4.11}$$

$$\Delta\mathrm{RI} = \mathrm{RI_{TEX}} - \mathrm{RI} \tag{4.12}$$

where ΔRI stands for the offset between samples (RI) and modern TEX_{86}-RI relationship. The quadratic regression between RI_{TEX} and TEX_{86} is derived from the global ocean data set (Zhang et al., 2016).

The %GDGT-0 index was used to evaluate the contribution of methanogenic archaea to the sedimentary GDGTs. Samples with %GDGT-0 values higher than 67% are potentially influenced by additional organic sources from methanogenic *Euryarchaeota* (Inglis et al., 2015). The %GDGT-0 index is calculated as,

$$\%\mathrm{GDGT{-}0} = (\mathrm{GDGT{-}0}/(\mathrm{GDGT{-}0} + \mathrm{Crenarchaeol})) \times 100 \tag{4.13}$$

The GDGTs distribution from the HIW core shows a wide range of BIT values (0.17-0.88). The age of 33.85 Ma is a cut-off for separating GDGT distribution from high BIT values (mean BIT = 0.75) in the early Oligocene to relative low BIT values (mean BIT = 0.43) from the late Eocene (Fig. 4.4). This major increase in BIT values tracks the decrease in P_{aq} values (Fig. 4.4), and we infer that the samples with high BIT values are most likely the result of a eustatic sea-level fall and thus a landward shift of organic source. The substantial high BIT values (>0.7) during the late Oligocene indicate that these samples are less reliable for SST reconstruction due to this significant terrigenous input. Investigation of modern soil branched GDGTs distribution shows that temperature deviation can be greater than 2°C when BIT values exceed 0.4 (Weijers et al., 2006).

However, further study found that in some localities (e.g., ODP sites 925 and 929), samples with high BIT values (>0.4) show similar SST estimation as those with low BIT values (<0.1) (Inglis et al., 2015). In the HIW core, while the early Oligocene samples exhibit relatively high BIT values (mean BIT = 0.75), the late Eocene samples have mean BIT values of 0.43, close to the threshold of 0.4 for a conservative SST reconstruction. We have compared SST values between samples with BIT < 0.4 and samples with 0.4 < BIT < 0.5.

The result shows that SSTs from samples with high BIT values did not exhibit resolvable deviation (exceeding the analytical error of ±1°C) from SSTs from samples with low BIT values (Fig. 4.4). In addition, there is no correlation between the BIT values and SSTs when the BIT values are smaller than 0.5 (Fig. 4.5). This implies that the higher-than-threshold BIT values ($0.4 < BIT < 0.5$) may not bias the SSTs reconstruction from TEX_{86}. Thus, we have concluded that the late Eocene samples with $0.4 < BIT < 0.5$ can be used for SST reconstruction. In addition, we further evaluated the potential influence of methanogenic *Euryarchaeota* on the GDGTs distribution by examining the ΔRI, %GDGT-0, and MI values. For late Eocene samples, the average ΔRI (0.38) is close to the threshold of 0.3, and the average MI value (0.39) reaches the upper limit for normal marine settings (0.3-0.5). However, the mean %GDGT-0 (40%) is much smaller than the threshold of 67%. Hence, we argue that the impact of methanogens is negligible.

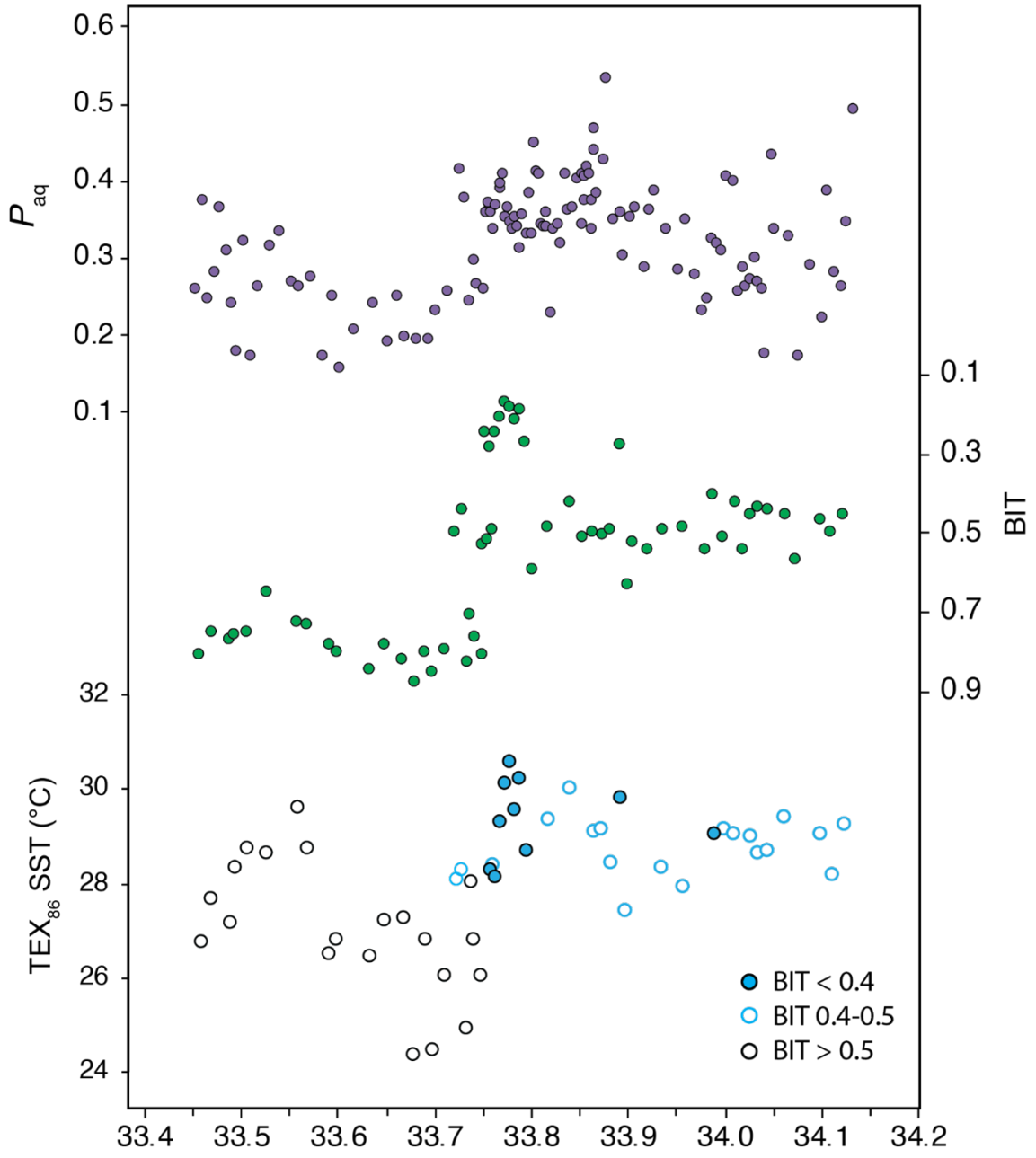

Figure 4.4. Comparison among TEX86 SSTs, BIT, and Paq values.

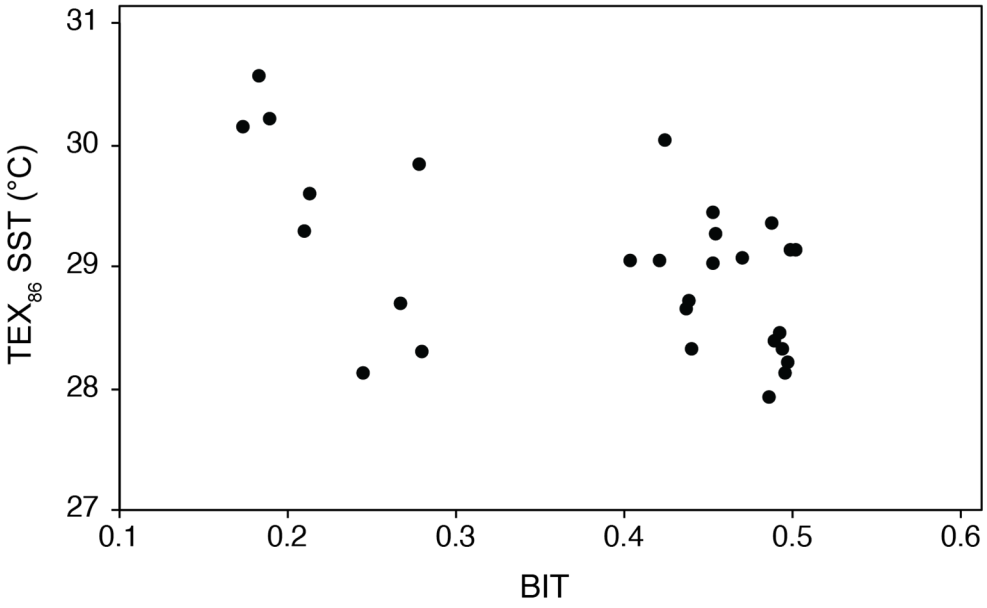

Figure 4.5. Comparing the relationship between the BIT values and the TEX86 SST for the late Eocene samples with BIT values between 0.4 and 0.5.

4.4. Results and Discussions

4.4.1. *n*-Alkanes Characteristics and Evidence for Sea-level Fall

Plant cuticular waxes coat on the leaf surface to maintain the water balance and to prevent physical damage to the leaf cells. *n*-Alkanes, as one of the major compounds consisting of leaf waxes, are ubiquitously preserved in almost all types of sedimentary environments. A rigorous cut-off of CPI values for terrestrial higher plant sources has been suggested to be greater than 2 (Bush and McInerney, 2013). Samples with CPI values near 1 are suspected to be influenced by thermal alteration or degradation after deposition. CPI values

range from 2.2 to 4.0, indicating that the HIW sediments are less likely to be influenced by post-depositional alteration.

P_{aq} values vary between 0.2 and 0.5 in the whole series, with a marked decrease of ~0.2 at 33.69 Ma (Fig. 4.6A). This drastic change is synchronous with the Early Oligocene Glacial Maximum (EOGM), which indicates an increase in terrestrial organic matter input, which may have resulted from rapid eustatic fall driven by Antarctic glaciation. Marine $\delta^{18}O$ and Ca/Ma records from nearby successions in St. Stephens Quarry (SSQ) site Alabama support the major drop of sea level in the Gulf of Mexico associated with the timing of the EOGM (Katz et al., 2008; Miller et al., 2008).

4.4.2. Hydrological History in the GoM during the EOT

$\delta^{13}C_{wax}$ values at HIW decrease by ~1.6‰ across the EOT, with mean value shifts from -29.5‰ at the late Eocene to -31.1‰ after the EOGM (Fig. 4.6B). The change of $\delta^{13}C_{wax}$ values is synchronous with the positive shift in benthic foraminifera $\delta^{18}O$ records of the global dataset (Figs. 4.6B and 4.6E). $\delta^{13}C_{wax}$ is a function of the $\delta^{13}C$ of atmospheric CO_2 ($\delta^{13}C_{atm}$) and photosynthetic fractionation during carbon fixation (Farquhar et al., 1982). Photosynthetic fractionation is modulated by both physiological (photosynthetic pathways) and environmental (water stress) variables. Plants with different

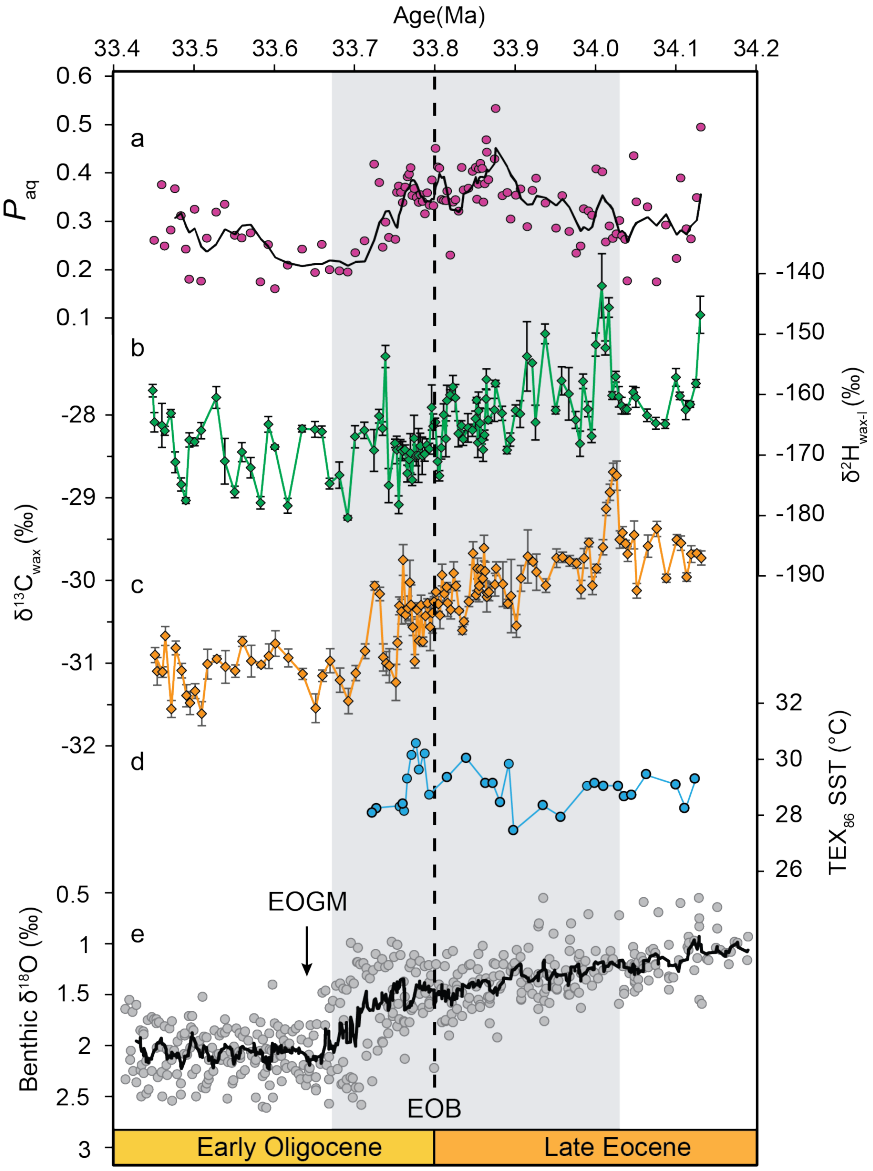

Figure 4.6. Paleoclimatic reconstruction in the GoM based on leaf wax carbon and hydrogen isotopes and TEX_{86} SSTs. A, P_{aq} record. B, $\delta^2H_{wax\text{-}I}$ record. C, $\delta^{13}C_{wax}$ record. D, TEX_{86} SSTs. SSTs with BIT $<$ 0.4 (solid circles); SSTs with $0.4 < BIT < 0.5$ (empty circle); SSTs with BIT > 0.5 are not reported due to high terrestrial organic input. E, a global compilation of benthic $\delta^{18}O$ records with the black line representing a 10-point moving average (Cramer et al., 2009). The shaded bar denotes the EOT interval.

photosynthetic pathways can result in distinct carbon isotopic signatures. C_3 (Calvin-Benson) carbon fixation pathways have larger fractionation than the C_4 (Hatch-Slack) pathway (Diefendorf and Freimuth, 2017). Therefore, the mean $\delta^{13}C_{wax}$ values for C_3 plants are ~ -33‰, whereas the mean value for C_4 plants is ~ -22‰. $\delta^{13}C_{wax}$ data from the HIW site range from -31.6‰ to -28.7‰, thus indicating that C_3 plants were dominant in the Gulf Coast region during the early Oligocene and the late Eocene. Our results are comparable to the $\delta^{13}C_{wax}$ records from the Gulf of Mexico during the same time interval (Tipple and Pagani, 2010). Variation of $\delta^{13}C_{wax}$ values in HIW reflect a change in Δleaf, as the $\delta^{13}C_{atm}$ is relatively constant across the EOT based on benthic foraminifera $\delta^{13}C$ records (Tipple et al., 2010). Water stress predominantly controls Δleaf through regulating leaf gas-exchange via constraints on stomatal conductance. Thus, plant carbon isotope fractionation is strongly correlated with mean annual precipitation of C_3 plants that hibit lower $\delta^{13}C_{wax}$ values when precipitation amounts are high (Diefendorf et al., 2010). We argue that the 2‰ negative shift of $\delta^{13}C_{wax}$ values in HIW implies an increase in precipitation in the GoM through the EOT.

$\delta^{2}H_{wax\text{-}I}$ record shows a ~10‰ negative shift in 310 kyr (ca. 34.00-33.69 Ma) across the EOT, which is coeval with the negative shift in $\delta^{13}C_{wax}$

values (Figs. 4.6B and 4.6C). Mean $\delta^2H_{wax\text{-}I}$ values change from -158‰ before the EOT to -169‰ after the EOGM. δ^2H_{wax} from modern lake sediments reflects the hydrogen isotopic composition of source waters and varies among plant forms due to biosynthetic differences (Hou et al., 2008; Sachse et al., 2012). As the primary control of δ^2H_{wax} values, precipitation δ^2H changes as a function of temperature, precipitation amount, evaporation, and other climatic factors. δ^2H_{wax} has been used to reconstruct the long-term hydrologic evolution of the Great Plains of North America since the late Eocene (Tipple and Pagani, 2010). The present study focuses on the change in paleoclimate in the Gulf Coasts across the EOT. Variation of interannual precipitation δ^2H in the Gulf Coast mainly reflects changes in rainfall amount, with lower δ^2H values indicating increasing precipitation and vice versa (Joe Lambert and Aharon, 2010). Seasonal and annual temperatures have little influence on the precipitation isotope values ($\delta^{18}O$ and δ^2H) in the US Gulf Coast (Vachon et al., 2010), due to a weak seasonality in the Gulf Coast and single moisture source from tropical maritime air masses (Joe Lambert and Aharon, 2010). Thus, we interpret that the negative shift in $\delta^2H_{wax\text{-}I}$ across the EOT represents an increase in precipitation amount.

Change in plant communities should have a negligible effect on $\delta^{13}C_{wax}$

and $\delta^2H_{wax\text{-}I}$ values in the HIW core across the EOT. Studies on modern plants suggest that plant carbon and hydrogen isotopes vary among taxonomy groups (Diefendorf et al., 2010; Sachse et al., 2012). For example, carbon isotopic fractionations in gymnosperms are ~ 3-5‰ less than in angiosperms, which results in higher $\delta^{13}C_{wax}$ values for conifers than angiosperms (Diefendorf et al., 2011). Hydrogen isotopic fractionation for graminoids is more depleted than trees and shrubs by ~30‰ (Sachse et al., 2012). Gulf Coast regions were dominated by tropical to subtropical forest assemblages during the late Eocene and the early Oligocene; for example, *Quercoidites*, *Sequoiapollenits*, *Cupressacites*, and *Cyrillaceaepollenites* (Oboh-Ikuenobe and Jaramillo, 2003). Although *Quercoidites* increase slightly during the Oligocene, there is no significant paleofloristic change and turnover across the Eocene/Oligocene boundary (Oboh-Ikuenobe and Jaramillo, 2003).

4.4.3. $\delta^2H_{wax\text{-}I}$ and $\delta^{13}C_{wax}$ Based Rainfall Reconstruction

We use $\delta^2H_{wax\text{-}I}$ and wax records to generate two independent reconstructions of precipitation across the EOT. The change in precipitation is calculated relative to the mean annual precipitation during the latest Eocene (prior to 34.0 Ma). Then, we compare and evaluate the reconstructions of precipitation based on $\delta^2H_{wax\text{-}I}$ and $\delta^{13}C_{wax}$ records.

The reconstruction of precipitation using $\delta^{13}C_{wax}$ is based on a compilation of leaf discrimination (Δ_{leaf}) values as a function of mean annual precipitation (Diefendorf et al., 2010). Conversion from $\delta^{13}C_{wax}$ to Δ_{leaf} involves two processes: (1) fractionation between $\delta^{13}C$ of the bulk leaf ($\delta^{13}C_{leaf}$) and $\delta^{13}C$ of the atmosphere ($\delta^{13}C_{atm}$) and (2) fractionation between $\delta^{13}C_{leaf}$ and $\delta^{13}C_{wax}$, expressed by the equations:

$$\Delta_{leaf} = \left(\frac{\delta^{13}C_{atm} + 1}{\delta^{13}C_{leaf} + 1} - 1\right) \times 10^3 \tag{4.14}$$

$$\varepsilon_{leaf} = \left(\frac{\delta^{13}C_{wax} + 1}{\delta^{13}C_{leaf} + 1} - 1\right) \times 10^3 \tag{4.15}$$

Where $\delta^{13}C_{atm}$ is ~-6‰ during this interval (Tipple et al., 2010). $\delta^{13}C_{leaf}$ is the carbon isotopic composition of the bulk leaf.

The biosynthetic fractionation (ε_{leaf}) between $\delta^{13}C_{wax}$ of long-chain *n*-alkanes (*n*-C_{27}, *n*-C_{29}, and *n*-C_{31}) and bulk leaf $\delta^{13}C_{leaf}$ is ~ -5‰ for C_3 plant, based on the compilation of modern plants (Tipple and Pagani, 2010; Diefendorf and Freimuth, 2017). Analysis of woody C_3 plants from the global dataset indicates that Δ_{leaf} is linearly correlated with the log of the mean annual precipitation (MAP) (Diefendorf et al., 2010). To quantify the change of MAP in HIW during the EOT, we calculated the Δ_{leaf} of our $\delta^{13}C_{wax}$ records,

and then employed an empirical Δ_{leaf} – MAP relationship:

$$log(\text{MAP}) = 0.10(\pm 0.04) \times \Delta_{\text{leaf}} + 1.01(\pm 0.08)\ (R = 0.73, n = 105) \qquad (4.16)$$

Data used for deriving the equation are from a global compilation of modern plant by Diefendorf et al. (2010) and new data for trees in the Gulf Coast region. $\delta^{13}C_{wax}$ reconstructed precipitation amounts increase from an average of 818 mm during the latest Eocene (before 34.0 Ma) to 1175 mm during the early Oligocene (33.45-33.70 Ma) (Figs. 4.7 and 6D), which is equivalent to an increase of 44% in precipitation across the EOT. The predicted MAP within a 90% confidence interval ranges from 349 mm to 1929 mm during the late Eocene and ranges from 502 mm to 2771 mm during the early Oligocene (Table S2). This large MAP range possibly results from genetic variability among plant species (Ehleringer et al., 1991; Diefendorf and Freimuth, 2017).

However, if this empirical relationship is valid for individual plant species and the composition of plant communities is stable, the error of MAP reconstruction is likely to shift the predicted precipitation amount as a whole but is unchanged for MAP change in proportion (MAP%). Pollen data indicate a stable plant assemblage in the Gulf Coast regions. Hence, we argue that

MAP% in HIW is reliable for predicting precipitation change across the EOT.

We use modern meteorological data from the meteorological station in Alabama (Joe Lambert and Aharon, 2010) to generate an empirical relationship between precipitation δ^2H and MAP. Only weekly data is reported for the region, showing a correlation between weekly precipitation amount and precipitation δ^2H. We assume that the observed relationship between the weekly amount of precipitation and the precipitation δ^2H hold for annual precipitation and thus convert the weekly amount to the annual amount by multiplying a coefficient of 52. The precipitation δ^2H is then converted to $\delta^2H_{wax\text{-}I}$ values by applying a fractionation factor of 130‰ to equation (4.7). The derived $\delta^2H_{wax\text{-}I}$ values linearly correlate with MAP, with the low $\delta^2H_{wax\text{-}I}$ values correlated with high precipitation. The equation expresses the relationship between MAP and $\delta^2H_{wax\text{-}I}$ values:

$$\delta^2H_{wax\text{-}I} = -12.5 \times log(\text{MAP}) - 108.4 \; (R = 0.45, n = 118) \tag{4.17}$$

The $\delta^2H_{wax\text{-}I}$ reconstruction shows increases of MAP from 1,514 mm before 34.10 Ma, to 2,269 mm between 33.45-33.70 Ma, equivalent to a 50% increase in precipitation (Figs. 4.8 and 4.9D). The calculated precipitation amount from $\delta^2H_{wax\text{-}I}$ is higher than the result from the $\delta^{13}C_{wax}$ record.

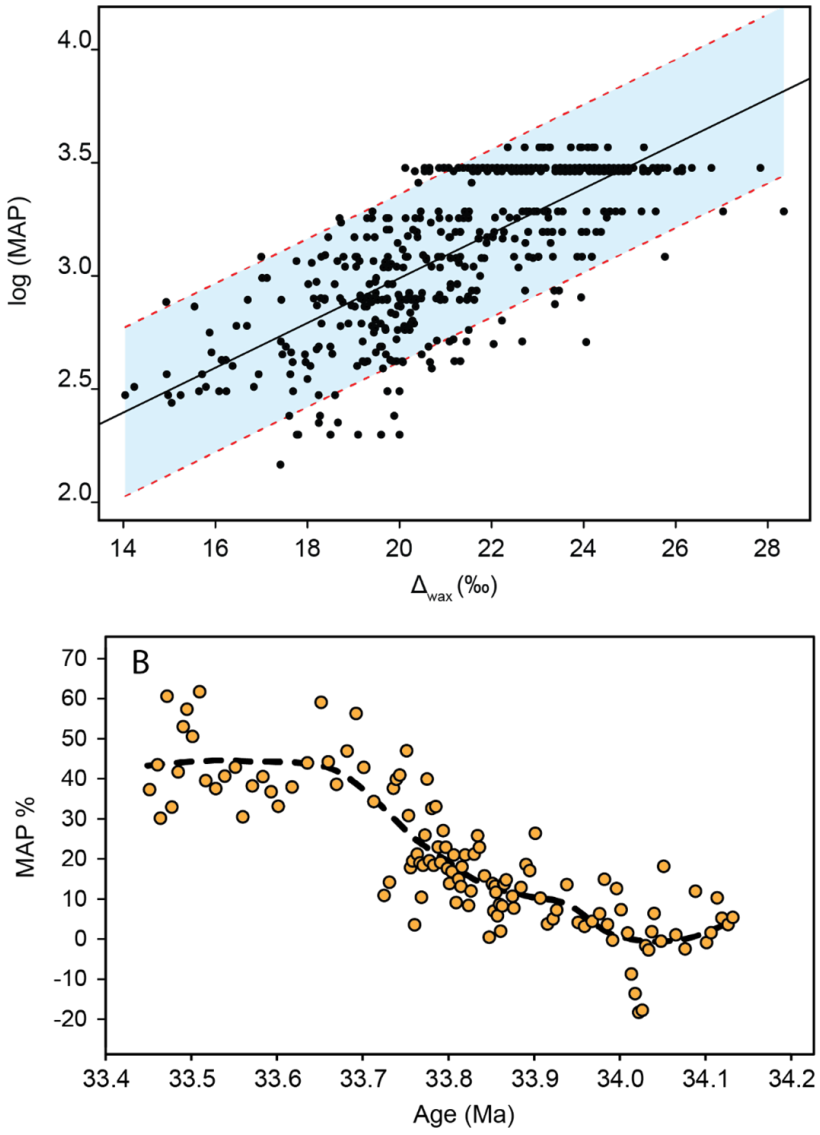

Figure 4.7. Mean annual precipitation reconstruction based on Δ_{leaf} . A, a linear relationship between Δ_{leaf} and *log*(MAP). MAP (mean annual precipitation, in mm). The Δ_{leaf} and MAP data are adapted from Diefendorf et al. (2010). The shaded area denotes the 90% confidence interval. B, change of mean annual precipitation in proportion (MAP%) at HIW across the EOT is reconstructed by using the $\delta^{13}C_{wax}$ record. The dashed line is generated by local regression. MAP% are calculated relative to the mean values for the late Eocene (before 34.0 Ma) and are reported in percentage (%).

δ^2H_{wax}-based MAP% resembles the estimation from the $\delta^{13}C_{wax}$ record (Figs. 4.7 and 4.8).

4.4.4. Interhemispheric Temperature Asymmetry across the EOT

The TEX_{86} SSTs at HIW (Fig. 4.6D) increases from 28°C to 31°C from 34.1 Ma to 33.8 Ma and decreases ~3°C within the following 50 ka (33.8 Ma-33.75 Ma). While samples younger than 33.75 Ma show high terrestrial branched glycerol dialkyl glycerol tetraethers (br-GDGT) input, we performed multifarious quantitative and correlation analyses and show here that samples with a BIT < 0.5 are best to constrain the SST variations (Fig. 4.4). Our TEX_{86} SST records show similar cooling magnitudes to the SSTs at SSQ (Wade et al., 2012). In addition, our new SST records capture a secular warming trend within ~300 ka before this cooling, which is concordant with the increasing SST in the GoM and equatorial Atlantic during the late Eocene (Tremblin et al., 2016; Houben et al., 2019). The warming at low latitudes during the late Eocene might have reflected an increasing heat accumulation in the tropical and subtropical Atlantic, which can be linked to an invigoration of modern-like AMOC (Tremblin et al., 2016; Elsworth et al., 2017). This inference is supported by the increasing meridional benthic foraminiferal $\delta^{18}O$ gradient among the Atlantic and the Southern Ocean (Cramer et al., 2009)

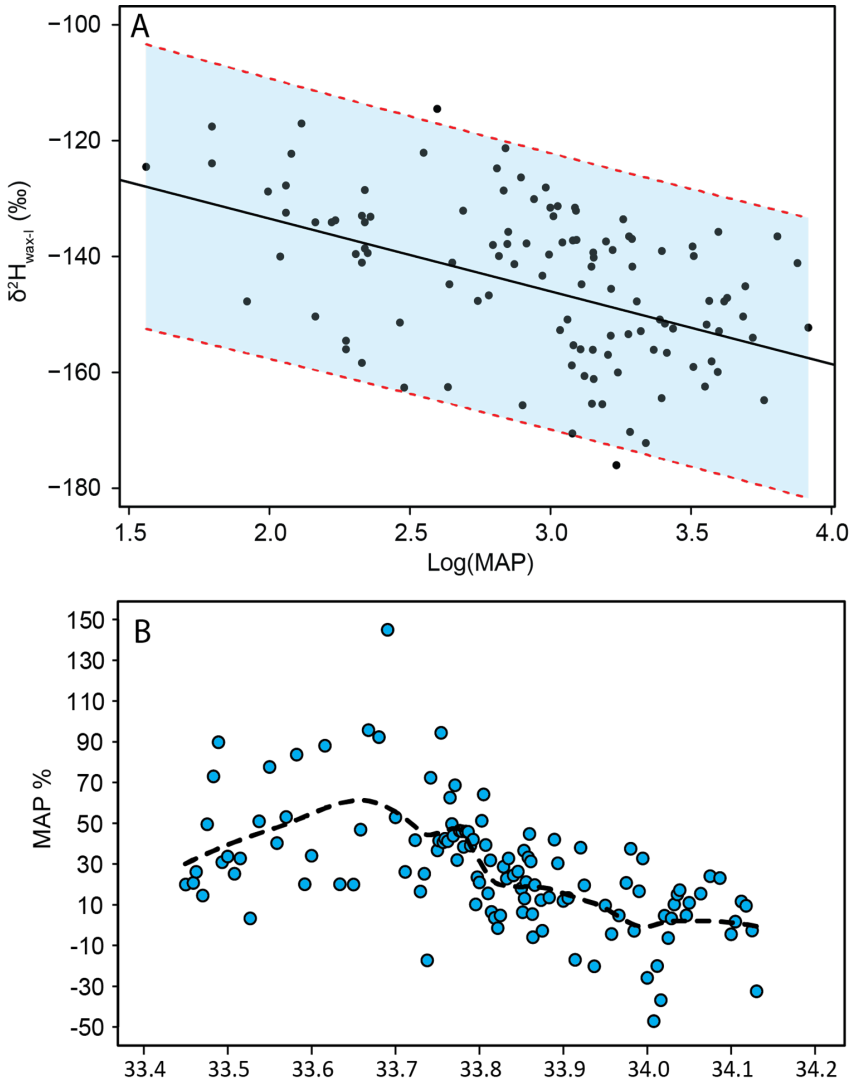

Figure 4.8. Mean annual precipitation reconstruction based on δ^2H_{wax}. A, a linear relationship between δ^2H_{wax} and *log*(MAP). MAP (mean annual precipitation, mm). δ^2H_{wax} values are converted from δ^2H of precipitation using the equation (4.7) and regional meteorological data from the IAEA station in Alabama (Joe Lambert and Aharon, 2010). The shaded area denotes the 90% confidence interval. B, change of mean annual precipitation in proportion (MAP%) at HIW across the EOT is reconstructed by using the $\delta^2H_{wax\text{-}I}$ record. The dashed line is generated by local regression. MAP% are calculated relative to the mean values for the late Eocene (before 34.0 Ma) and are reported in percentage (%).

and enhanced vertical mixing between Atlantic intermediate and deep water inferred by the collapse in the planktic-benthic $\delta^{13}C$ gradient (Abelson and Erez, 2017; Coxall et al., 2018). The warming of SST in HIW during the late Eocene supports the presence of modern-like AMOC in the Atlantic, which result in northward heat transport and a warmer Northern Hemisphere than the Southern Hemisphere (Buckley and Marshall, 2016).

Our TEX_{86} temperatures agree with other temperature proxy data and benthic $\delta^{18}O$ records, revealing that SST decreases weakly across the EOT in the subtropics and Northern Hemisphere relative to the Southern Hemisphere (Lear et al., 2008; Cramer et al., 2009; Liu et al., 2018). The magnitude of change in SST at the HIW core location is consistent with the $U^{K'}_{37}$ SST data from Site 1404 in the North Atlantic (Fig. 4.9B), where SST decreases less than 2°C associated with the EOT (Liu et al., 2018). In addition, terrestrial paleoclimate proxy data from the Northern Hemisphere (Fig. 4.9A) also show a delayed cooling that does not begin until the EOGM at ~33.67 Ma. Temperature proxy data from continental North America suggest a more pronounced cooling (~7-8°C) from the late Eocene into the early Oligocene (Zanazzi et al., 2007; Hren et al., 2013; Fan et al., 2017), while the major phase of cooling occurs after ~33.6 Ma. Contrary to the Northern Hemisphere, the $U^{K'}_{37}$ SST

from site 511 in the southern ocean (Fig. 4.9B) strikingly declines during the late Eocene, which is ~0.5-1 Ma earlier than the cooling in the Northern Hemisphere (Liu et al., 2009). This asymmetric temperature pattern across the EOT cannot be attributed to the drop of pCO_2 alone, which is supposed to cool the global temperature synchronously. Climate simulation and proxy data propose that the southern-northern temperature difference is associated with the establishment of the Antarctic ice sheet that intensifies the meridional temperature gradient and invigorates ocean circulation (Goldner et al., 2014; Liu et al., 2018).

4.4.5. Northward Shift of the Intertropical Convergence Zone (ITCZ) Driven by Hemispherically Asymmetric Temperatures

The increase in precipitation is synchronous with a positive shift in global marine $\delta^{18}O$ records (Cramer et al., 2009) and cooling of southern high-latitude temperatures (Liu et al., 2009) (Fig. 4.9B, 4.9C, and 4.9D), indicating that the hydrological change along the Gulf Coast is associated with changes in meridional temperature gradients and reorganization in the ocean and atmospheric circulation. We argue that interhemispheric temperature asymmetry has intensified the meridional pressure gradient that caused a northward migration of ITCZ, with enhanced rainfall in GoM regions. Millennial-scale climate modeling for glacial-interglacial cycles has suggested that the ITCZ

displacement is sensitive to extratropical cooling. This interhemispheric asymmetric temperature gradient impacts the Hadley and eddy circulation and forces the ITCZ to shift toward relatively warmer regions by alternating atmospheric heat exchange between the tropics and mid-latitudes (Broccoli et al., 2006; Chiang and Friedman, 2012). Substantial cooling of the Southern Hemisphere across the EOT, relative to the Northern Hemisphere, potentially shifts the ITCZ to the Northern (relatively warmer) Hemisphere. In the GoM, this northward positioning of the ITCZ can result in higher-than-normal precipitation in GoM coastal regions, as represented by lower $\delta^{13}C_{wax}$ and $\delta^{2}H_{wax\text{-}I}$ values.

The northward shift of the ITCZ, with enhanced precipitation in GoM regions, is consistent with a climate simulation that predicts an increase in annual precipitation by 20-100% in the tropics and subtropics driven by a strengthened AMOC (Elsworth et al., 2017). This enhanced precipitation subsequently prompted silicate weathering and drawdown in pCO_2. The northward migration of the ITCZ is supported by a dust provenance study from the central equatorial Pacific site 1334, suggesting a northward shift of the rain belt across the EOT (Hyeong et al., 2016). This displacement of the ITCZ appears to have been a rapid change, which is identical to the transient nature of

hemispherically asymmetric temperature patterns (Liu et al., 2018). After the rapid growth of the Antarctic ice sheet at the onset of the EOGM, this northward shift of the ITCZ, along with precipitation intensification in the subtropics, was likely to have been restrained due to the Northern Hemisphere having gradually cooled, and therefore the meridional thermal gradients decreased after the EOGM (Fig. 4.9).

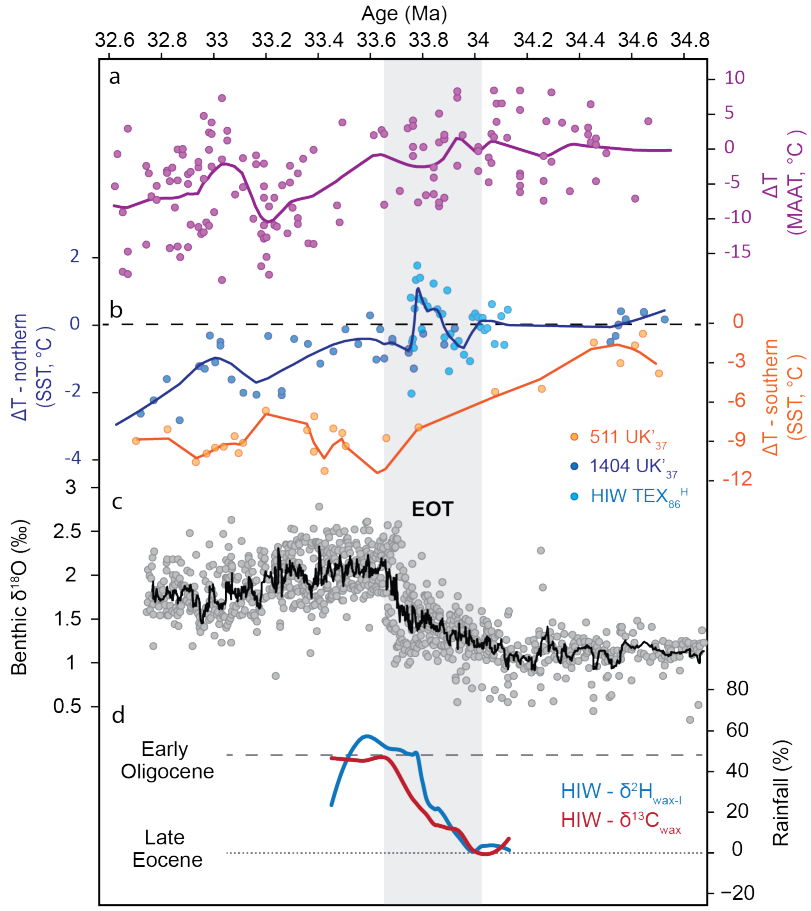

Figure 4.9. Comparison between leaf wax $\delta^2H_{wax\text{-}I}$, and $\delta^{13}C_{wax}$-based rainfall variations and temperature records in both hemispheres. A, continental records of mean annual average temperature (MAAT) (Zanazzi et al., 2007; Hren et al., 2013; Fan et al., 2017). B, sea surface temperatures from sites 511 (blue, North Atlantic) and 1404 (orange, South Atlantic) (Plancq et al., 2014; Liu et al., 2018) and new TEX_{86} at HIW. Temperature changes (ΔT) are relative to the mean values between 34.5 and 37 Ma at individual localities. The published datasets reviewed in A and B (points) are smoothed by using local regression (curves). C, global benthic $\delta^{18}O$ records (points), with the black line representing the 10-point moving average (Cramer et al., 2009). D, reconstructed changes in rainfall based on $\delta^{13}C$ and $\delta^2H_{wax\text{-}I}$; dashed line represents the average MAP for the early Oligocene (33.45-33.70 Ma); dotted line denotes the average MAP for the late Eocene (before 34.0 Ma). Change of MAP in proportion (MAP%) is calculated relative to the mean values for the late Eocene (before 34.0 Ma) and is reported in percent (%). The shaded bar denotes the EOT interval.

4.5. Conclusions

Our biomarker proxy data implies that an increase in precipitation in the subtropical Gulf Coast regions across the EOT can be associated with a northward shift in the position of the ITCZ that was driven by a larger polar-to-tropic temperature gradient in the Southern Hemisphere. Paleoclimate reconstruction supports that the change in Atlantic Ocean circulation, along with an invigoration of modern-like AMOC, occurs during the late Eocene. Our findings highlight the critical role of high-latitude climate and large-scale ocean circulation in modulating tropical and subtropical hydroclimate and its potential impacts on CO_2-weathering feedback during the "greenhouse" to "icehouse" transition near the E/O boundary.

Chapter 5. Isotopic Fingerprints of Mountain Uplift and Global Cooling in Paleoclimatic and Paleoecological Records from the Northern Tibetan Plateau

5.1. Introduction

Tectonism and global change are two key factors influencing the Cenozoic climate in Asia (Kutzbach et al., 1989; Molnar et al., 1993; An et al., 2001; Dettman et al., 2001; Dettman et al., 2003). The high topography of the Himalaya-Tibetan Plateau orogen was constructed as a result of the India-Asia collision since 50-55 Ma (Tapponnier et al., 2001; Molnar and Stock, 2009; Najman et al., 2010), which in turn changed the regional and global atmospheric circulation patterns (Ruddiman and Kutzbach, 1989; An et al., 2001; Boos and Kuang, 2010; Molnar et al., 2010; An, 2014). High Himalaya-Tibetan Plateau is a primary driver in the development of the Asian monsoons (An et al., 2001) and the aridification history of Central Asia (Zhuang et al., 2011; Miao et al., 2012; Li et al., 2016; Wang et al., 2020). On the other hand, global change has impacted the Asia climate throughout the Cenozoic. For example, Tibetan Plateau has become increasingly arid due to global cooling at the Eocene-Oligocene transition (Dupont-Nivet et al., 2007) and the Middle Miocene Climate Maximum (Miao et al., 2011; Tang et al., 2011; Zhuang et al., 2011).

Differentiating the relative role of tectonism versus global climate change remains challenging. We are particularly interested in the middle Miocene, a period of active tectonism when the global climate change also manifests the influential impact in the regional climatic records. Sedimentary and geochemistry evidence suggest that the northern Tibetan Plateau has uplifted during the late Miocene (Bovet et al., 2009; Zhuang et al., 2014; Zuza et al., 2016; Zhuang et al., 2019b). The high topography of the Tibetan Plateau has acted as a moisture barrier of the Westerlies, enhancing the regional aridity in Central Asia (Miao et al., 2012; Wang et al., 2020). However, the dry climate has also been affected by global climate change. Post-Middle Miocene global cooling, one of the most profound climate changes during the Cenozoic, has drawn particular attention in the studies of Central Asian climate because of contemporary uplift of the northern Tibetan Plateau (Bovet et al., 2009; Zhuang et al., 2014; Zuza et al., 2016; Zhuang et al., 2019a). Global cooling can reduce the capacity of moisture load in the atmosphere, limiting the precipitation in Central Asia (Dupont et al., 2007; Miao et al., 2011). In the northern Tibetan Plateau, increasing xerophytic pollen proportion and carbonate $\delta^{18}O$ values in sedimentary records indicate that Qaidam Basin has encountered extensive aridity since ca. 18 Ma (Zhuang et al., 2011; Miao et al.,

2012).

How tectonic activity and global climate change shaped the regional ecological community has also added complexity to the tectonism-global climate dilemma. In the northern Tibetan Plateau, temperature and hydrological changes invoked by contemporary tectonic uplift have changed C_3 and C_4 plants' contribution since the mid-late Miocene. For example, leaf wax carbon isotopic data from the North Pacific suggest that a decline in C_4 plant proportion between ~12-8 Ma is associated with cold/arid climate due to the rapid growth of source area northern Tibetan Plateau, as well as the global cooling (Jia et al., 2012). C_4 plant has been recognized to expand during the late Miocene-early Pliocene at a global scale (Cerling et al., 1997; Tipple and Pagani, 2007; Edwards et al., 2010; Strömberg, 2011). C_4 plants preferentially adapt to low latitudes with warm temperature (>25°C) and sufficient precipitation (>25 mm per month), whereas C_3 plants have a competitive advantage to inhabit high latitudes and elevations (Collatz et al., 1998; Edwards and Smith, 2010). The declining atmospheric pCO_2 and warm-dry climate favor C_4 grasses relative to C_3 woody plants in tropic and subtropic regions since the middle-late Miocene (Pagani et al., 1999; Huang et al., 2007; Edwards et al., 2010).

In this study, we reconstruct paleoecology and paleoclimate in the Hexi Corridor (foreland basin), then compare with records in the Qaidam Basin (intermontane basin). Three questions are addressed. (1) we establish the basin-wide paleoecology and paleoclimate records in the Hexi Corridor to understand the linkage between climate and ecology. (2) we differentiate the basin isolation signal related to the tectonic uplift by comparing the Hexi Corridor and Qaidan Basin' records. (3) the intra- and inter-basinal comparisons advance our understanding of the relative role of tectonism and global cooling on regional climatic and ecological evolutions.

5.2. Geological Background and Modern Climate

Hexi Corridor (Fig. 5.1A), an elongate foreland basin in the northern margin of Tibetan Plateau, is constrained by the North Qilian Shan Fault to the south, Altyn Tagh Fault to the west, Alax Block to the North, and Ordus Block to the east. The basin is divided into three sub-basins: Jiuxi, Jiudong, and Zhangye Basins (Dai et al., 2005; Fang, 2005). Our study sites are in the Jiuxi Basin (Fig. 5.1B) bounded by the North Qilian Shan Fault to the south, Altyn Tagh Fault to the west, Heishan Fault to the north, and Jiayuguan Fault to the east.

Cenozoic sedimentation in the Hexi Corridor mainly consist of five

formations: the late Eocene Huoshaogou Formation (ca. 40.2-33.35 Ma), the late Oligocene to early Miocene Baiyanghe Formation, the middle Miocene to Pliocene Shulehe Formation (ca. 13-5 Ma), the Pliocene-Pleistocene Yumen conglomerate (ca. 5-0.9 Ma), and the late Pleistocene Jiuquan conglomerate (ca. 0.9-0.1 Ma) ((GBGMR), 1989; Zhao et al., 2001; Dai et al., 2005). We study post-middle Miocene successions in the Laojunmiao (LJM), Wenshushan (WSS), and Caogou (CG) stratigraphic sections in the Jiuxi Basin, western Hexi Corridor (Fig. 5.2). The ages of each stratigraphic section are constrained by lithostratigraphy, biostratigraphy, and magnetostratigraphy (Zhao et al., 2001; Fang, 2005; Wang et al., 2016).

The LJM section (Fig. 5.2) extends from the late Miocene (ca. 13Ma) to the late Pleistocene (ca. 0.1 Ma) (Fang, 2005). The LJM section is subdivided into three formations. The lower part of Shulehe Formation (0-600 m) is composed of sandy siltstone and mudstone, associated with the deep lacustrine depositional environment. the upper part of Shulehe Formation (600-1200 m) is dominated by sandy conglomerate interbedded with muddy sandstone, which is deposited in shallow lacustrine to fan delta environment. Yumen Conglomerate and Jiuquan Conglomerate (1200-2000 m) consist of poorly sorted gravels, associated with an alluvial fan environment.

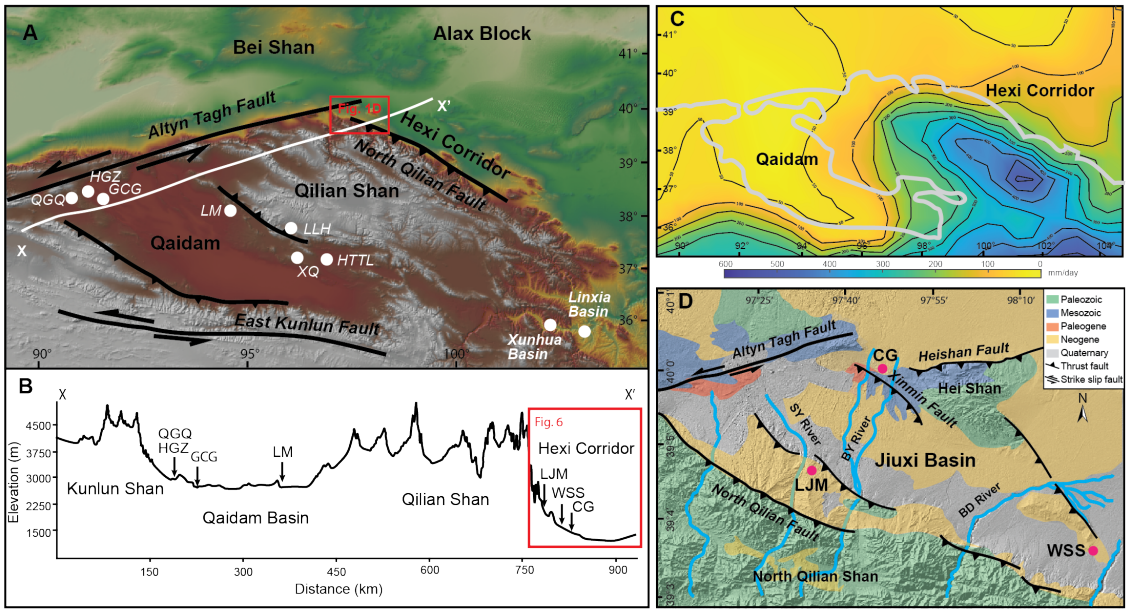

Figure 5.1. A, Topography of northern Tibetan Plateau, showing major faults, locations of paleoclimate studies from stable isotopes of fluvial and lacustrine carbonates, and leaf wax lipids. HGZ: Honggouzi (Wu et al., 2019); HTTL: Huaitoutala (Zhuang et al., 2011); Linxia Basin and Xunhua Basin (Hough et al., 2011); Qigequan (QGQ), Ganchaigou (GCG), Lake Mahai (LM), Lulehe (LLH), and Xiao Qaidam (XQ) are from (Kent-Corson et al., 2009). B, Elevation profile of Qaidam Basin, Qilian Shan, and Hexi Corridor, with nearby paleoclimate study sites. C, precipitation in northern Tibetan Plateau, with grey line denoting 3000 m contour. D, Geological map of Jiuxi Basin (modified from GBGMR, 1989 and Wang et al., 2016), showing major faults, strata, and studied sedimentary sections: Caogou (CG), Laojunmiao (LJM), and Wenshushan (WSS).

The WSS section (Fig. 5.2) spans from the late Miocene (ca. 11.5 Ma) to the late Pleistocene (> 0.9 Ma) (Zhao et al., 2001). The WSS section is subdivided into three formations. The lower Shulehe Formation (0-260 m) consists of siltstone and medium to coarse sandstone, channel lag deposits above the

erosional surface. The upper Shulehe Formation (260-750 m) has increasing proportions of medium-coarse sandstone and sandy conglomerate, deposited in the meandering fluvial environment. Yumen Conglomerate and Jiuquan Conglomerate (750-1150 m) are composed of pebble conglomerate interbedded with coarse sandstone, which is interpreted as the braided fluvial deposits.

The CG section (Fig. 5.2) spans from the late Oligocene (ca. 24.2 Ma) to the late Pliocene (2.8 Ma) (Wang et al., 2016) and is subdivided into five depositional units. The lower Baiyanghe Formation (0-170 m) is composed of fine to coarse sandstone with pebble conglomerate on the erosional surface. This unit is characterized by upward-fining trends, channel lag deposits, and cross-stratification, which is associated with a braided fluvial environment. The upper Baiyanghe Formation (170-280 m) comprises mudstone and interbedded fine sandstone and siltstones, reflecting a shallow lacustrine environment. The lower Shulehe Formation (280-530 m) is dominated by fine sandstone and siltstone, reflecting the delta fan environment. Upper Shulehe Formation (530-800 m) consists of pebble to cobble conglomerate with minor sandstone and siltstone layers. The upward coarsening and coarse-grained size are interpreted to be deposited in the distal to middle alluvial fan environment. Overlying Yumen Conglomerate (800-1050 m) is primarily composed of pebble- to cobble-

conglomerate, reflecting a proximal alluvial fan environment.

The northern Tibetan Plateau is mainly interacted by two moisture sources: Westerlies and Asian summer monsoon. Hexi Corridor on the northern margin of Tibetan Plateau predominately receives Atlantic moisture from the Westerlies and regionally recycled surface water (Araguás-Araguás et al., 1998; Li and Garzione, 2017). The summer monsoons (East Asian summer and South Asian summer monsoon) could only influence the southeastern margin of the Plateau (Araguás-Araguás et al., 1998; Tian et al., 2001). The modern Hexi Corridor receives the Westerlies moisture all year round with a substantial amount of recycled surface water from inner Asia (Bershaw et al., 2012; Li and Garzione, 2017). The meteorological data from International Atomic Energy Agency (IAEA) station in Zhangye show that the average annual precipitation falls in ~100-150 mm, with ~95% of precipitation occurring during summer; average temperature ranges from -10°C to 25°C, with the average annual temperature at 8°C (IAEA/WMO, 2006).

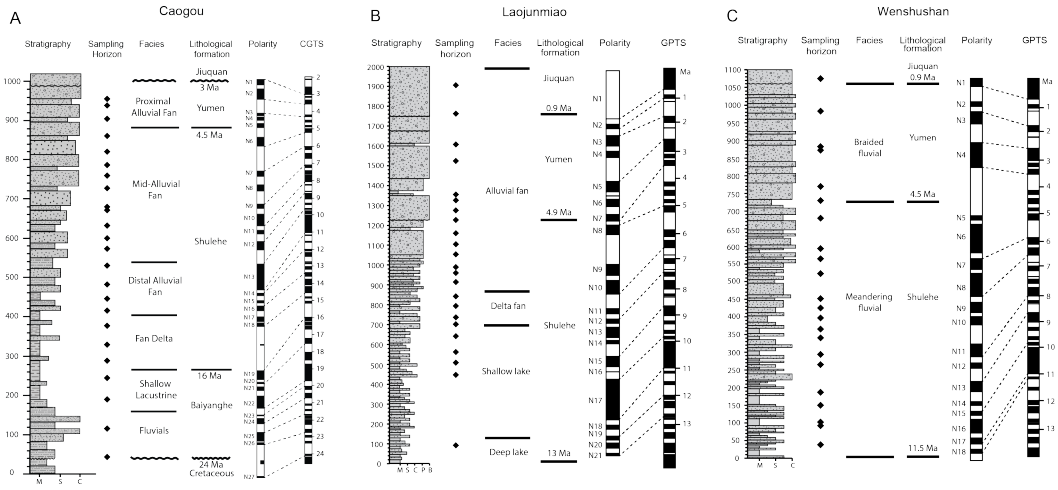

Figure 5.2. Stratigraphic column of A, Caogou (CG), B, Laojunmiao (LJM), and C, Wenshushan (WSS) sections with the interpretation of depositional facies and lithological Formations. Age constraints of CG section are interpreted by Wang et al. (2016), LJM section is interpreted by Fang (2005), and WSS are interpreted by Zhao et al. (2001). M: mudstone; S: sandstone; C: conglomerate; P: pebble; B: boulder.

5.3. Methods and Materials

We studied leaf wax $\delta^{13}C_{wax}$ values of mudstone and siltstone from three stratigraphic sections in Jiuxi Basin, including 23 samples from the LJM section, 21 samples from the WSS section, and 15 samples from the CG section. $\delta^{13}C_{wax}$ values of terrestrial-high plants are a function of $\delta^{13}C$ of atmospheric CO_2 ($\delta^{13}C_{atm}$) and photosynthetic fractionation during carbon fixation (Farquhar et al., 1982; Farquhar et al., 1989a; Sparks and Ehleringer, 1997). Fractionation between $\delta^{13}C_{atm}$ and $\delta^{13}C_{wax}$, expressed by carbon isotope discrimination (ε_{CO_2-wax}), is modulated by the physiological (photosynthetic path-

ways) and environmental factors (e.g., water stress) (Farquhar et al., 1982; Sparks and Ehleringer, 1997; Diefendorf and Freimuth, 2017). ε_{CO_2-wax} is calculated with given $\delta^{13}C_{atm}$ values:

$$\varepsilon_{CO2\text{-}wax} = (\frac{\delta^{13}C_{atm} + 1}{\delta^{13}C_{wax} + 1} - 1) \times 10^3 \quad (5.1)$$

We also analyzed oxygen isotopic composition ($\delta^{18}O$) of bulk sediments from LJM, WSS, and CG sections, which reflect changes in paleoclimate conditions, such as precipitation, evaporation, and temperature.

5.3.1. Total Lipid Extraction

Rock samples were broken and grounded with pestle and mortar into the coarse-sand size and freeze-dried for 48 hours before extraction. Total lipids were extracted with Soxhlet extractor using the azeotrope of dichloromethane/methanol (DCM/MeOH; 2:1 v/v) for 48 hours. The lipid extracts were evaporated under a stream of pure nitrogen until dry. Organic compounds in total lipid extracts were separated into apolar, intermediate, and polar fractions using a pipette column filled with ca. 0.5 grams of activated silica gel and eluted with 2 ml hexane, 4 ml DCM and 4 ml methanol sequentially.

5.3.2. Column Chromatography and *n*-Alkanes Characterization

n-Alkanes contained in the apolar fractions are re-dissolved into 1500 µL of hexane. *n*-Alkane abundances were determined using a Thermal Trace 1310 Gas chromatography (GC)-flame ionization detector (FID) fitted with programmable-temperature vaporization (PTV) injector and TG-1MS column (60 m long, 0.25 mm i.d., 0.25 µm film thickness). Samples were carried by helium at a rate of 2 ml/min. GC oven temperature is ramped from 60 °C (holding for 1 min) to 320 °C at a rate of 15 °C/min (holding for 20 min). Individual n-alkanes were identified by comparing the elution time with a reference standard (Mix A6, Schimmelmann, Indiana University Bloomington).

The carbon preference index (CPI) of *n*-alkanes were determined using the equation:

$$\mathrm{CPI} = \frac{1}{2}\frac{\sum \mathrm{A}(23+25+27+29+31+33)+\sum \mathrm{A}(25+27+29+31+33+35)}{\sum \mathrm{A}(24+26+28+30+32+34)} \quad (5.2)$$

Where A stands for the areas of the individual *n*-alkanes that are estimated by using Xcalibur for chromatography analysis. Numbers (23–35) represent the chain length of *n*-alkanes.

5.3.3. Leaf Wax Carbon Isotopic Analysis

Leaf wax carbon isotopic values were measured using Trace 1310 GC coupled to a Thermo Delta V Advantage isotope ratio mass spectrometer (IRMS) with a Thermo Isolink interface. Trace 1310 GC is fitted with PTV injector and TG-5MS column (30 m long, 0.25 mm i.d., 0.25 µm film thickness). Samples were carried by helium at a rate of 2 ml/min. Compounds were separated by the GC with the temperature ramping from 60 °C (held for 2 min) to 170 °C at 14 °C/min, to 300 °C at 3 °C/min, to 320 °C at 14 °C/min, then isothermally holding at 320 °C for 5 mins. Samples were analyzed in duplicate with a mean analytical precision of 0.1 ‰ for $\delta^{13}C$. The *n*-alkane reference materials Mix A6 (*n*-C_{16} to *n*-C_{30}; Arndt Schimmelmann, Indiana University) were measured every four to six analyses for monitoring the instrumental drift. Carbon isotope ratio values were calibrated relative to Mix A6. $\delta^{13}C$ values are reported relative to Vienna Pee Dee Belemnite (VPDB) using the equation:

$$\delta^{13}C = \left(\frac{R_{sample}}{R_{reference}} - 1\right) \tag{5.3}$$

Where R represents the $^{13}C/^{12}C$ ratios in samples and standard reference materials.

5.3.4. Calculation of C_4 Plant Contribution

Plants using C_3 (Calvin-Benson) carbon fixation pathways have larger carbon isotopic fractionation than those using the C_4 (Hatch-Slack) pathway (O'Leary, 1988; Tipple and Pagani, 2007; Diefendorf and Freimuth, 2017). The modern mean ε_{CO_2-wax} value of n-C_{31} is -26.5 ± 3 for C_3 plants, while is -13.7 ± 2 for C_4 plants (Tipple and Pagani, 2010; Jia et al., 2012). We model the change of n-alkanes contribution from C_4 plants in the Hexi corridor by assuming that the Miocene ε_{CO_2-wax} is the same as the modern values. The equation is expressed as follows:

$$\varepsilon_{CO_2-wax} = \varepsilon_{CO_2-C_3} \times (1 - f_{C_4}) + \varepsilon_{CO_2-C_4} \times f_{C_4} \tag{5.4}$$

Where $\varepsilon_{CO_2-C_3}$ and $\varepsilon_{CO_2-C_4}$ represent the carbon isotopic fractionation between $\delta^{13}C_{atm}$ and $\delta^{13}C_{wax}$ of n-alkanes derived from C_3 plants and C_4 plants, respectively. f_{C_4} is the fraction of C_4 plants' abundance. ε_{CO_2-wax} values are calculated with equation (5.1) with reconstructed CO_2 (Tipple et al., 2010)and observed leaf wax carbon isotopes (Fig. 5.3).

5.3.5. Oxygen Isotopic Analysis

0.5-1 mg of powdered bulk rock samples were analyzed for $\delta^{18}O$ values. Samples were grounded by an agate mortar and were dried in the oven at

70°C for 24 hours. Dried samples were reacted with orthophosphoric acid at 72°C to produce carbon dioxide and water. $\delta^{18}O$ values were measured using a Gas Bench interfaced with Thermo Delta V Advantage IRMS. Isotopic results are reported with respect to VPDB and expressed in ‰. The precision of repeated analysis for $\delta^{18}O$ values is less than 0.15‰.

5.4. Results

Samples from LJM, WSS, and CG sections are most abundant in long-chain *n*-alkane homologs (*n*-C_{27}, *n*-C_{29}, and *n*-C_{31}), indicating a terrestrial higher plant source (Eglinton and Hamilton, 1967; Tipple and Pagani, 2007). CPI values of all sections in the Hexi Corridor are higher than 1, suggesting that samples are unlikely influenced by post-depositional thermal alteration (Marzi et al., 1993). We report carbon isotopic compositions of *n*-C_{29} and *n*-C_{31} alkanes from LJM, WSS, and CG sections and discuss their weighted mean values ($\delta^{13}C_{wax}$) in the text (Fig. 5.3).

$\delta^{13}C_{wax}$ values of CG section (Fig. 5.3E) decrease from -28.0‰ to -30.5‰ between 15.6 Ma to 10.9 Ma, followed by an increase of isotopic values from -30.5‰ to -29.9‰ between 10.9 Ma to 5.0 Ma. After this positive shift, $\delta^{13}C_{wax}$ values range from -29.9‰ to -31.4‰ from 5 Ma to 2.8 Ma. $\delta^{13}C_{wax}$ values of LJM section (Fig. 5.3E) decrease from -30.5‰ to -33.4‰ between

12.7 Ma and 3.5 Ma, then isotopic values increase from 3.5 Ma to 2.6 Ma and vary between -30.5‰ and -32.9‰. $\delta^{13}C_{wax}$ values of WSS section (Fig. 5.3E) decrease from -30.1‰ to -32.2‰ between 11.4 Ma to 4.2 Ma, followed by a variation on isotopic values between -30.5‰ and -32.2‰ from 4.2 Ma to 1.7 Ma.

We divided the $\delta^{13}C_{wax}$ records in Hexi Corridor into three stages by comparing our records with regional and global paleoclimate records (Figs. 5.3 and 5.5). Stage one (16-12 Ma) shown in CG records is characterized by a decrease in $\delta^{13}C_{wax}$ values by ~2‰, consistent with the decreasing trends in $\delta^{13}C_{wax}$ records from the Qigequan (QGQ) and Honggouzi (HGZ) sections in the Qaidam Basin and from the North Pacific. This stage is concurrent with the positive shift of global benthic foraminifera $\delta^{18}O$ values (Fig. 5.5F) (Zachos et al., 2001) and declined $\delta^{13}C$ values of atmosphere CO_2 (Fig. 5.4E) (Tipple et al., 2010). In stage two (12-4 Ma), LJM and WSS show ~1.5-2‰ negative shift of $\delta^{13}C_{wax}$, while $\delta^{13}C_{wax}$ values in CG increase ~0.5‰. Stage three (after 4 Ma) shows variable $\delta^{13}C_{wax}$ values in the northern Tibetan Plateau.

$\delta^{18}O$ records of Hexi Corridor can be subdivided into three stages (Fig. 5.6). Stage one (16-12 Ma) is recorded in the CG section and show a decrease in $\delta^{18}O$ values from -5.4‰ to -11.0‰. In stage two (12-4 Ma), isotopic values

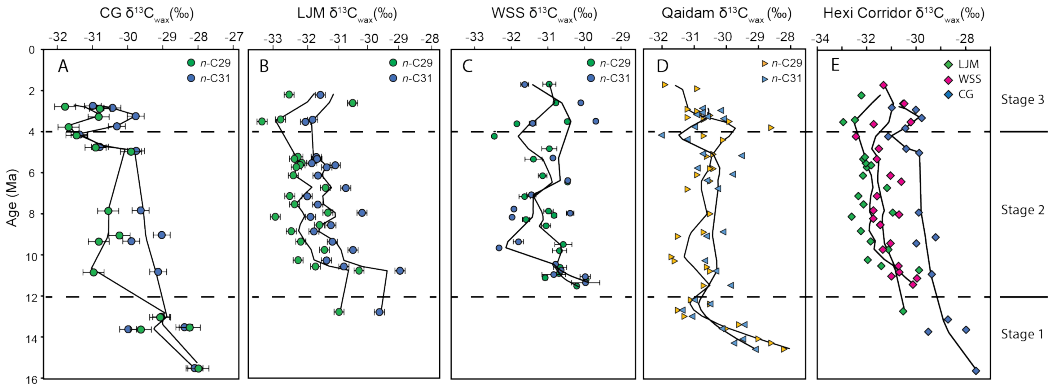

Figure 5.3. Leaf wax carbon isotopic ($\delta^{13}C_{wax}$) records of the A, Caogou (CG), B, Laojunmiao (LJM), and C, Wenshushan (WSS) sections from the Hexi Corridor, and D, Qigequan (QGQ) and Honggouzi (HGZ) sections from the Qaidam Basin (Wu et al., 2019). E, Weight mean $\delta^{13}C_{wax}$ of *n*-C_{29} and *n*-C_{31} alkanes in CG, LJM, and WSS sections.

are less variant, varying between -6.7‰ and -9.1‰ in CG, -10.5‰ ~ -8.7‰ in WSS, and -10.8‰ ~ -6.6‰ in LJM expect for one lowest value of -13.6‰ at 6.1 Ma. Stage three (after 4 Ma) shows a general increase of ca. 2‰ in $\delta^{18}O$ values.

5.5. Discussions

5.5.1. Decline in C_4 Plant in the Northern Tibetan Plateau since Middle Miocene Global Cooling

The most pronounced change in $\delta^{13}C_{wax}$ values occurs in stage one and is archived by CG records. ~2.5‰ negative shift of $\delta^{13}C_{wax}$ values from 16 Ma to 12 Ma reflect a change in carbon isotope discrimination and $\delta^{13}C_{atm}$ values (Fig. 5.3E). Reconstructed $\delta^{13}C_{atm}$ values decrease ~0.6‰ from 16 Ma to 12

Ma based on the reconstruction from benthic foraminifera records (Fig. 5.4E) (Tipple et al., 2010). Hence, a ~1.9‰ decrease of $\delta^{13}C_{wax}$ value reflects the change in carbon assimilation in response to a change in plant communities (e.g., C_3 vs. C_4 plants) and water stress. Several scenarios can explain the negative shift in CG $\delta^{13}C_{wax}$ values : (1) change in the proportion of C_3 and C_4 plants, (2) change in plant types among C_3 communities (e.g., angiosperms vs. gymnosperms), and (3) lessening of water stress conditions as a result of climate change.

Plants with different photosynthetic pathways (e.g., C_3 and C_4 pathways) produce distinct carbon isotopic signatures (Diefendorf and Freimuth, 2017). C_4 plants predominantly produce long-chain *n*-C_{31} and *n*-C_{33} alkanes, with a mean ε_{CO_2-wax} value of -26.5 ± 3 for C_3 plants and -13.7 ± 2 for C_4 plants (Tipple and Pagani, 2010; Jia et al., 2012). Late Holocene $\delta^{13}C_{wax}$ values (-32‰) from Lake Qinghai indicate a C_3 plant-dominated ecosystem (Thomas et al., 2014). $\delta^{13}C_{wax}$ values of CG section between 16-12 Ma (Fig. 5.3E) are higher than the Lake Qinghai $\delta^{13}C_{wax}$ values by ~4‰, indicating the presence of C_4 plant in the Hexi Corridor during the middle-late Miocene. Pollen records from the LJM section identify that herbaceous plant Artemisiaepollenites and Chenopodipollis are predominant between 13-11.15 Ma (Ma,

2005). C_4 Chenopodiaceae species that are abundant in saline and arid Central Asia desert and steppe regions (Pyankov et al., 2000; Lu et al., 2018) might also grow in the Hexi Corridor during the late Miocene. We calculated the contribution of C_4 plants using ε_{CO_2-wax} of *n*-C_{31} alkanes from Hexi Corridor records and from modern end members using equation (5.4) (Fig. 5.4). The reconstructed C_4 plant proportion from the CG section decrease by ~20% from 16 Ma to 12 Ma (Fig. 5.4A). The mean C_4 plant proportion in CG, LJM, and WSS sections vary between 0 and 15% after 12 Ma (Figs. 5.4A-C). C_4 plants have the advantage of adapting to warm growing season temperatures (Ehleringer et al., 1997). Declined global temperature after the middle Miocene Climate Optimum (Zachos et al., 2001) is likely to reduce C_4 plants.

$\delta^{13}C_{wax}$ record from the North Pacific sediments supports a decrease in C_4 plant from ~16% to 10% between 12 Ma and 8 Ma in the sediment source area (northern Tibetan Plateau) (Jia et al., 2012). The decline in the North Pacific record has been interpreted to indicate a cold and arid climate in the northern Tibetan Plateau due to the tectonic uplift and post-middle Miocene global cooling. The $\delta^{13}C_{wax}$ of *n*-C_{31} alkanes from the Qaidam Basin, despite a significant difference in elevation (>1000 m) compared to the Hexi Corridor, shows a contemporaneous negative shift by ~3‰ (Wu et al., 2019). Our calcu-

lation shows that this negative shift is equivalent to a ~19% decrease in the C_4 plant (Figs. 5.3D and 5.4D). Qaidam Basin has been uplifted for 2 km from 15 Ma to 10 Ma (Zhuang et al., 2014; Zhuang et al., 2019a), while Hexi Corridor is located at the geographical lowlands, i.e., the foreland basin. The reconstructions for the hinterland of intermontane Qaidam Basin and the foreland basin of Hexi Corridor both capture the decline of C_4 plants. Therefore, we argue it is global cooling rather than tectonism that drove this change in paleoecology.

Carbon isotope discrimination varies among taxonomic groups due to different water use efficiency and growth strategies (Brooks et al., 1997; Diefendorf and Freimuth, 2017). A change in $\delta^{13}C_{wax}$ values may be a signal of the ecological shift within the C_3 plants. For example, ε_{CO_2-wax} of conifers are > 2‰ lower than angiosperms with control of environment influences (Diefendorf et al., 2010; Diefendorf et al., 2011), and ε_{CO_2-wax} of gymnosperm can be more variable among species than at the family level (Sheldon et al., 2020). If the conifers contribution decreases between 16-12 Ma in the Hexi Corridor, we would expect to observe a negative shift in $\delta^{13}C_{wax}$ values. However, this scenario is not supported by the palynology study. Pollen data from the nearby LJM section do not show a resolvable change in angiosperms or gymnosperm proportion during 13-11 Ma (Ma, 2005). We argue that change in

photosynthetic fractionation among C_3 plant communities is unlikely the cause for $\delta^{13}C_{wax}$ change in CG from 16Ma to 12 Ma.

Plant carbon isotopic fractionation is strongly influenced by precipitation amount (PPT). The PPT mediates the leaf gas-exchange by controlling stomatal conductance (Farquhar et al., 1989a; Farquhar et al., 1989b; Marshall et al., 2007). A compilation of the global plant dataset shows increased ε_{CO_2-wax} values with mean annual precipitation amount (Diefendorf et al., 2010). $\delta^{13}C_{wax}$ values would decrease with increasing precipitation amount due to reduced water stress, and vice versa. Paleoclimatic data from the northern Tibetan Plateau support a generally arid climate during the middle to late Miocene (Miao et al., 2011; Miao et al., 2012). Pollen record from Qaidam Basin shows an increase in xerophytic plants since ca. 18 Ma, indicating a cooling and drying climate trend (Miao et al., 2011). Hence, decreased $\delta^{13}C_{wax}$ values from 16 Ma to 12 Ma cannot be attributed to the increased water availability in the Hexi Corridor.

5.5.2. Stable Hydroclimate in the Hexi Corridor during the Late Miocene

$\delta^{13}C_{wax}$ records in stage two (12-4 Ma) mainly archive the changes in atmospheric $\delta^{13}C$ values and paleoclimate in the Hexi Corridor. $\delta^{13}C_{wax}$ values of LJM and WSS sections (Fig. 5.5A) show ~1.5‰ negative shift from 12

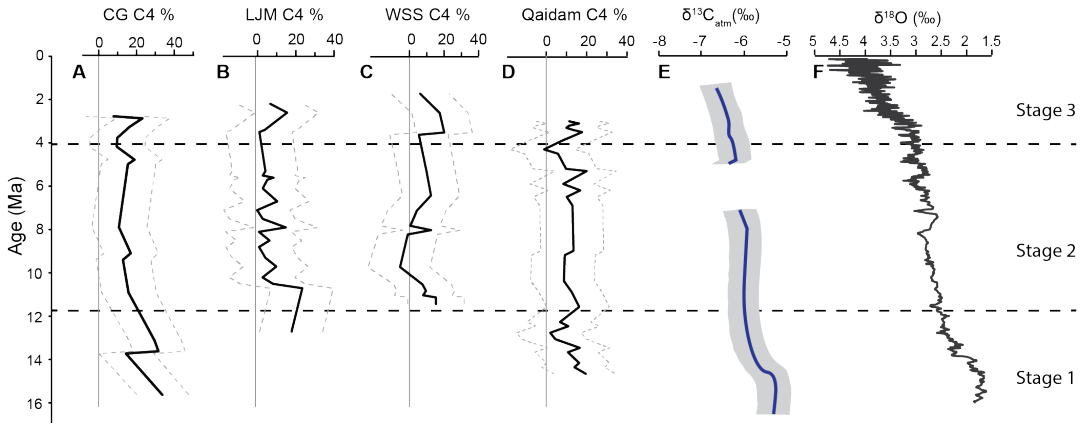

Figure 5.4. Calculated C_4 contribution from $\delta^{13}C_{wax}$ of C_{31} *n*-alkanes in the CG (A), LJM (B), and WSS (C) sections from the Hexi Corridor and QGQ and HGZ sections from the Qaidam Basin (D) (Wu et al., 2019). Dashed gray lines denote 1-sigma calculation uncertainty of modern end-members C_{31} *n*-alkanes. E, Reconstructed $\delta^{13}C$ of atmosphere CO_2 ($\delta^{13}C_{atm}$) from benthic foraminifera are shown in blue with a 90% confidence interval (Tipple et al., 2010). F, A compilation of global benthic foraminifera $\delta^{18}O$ records (Zachos et al., 2001).

Ma to 4 Ma, which is consistent with 1‰ decrease in $\delta^{13}C$ values of the atmospheric CO_2 ($\delta^{13}C_{atm}$) during the same period (Fig. 5.4E) (Tipple et al., 2010). Given that variation of Hexi Corridor $\delta^{13}C_{wax}$ values resemble the trend of $\delta^{13}C_{atm}$ values during the middle and late Miocene, the decrease in $\delta^{13}C_{wax}$ values reflects the change in $\delta^{13}C_{atm}$ values from 12 Ma to 4 Ma. We calculated ε_{CO_2-wax} of CG, LJM, and WSS sections by subtracting the effect on the $\delta^{13}C_{wax}$ values due to $\delta^{13}C_{atm}$ variation (Fig. 5.5B). The calculated ε_{CO_2-wax} values reflect hydrological change related to precipitation and evaporation, with the mean value of ~27‰ for LJM, ~26‰ for WSS, and ~25‰ for CG

sections. ε_{CO_2-wax} values of three sections in the Hexi Corridor vary within an amplitude of 1-2‰ between 12-4 Ma, suggesting a relatively stable hydrological condition. $\delta^{18}O$ results of LJM, WSS, and CG sections (Fig. 5.5C) are consistent with previous stable isotopic records from the Hexi Corridor (Kent-Corson et al., 2009) suggesting a relatively stable hydroclimate.

5.5.3. Uplift-driven Isolation of Qaidam Basin and Enhanced Aridity

Paleoclimate studies from the Qaidam Basin show that climate has become increasingly arid since the middle Miocene, which is concurrent with high elevation obtained in the northern Tibetan Plateau. Calculated ε_{CO_2-wax} values from QGQ and HGZ sections in the western Qaidam (Fig. 5.5D) decrease ~2‰ since ~12 Ma. Water stress has been recognized as a strong control on carbon discrimination of C_3 plants (Diefendorf and Freimuth, 2017). Water availability influences the plant's stomal conductance and CO_2 uptake during photosynthesis, which affects carbon isotope fractionation. Decreased ε_{CO_2-wax} from 12 Ma to 4 Ma is likely to reflect enhanced evaporation and water stress.

$\delta^{18}O$ records (Fig. 5.5E) of fluvial and lacustrine carbonates in the Qaidam Basin are consistent with ε_{CO_2-wax} record and support a generally arid climate after the middle to late Miocene (Kent-Corson et al., 2009; Hough et

al., 2011; Zhuang et al., 2011). The enhanced dry climate in the Qaidam Basin is distinguished from the stable hydroclimate condition in the adjacent Hexi Corridor during the same interval (Fig. 5.5). Additionally, mean $\delta^{18}O$ values in the Qaidam records (-8.6‰) (Kent-Corson et al., 2009) resemble those in the Hexi Corridor (-8.1‰), even though the elevation of the Qaidam Basin is more than 1000 m higher than that of the Hexi Corridor (Figs. 5.5C and 5.5E). $\delta^{18}O$ values are supposed to become more negative as increasing elevation since heavier oxygen isotope (^{18}O) become more depleted during rainfall (Garzione et al., 2000; Poage and Chamberlain, 2001; Rowley et al., 2001). Similar mean $\delta^{18}O$ values between the Qaidam Basin and Hexi Corridor imply that isotopic depletion in the Qaidam Basin due to higher elevation has compensated the isotopic enrichment caused by drier climate.

The discrepancy between regional climatic patterns between the Hexi Corridor and the Qaidam Basin is related to their tectonic settings. Increasing evidence suggests a major uplift and outward expansion of the northern Tibetan Plateau during the middle to late Miocene, based on structural, stable isotope, biomarker, and thermochronological studies. Provenance analysis of Miocene granitic clasts north of Altyn Tagh fault suggests a reduced slip rate and a transition of tectonic activation from lateral extrusion to the dis-

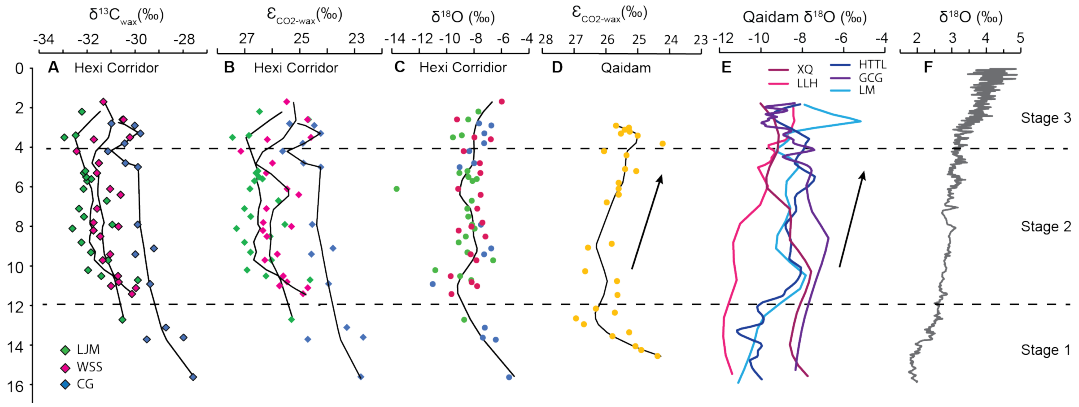

Figure 5.5. Comparison of paleoclimatic records in Northern Tibetan Plateau. A, Weight mean $\delta^{13}C_{wax}$ of C_29 and C_31 *n*-alkanes in CG, LJM, and WSS sections. B, CG, LJM, and WSS sections. C, $\delta^{18}O$ records of bulk rocks in the CG, LJM, and WSS sections. D, ε_{CO_2-wax} records of HGZ and QGQ in the Qaidam Basin (Wu et al., 2019). E, $\delta^{18}O$ records of fluvial and lacustrine carbonate rocks from Ganchaigou (GCG), Lake Mahai (LM), Lulehe (LLH), and Xiao Qaidam (XQ) (Kent-Corson et al., 2009) and Huaitoutala (HTTL) (Zhuang et al., 2011). Locations of the paleoclimate studies discussed in the text are shown in Fig. 5.1. F, A compilation of global benthic foraminifera $\delta^{18}O$ records (Zachos et al., 2001).

tributed crustal thickening since the end of early Miocene (Yue et al., 2004). Sedimentary records from Hexi Corridor suggest that high energy deposition and northeast-trending paleocurrent initiate since ca. 13 Ma, indicating crustal shortening in the North Qilian Shan before the late Miocene (Bovet et al., 2009). These findings are consistent with apatite fission-track studies showing rapid cooling in the North Qilian Shan during 20-10 Ma (George et al., 2001; Zheng et al., 2010). Nd isotopic record from Northern Pacific suggests increasing input of Asian dust sediment since 15 Ma, resulting from accelerated

exhumation on northern Tibetan Plateau induced by surface uplift (Li et al., 2011). Stable isotopic studies from Qaidam, Linxia, and Xunhua Basins suggest surface uplift of northeastern Tibetan Plateau between ca. 15-11 Ma (Hough et al., 2011; Zhuang et al., 2014). Recent detrital zircon U-Pb and paleothermometry data show that the northern Tibetan Plateau's high topography has gained by ca. 8 Ma (Chen et al., 2019; Zhuang et al., 2019a). We argue that Qaidam Basin has encountered more substantial evaporation and less precipitation than the Hexi Corridor did since the northern Tibetan Plateau uplifted at the middle to late Miocene. Uplift of basin-bounding ranges in the northern Tibetan Plateau (Altyn Shan and Qilian Shan) has intensified arid cliamte and hydrological isolation of the Qaidam Basin by blocking Westerlies moisture from the Atlantic and Arctic. Hence, tectonic forcing might have a more pivotal effect than global climate change on regional hydroclimate change in the Qaidam Basin during the late Miocene.

5.5.4. Intra-basinal Comparison of $\delta^{13}C_{wax}$ Records in the Hexi Corridor

$\delta^{13}C_{wax}$ and $\delta^{18}O$ records in the Hexi Corridor show the persistent intra-basinal offset since ca. 12 Ma (Figs. 5.5A, and 5.6), reflecting distinguished hydrological patterns within different parts of the basin. Even though all three sections resemble isotopic trends, the $\delta^{13}C_{wax}$ values of LJM are over-

all more negative than those of WSS by ~1‰ and are lower than those of CG by ~1.5‰ (Fig. 5.5A). The mean $\delta^{18}O$ values in the LJM (-8.7‰) is lower than in the WSS (-8.1‰) and CG (-7.5‰) (Fig. 5.6). Compared to the intra-basinal difference among different parts of the Hexi Corridor, we suggest that the offsets in mean isotopic values indicate specific local environmental features. We solicit two scenarios to explain the intra-basinal isotopic differences in the Hexi Corridor: the orographic effect and elevation effect.

The orographic rainfall effect demonstrates that more precipitation occurs in the mountain front and diminishes toward the basin's center. Our field observation along the transection reveals a transition in vegetation types from patches of forests at LJM near the Qilian Shan slope, shrubs at WSS to sparse grasses at CG in the center Hexi Corridor Basin (Fig. 5.6). $\delta^{13}C_{wax}$ and $\delta^{18}O$ isotopic values would become more depleted due to increased precipitation as approaching the North Qilian Shan front. LJM is closest to the North Qilian Shan comparing with the other two sections. Thus, it could receive more precipitation and the lowest mean $\delta^{13}C_{wax}$ and $\delta^{18}O$ values. Contrarily, CG is at the northern margin of the Jiuxi Basin, where less rainfall and enhancing evaporation and recycling of moistures lead to more positive oxygen isotopic values in local precipitation. Stresses precipitation will reflect plant wax isotopic

compositions.

$\delta^{18}O$ values decrease as increasing elevation, which demonstrates the altitude effect on isotopic fractionation. Altitude can affect leaf carbon isotopic fractionation with control of mean annual precipitation, which is characterized by reducing $\delta^{13}C$ values as increasing elevation (Warren et al., 2001; Van de Water et al., 2002; Marshall et al., 2007; Diefendorf et al., 2010). The LJM, WSS, and CG sections have altitudes of 2280m, 1720m, and 1570m, respectively (Fig. 5.1). The higher elevation of the LJM section could be a potential cause for lower $\delta^{13}C_{wax}$ and $\delta^{18}O$ values than those in the WSS and the CG.

5.5.5. Dynamic Climate in Northern Tibetan Plateau since the Pliocene

ε_{CO_2-wax} values of LJM, WSS, and CG (Fig. 5.5B) show positive shifts in stage three (after ~4 Ma), suggesting a drying climate in the Hexi Corridor, which is consistent with increased $\delta^{18}O$ values in the LJM (Kent-Corson et al., 2009). The intensified aridity is synchronous with global cooling indicated by increasing benthic foraminifera $\delta^{18}O$ values (Fig. 5.5F) (Zachos et al., 2001). We argue that drying climate after ca. 4 Ma in the Hexi Corridor is associated with reduced moisture hold by air masses due to cooling climate. Hexi Corridor $\delta^{18}O$ records (Fig. 5.6) support an arid climate trend since 4 Ma.

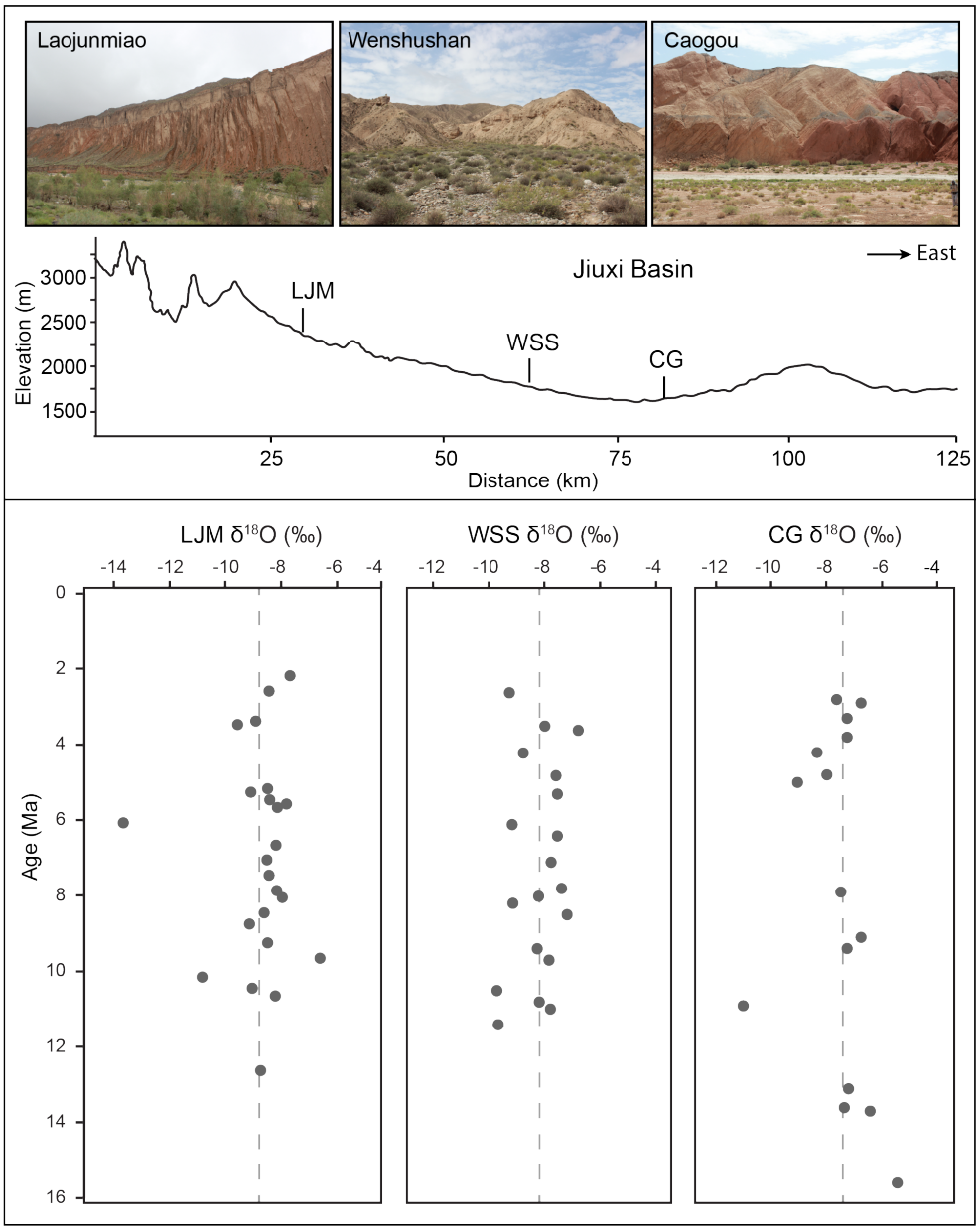

Figure 5.6. Field pictures show ecology along the elevation transection of the Jiuxi Basin, correlated with $\delta^{18}O$ records from CG, LJM, and WSS sections. Refer to Fig. 1 for the localities. $\delta^{18}O$ records of bulk rocks in the Caogou (CG), Laojunmiao (LJM), and Wenshushan (WSS) sections from the Hexi Corridor. Dashed gray lines denote the mean isotopic values of each sedimentary section.

5.6. Conclusions

We use leaf wax carbon isotopes and carbonate oxygen isotopes to reconstruct post-middle Miocene paleoecology and paleoclimate from sedimentary successions in the Hexi Corridor. Isotopic records show a declined abundance of C_4 plants between ca. 16-12 Ma due to the post middle Miocene global cooling. The stable carbon isotope discrimination (ε_{CO_2-wax}) and carbonate oxygen isotopes show disparate trends in the foreland basin of the Hexi Corridor and the intermontane Qaidam Basin from 12 to 4 Ma. We attribute the differences to the uplift induced basin isolation of the Qaidam Basin, a result of tectonism since the mid-late Miocene that is consistent with regional geological studies. Intra-basinal variations on isotopic values within the Hexi Corridor reflect local environmental features associated with orographic precipitation and elevation effect. A drier climate in the region after 4 Ma is associated with an enhanced cooling climate during Plio-Pleistocene.

Chapter 6. Conclusions

In this research, I conducted paleoclimate and paleoecology studies in Central Asia and the southern United States by applying compound-specific carbon and hydrogen isotopes, alkenone unsaturation-based paleothermometry ($U^{K'}_{37}$), and GDGT-based paleothermometry (TEX_{86}). My research project focus on three revolutionary climate events that caused significant changes in the Earth's climate and ecosystem: the last glacial-interglacial climate cycle, the Eocene-Oligocene climate transition, the post-middle Miocene climate change.

In the first project, we conclude that the climate boundary between the Westerlies and Asian summer monsoon is dynamically change depending upon the earth's orbital forcing. The relative strength of Westerlies and Asian summer monsoons not only varies interglacial-glacial scale but also respond to precessional forcing. Asian summer monsoons are penetrated inland ward when summer insolation is high, which results in increased rainfall in Central Asia. Climate is generally cold, dry during the last glacial maximum but wetter than at present when Asian summer monsoons retreat, and the Westerlies become dominant. Our findings suggest that the Westerlies and Asian summer monsoons alternately controlled the Qaidam Basin's climate in response to precessional forcing during the late Pleistocene.

In the second project, we found that (1) cooling in the Northern Hemisphere delay than in the Southern Hemisphere during the Eocene-Oligocene climate transition, and (2) precipitation is enhanced in the Gulf of Mexico regions due to asymmetric cooling between two hemispheres. The increased precipitation results from enhanced Atlantic Meridional Overturning Circulation that shifts the intertropical Convergence Zone northward over the Gulf Coast. We estimated an increase of up to 50% in mean annual precipitation during the Eocene-Oligocene climate transition. This finding marks the far-field connections between high- and low-latitudes and supports CO_2-weathering feedback in the oceanic-atmospheric systems during the "greenhouse" to "icehouse" transition.

In the third project, we address the relative importance of global climate change and tectonic activity in influencing the post-middle Miocene climate and ecology in the northern Tibetan Plateau. We compared the paleoclimate and paleoecology history in the Hexi Corridor and Qaidam Basin in the northern Tibetan Plateau. Our findings show that the Hexi Corridor has a stable hydrological condition since 12 Ma while the adjacent Qaidam Basin experienced increased aridity. We suggest that the Qaidam Basin influenced the uplift induced basin isolation since 12 Ma that prevents moisture transport to

the basin. Differently, Given that the Hexi Corridor is tectonically stable, its climate and ecology are primarily controlled by global climate change.

Bibliography

Abelson, M. and Erez, J. (2017). The onset of modern-like atlantic meridional overturning circulation at the eocene-oligocene transition: Evidence, causes, and possible implications for global cooling. *Geochemistry Geophysics Geosystems*, 18(6):2177–2199.

Aichner, B., Makhmudov, Z., Rajabov, I., Zhang, Q., Pausata, F. S. R., Werner, M., Heinecke, L., Kuessner, M. L., Feakins, S. J., Sachse, D., and Mischke, S. (2019). Hydroclimate in the pamirs was driven by changes in precipitation-evaporation seasonality since the last glacial period. *Geophysical Research Letters*, 46(23):13972–13983.

Allen, R. G., Pereira, L. S., Raes, D., and Smith, M. (1998). Crop evapotranspiration-guidelines for computing crop water requirements-fao irrigation and drainage paper 56. *Fao, Rome*, 300(9):D05109.

Alley, R. B. (2000). The younger dryas cold interval as viewed from central greenland. *Quaternary science reviews*, 19(1-5):213–226.

An, Z., Colman, S. M., Zhou, W., Li, X., Brown, E. T., Jull, A. J. T., Cai, Y., Huang, Y., Lu, X., Chang, H., Song, Y., Sun, Y., Xu, H., Liu, W., Jin, Z., Liu, X., Cheng, P., Liu, Y., Ai, L., Li, X., Liu, X., Yan, L., Shi, Z., Wang, X., Wu, F., Qiang, X., Dong, J., Lu, F., and Xu, X. (2012). Interplay between the westerlies and asian monsoon recorded in lake qinghai sediments since 32 ka. *Scientific Reports*, 2.

An, Z., Liu, T., Lu, Y., Porter, S., Kukla, G., Wu, X., and Hua, Y. (1990). The long-term paleomonsoon variation recorded by the loess-paleosol sequence in central china. *Quaternary International*, 7:91–95.

Araguás-Araguás, L., Froehlich, K., and Rozanski, K. (1998). Stable isotope composition of precipitation over southeast asia. *Journal of Geophysical Research: Atmospheres*, 103(D22):28721–28742.

Bartov, Y., Goldstein, S. L., Stein, M., and Enzel, Y. (2003). Catastrophic arid episodes in the eastern mediterranean linked with the north atlantic heinrich events. *Geology*, 31(5):439–442.

Berger, A. (1978). Long-term variations of caloric insolation resulting from the earth's orbital elements. *Quaternary research*, 9(2):139–167.

Bershaw, J., Penny, S. M., and Garzione, C. N. (2012). Stable isotopes of modern water across the himalaya and eastern tibetan plateau: Implications for estimates of paleoelevation and paleoclimate. *Journal of Geophysical Research-Atmospheres*, 117.

Bond, G., Showers, W., Cheseby, M., Lotti, R., Almasi, P., DeMenocal, P., Priore, P., Cullen, H., Hajdas, I., and Bonani, G. (1997). A pervasive millennial-scale cycle in north atlantic holocene and glacial climates. *science*, 278(5341):1257–1266.

Broccoli, A. J., Dahl, K. A., and Stouffer, R. J. (2006). Response of the itcz to northern hemisphere cooling. *Geophysical Research Letters*, 33(1):n/a–n/a.

Bush, R. T. and McInerney, F. A. (2013). Leaf wax n-alkane distributions in and across modern plants: Implications for paleoecology and chemotaxonomy. *Geochimica Et Cosmochimica Acta*, 117:161–179.

Caley, T., Roche, D. M., and Renssen, H. (2014). Orbital asian summer monsoon dynamics revealed using an isotope-enabled global climate model. *Nature communications*, 5:5371.

Caves, J. K., Winnick, M. J., Graham, S. A., Sjostrom, D. J., Mulch, A., and Chamberlain, C. P. (2015). Role of the westerlies in central asia climate over the cenozoic. *Earth and Planetary Science Letters*, 428:33–43.

Cerling, T. E. and Harris, J. M. (1999). Carbon isotope fractionation between diet and bioapatite in ungulate mammals and implications for ecological and paleoecological studies. *Oecologia*, 120(3):347–363.

Chen, F., Wu, D., Chen, J., Zhou, A., Yu, J., Shen, J., Wang, S., and Huang, X. (2016). Holocene moisture and east asian summer monsoon evolution in the northeastern tibetan plateau recorded by lake qinghai and its environs: A review of conflicting proxies. *Quaternary Science Reviews*, 154:111–129.

Chen, K. and Bowler, J. (1986). Late pleistocene evolution of salt lakes in the qaidam basin, qinghai province, china. *Palaeogeography, Palaeoclimatology, Palaeoecology*, 54(1-4):87–104.

Cheng, H., Spoetl, C., Breitenbach, S. F. M., Sinha, A., Wassenburg, J. A., Jochum, K. P., Scholz, D., Li, X., Yi, L., Peng, Y., Lv, Y., Zhang, P., Votintseva, A., Loginov, V., Ning, Y., Kathayat, G., and Edwards, R. L. (2016). Climate variations of central asia on orbital to millennial timescales. *Scientific Reports*, 6.

Cheng, H., Zhang, P. Z., Spötl, C., Edwards, R. L., Cai, Y. J., Zhang, D. Z., Sang, W. C., Tan, M., and An, Z. S. (2012). The climatic cyclicity in semiarid-arid central asia over the past 500,000 years. *Geophysical Research Letters*, 39(1).

Chiang, J. C. H. and Friedman, A. R. (2012). Extratropical cooling, interhemispheric thermal gradients, and tropical climate change. *Annual Review of Earth and Planetary Sciences*, 40(1):383–412.

Clark, P. U., Dyke, A. S., Shakun, J. D., Carlson, A. E., Clark, J., Wohlfarth, B., Mitrovica, J. X., Hostetler, S. W., and McCabe, A. M. (2009). The last glacial maximum. *Science*, 325(5941):710–714.

Coxall, H. K., Huck, C. E., Huber, M., Lear, C. H., Legarda-Lisarri, A., O'Regan, M., Sliwinska, K. K., van de Flierdt, T., de Boer, A. M., Zachos, J. C., and Backman, J. (2018). Export of nutrient rich northern component water preceded early oligocene antarctic glaciation. *Nature Geoscience*, 11(3):190–+.

Coxall, H. K., Wilson, P. A., Palike, H., Lear, C. H., and Backman, J. (2005). Rapid stepwise onset of antarctic glaciation and deeper calcite compensation in the pacific ocean. *Nature*, 433(7021):53–57.

Craig, H. and Gordon, L. I. (1965). Deuterium and oxygen 18 variations in the ocean and the marine atmosphere.

Cramer, B. S., Toggweiler, J. R., Wright, J. D., Katz, M. E., and Miller, K. G. (2009). Ocean overturning since the late cretaceous: Inferences from a new benthic foraminiferal isotope compilation. *Paleoceanography*, 24.

Dansgaard, W. (1964). Stable isotopes in precipitation. *Tellus*, 16(4):436–468.

DeConto, R. M., Pollard, D., Wilson, P. A., Palike, H., Lear, C. H., and Pagani, M. (2008). Thresholds for cenozoic bipolar glaciation. *Nature*, 455(7213):652–U52.

Diefendorf, A. F., Freeman, K. H., Wing, S. L., and Graham, H. V. (2011). Production of n-alkyl lipids in living plants and implications for the geologic past. *Geochimica Et Cosmochimica Acta*, 75(23):7472–7485.

Diefendorf, A. F. and Freimuth, E. J. (2017). Extracting the most from terrestrial plant-derived n-alkyl lipids and their carbon isotopes from the sedimentary record: A review. *Organic Geochemistry*, 103:1–21.

Diefendorf, A. F., Mueller, K. E., Wing, S. L., Koch, P. L., and Freeman, K. H. (2010). Global patterns in leaf 13c discrimination and implications for studies of past and future climate. *Proceedings of the National Academy of Sciences*, 107(13):5738–5743.

Dykoski, C., Edwards, R., Cheng, H., Yuan, D., Cai, Y., Zhang, M., Lin, Y., Qing, J., An, Z., and Revenaugh, J. (2005). A high-resolution, absolute-dated holocene and deglacial asian monsoon record from dongge cave, china. *Earth and Planetary Science Letters*, 233(1-2):71–86.

Eglinton, G. and Hamilton, R. J. (1967). Leaf epicuticular waxes. *Science*, 156(3780):1322–+.

Eglinton, T. I. and Eglinton, G. (2008). Molecular proxies for paleoclimatology. *Earth and Planetary Science Letters*, 275(1-2):1–16.

Ehleringer, J. R., Phillips, S. L., Schuster, W. S. F., and Sandquist, D. R. (1991). Differential utilization of summer rains by desert plants. *Oecologia*, 88(3):430–434.

Elling, F. J., Könneke, M., Lipp, J. S., Becker, K. W., Gagen, E. J., and Hinrichs, K.-U. (2014). Effects of growth phase on the membrane lipid composition of the thaumarchaeon nitrosopumilus maritimus and their implications for archaeal

lipid distributions in the marine environment. *Geochimica et Cosmochimica Acta*, 141:579–597.

Ellwood, B. B., Febo, L., Anderson, L., Hackworth, R. T., Means, G. H., Bryan, J. A., Tomkin, J., Rowe, H., and Jovane, L. (2019). Regional to global correlation of eocene–oligocene boundary transition successions using biostratigraphic, geophysical and geochemical methods. *Geological Magazine*, 157(1):80–100.

Elsworth, G., Galbraith, E., Halverson, G., and Yang, S. (2017). Enhanced weathering and co2 drawdown caused by latest eocene strengthening of the atlantic meridional overturning circulation. *Nature Geoscience*, 10(3):213–+.

Estep, M. F. and Hoering, T. C. (1980). Biogeochemistry of the stable hydrogen isotopes. *Geochimica et Cosmochimica Acta*, 44(8):1197–1206.

Fan, M., Ayyash, S. A., Tripati, A., Passey, B. H., and Griffith, E. M. (2017). Terrestrial cooling and changes in hydroclimate in the continental interior of the united states across the eocene-oligocene boundary. *GSA Bulletin*, 130(7-8):1073–1084.

Farquhar, G. D., Cernusak, L. A., and Barnes, B. (2007). Heavy water fractionation during transpiration. *Plant Physiology*, 143(1):11–18.

Farquhar, G. D., O'Leary, M. H., and Berry, J. A. (1982). On the relationship between carbon isotope discrimination and the intercellular carbon dioxide concentration in leaves. *Functional Plant Biology*, 9(2):121–137.

Ficken, K. J., Li, B., Swain, D., and Eglinton, G. (2000). An n-alkane proxy for the sedimentary input of submerged/floating freshwater aquatic macrophytes. *Organic geochemistry*, 31(7):745–749.

Flanagan, L. and Ehleringer, J. (1991). Stable isotope composition of stem and leaf water: applications to the study of plant water use. *Functional Ecology*, 5(2):270–277.

Freeman, K. and Colarusso, L. (2001). Molecular and isotopic records of c 4

grassland expansion in the late miocene. *Geochimica et Cosmochimica Acta*, 65(9):1439–1454.

Goldner, A., Herold, N., and Huber, M. (2014). Antarctic glaciation caused ocean circulation changes at the eocene-oligocene transition. *Nature*, 511(7511):574–+.

Goudie, A. S. (2007). Mega-yardangs: A global analysis. *Geography Compass*, 1(1):65–81.

He, Y., Liu, W., Zhao, C., Wang, Z., Wang, H., Liu, Y., Qin, X., Hu, Q., An, Z., and Liu, Z. (2013). Solar influenced late holocene temperature changes on the northern tibetan plateau. *Chinese Science Bulletin*, 58(9):1053–1059.

Heermance, R. V., Pullen, A., Kapp, P., Garzione, C. N., Bogue, S., Ding, L., and Song, P. (2013). Climatic and tectonic controls on sedimentation and erosion during the pliocene–quaternary in the qaidam basin (china). *Geological Society of America Bulletin*, 125(5-6):833–856.

Hemming, S. R. (2004). Heinrich events: Massive late pleistocene detritus layers of the north atlantic and their global climate imprint. *Reviews of Geophysics*, 42(1).

Henry, L. G., McManus, J. F., Curry, W. B., Roberts, N. L., Piotrowski, A. M., and Keigwin, L. D. (2016). North atlantic ocean circulation and abrupt climate change during the last glaciation. *Science*, 353(6298):470.

Herzschuh, U., Kürschner, H., and Mischke, S. (2006). Temperature variability and vertical vegetation belt shifts during the last 50,000 yr in the qilian mountains (ne margin of the tibetan plateau, china). *Quaternary Research*, 66(1):133–146.

Hopmans, E. C., Weijers, J. W. H., Schefuss, E., Herfort, L., Damste, J. S. S., and Schouten, S. (2004). A novel proxy for terrestrial organic matter in sediments based on branched and isoprenoid tetraether lipids. *Earth and Planetary Science Letters*, 224(1-2):107–116.

Hou, J., D'Andrea, W. J., and Liu, Z. (2012). The influence of 14c reservoir age on interpretation of paleolimnological records from the tibetan plateau. *Quaternary Science Reviews*, 48:67–79.

Hou, J., D'Andrea, W. J., MacDonald, D., and Huang, Y. (2007). Hydrogen isotopic variability in leaf waxes among terrestrial and aquatic plants around blood pond, massachusetts (usa). *Organic Geochemistry*, 38(6):977–984.

Hou, J., D'Andrea, W. J., Wang, M., He, Y., and Liang, J. (2017). Influence of the indian monsoon and the subtropical jet on climate change on the tibetan plateau since the late pleistocene. *Quaternary Science Reviews*, 163:84–94.

Hou, J., D'Andrea, W. J., and Huang, Y. (2008). Can sedimentary leaf waxes record d/h ratios of continental precipitation? field, model, and experimental assessments. *Geochimica et Cosmochimica Acta*, 72(14):3503–3517.

Hou, J., Huang, Y., Zhao, J., Liu, Z., Colman, S., and An, Z. (2016). Large holocene summer temperature oscillations and impact on the peopling of the northeastern tibetan plateau. *Geophysical Research Letters*, 43(3):1323–1330.

Houben, A. J. P., Quaijtaal, W., Wade, B. S., Schouten, S., and Brinkhuis, H. (2019). Quantitative organic-walled dinoflagellate cyst stratigraphy across the eocene-oligocene transition in the gulf of mexico: A record of climate- and sea level change during the onset of antarctic glaciation. *Newsletters on Stratigraphy*, 52(2):131–154.

Hovan, S., Rea, D. K., and Pisias, N. G. (1991). Late pleistocene continental climate and oceanic variability recorded in northwest pacific sediments. *Paleoceanography and Paleoclimatology*, 6(3):349–370.

Hren, M. T., Sheldon, N. D., Grimes, S. T., Collinson, M. E., Hooker, J. J., Bugler, M., and Lohmann, K. C. (2013). Terrestrial cooling in northern europe during the eocene-oligocene transition. *Proceedings of the National Academy of Sciences of the United States of America*, 110(19):7562–7567.

Huguet, C., Kim, J.-H., de Lange, G. J., Sinninghe Damsté, J. S., and Schouten, S. (2009). Effects of long term oxic degradation on the , tex86 and bit organic

proxies. *Organic Geochemistry*, 40(12):1188–1194.

Hyeong, K., Kuroda, J., Seo, I., and Wilson, P. A. (2016). Response of the pacific inter-tropical convergence zone to global cooling and initiation of antarctic glaciation across the eocene oligocene transition. *Scientific Reports*, 6.

IAEA/WMO (2006). Global network of isotopes in precipitation: The gnip database. accessible at: http://isohis.iaea.org.

Inglis, G. N., Farnsworth, A., Lunt, D., Foster, G. L., Hollis, C. J., Pagani, M., Jardine, P. E., Pearson, P. N., Markwick, P., Galsworthy, A. M. J., Raynham, L., Taylor, K. W. R., and Pancost, R. D. (2015). Descent toward the icehouse: Eocene sea surface cooling inferred from gdgt distributions. *Paleoceanography*, 30(7):1000–1020.

Joe Lambert, W. and Aharon, P. (2010). Oxygen and hydrogen isotopes of rainfall and dripwater at desoto caverns (alabama, usa): Key to understanding past variability of moisture transport from the gulf of mexico. *Geochimica et Cosmochimica Acta*, 74(3):846–861.

Kageyama, M., Paul, A., Roche, D. M., and Van Meerbeeck, C. J. (2010). Modelling glacial climatic millennial-scale variability related to changes in the atlantic meridional overturning circulation: a review. *Quaternary Science Reviews*, 29(21-22):2931–2956.

Kahmen, A., Simonin, K., Tu, K. P., Merchant, A., Callister, A., Siegwolf, R., Dawson, T. E., and Arndt, S. K. (2008). Effects of environmental parameters, leaf physiological properties and leaf water relations on leaf water delta o-18 enrichment in different eucalyptus species. *Plant Cell and Environment*, 31(6):738–751.

Kapp, P., Pelletier, J. D., Rohrmann, A., Heermance, R., Russell, J., and Ding, L. (2011). Wind erosion in the qaidam basin, central asia: implications for tectonics, paleoclimate, and the source of the loess plateau. *GsA Today*, 21(4/5):4–10.

Katz, M. E., Miller, K. G., Wright, J. D., Wade, B. S., Browning, J. V., Cramer,

B. S., and Rosenthal, Y. (2008). Stepwise transition from the eocene greenhouse to the oligocene icehouse. *Nature Geoscience*, 1(5):329–334.

Katz, R. W., Parlange, M. B., and Tebaldi, C. (2003). *Stochastic modeling of the effects of large-scale circulation on daily weather in the southeastern US*, pages 189–216. Springer.

Kim, J.-H., Huguet, C., Zonneveld, K. A. F., Versteegh, G. J. M., Roeder, W., Sinninghe Damsté, J. S., and Schouten, S. (2009). An experimental field study to test the stability of lipids used for the tex86 and palaeothermometers. *Geochimica et Cosmochimica Acta*, 73(10):2888–2898.

Kim, J.-H., van der Meer, J., Schouten, S., Helmke, P., Willmott, V., Sangiorgi, F., Koc, N., Hopmans, E. C., and Damste, J. S. S. (2010). New indices and calibrations derived from the distribution of crenarchaeal isoprenoid tetraether lipids: Implications for past sea surface temperature reconstructions. *Geochimica Et Cosmochimica Acta*, 74(16):4639–4654.

Kolattukudy, P. J. L. (1970). Plant waxes. 5(2):259–275.

Kukla, G. and An, Z. (1989). Loess stratigraphy in central china. *Palaeogeography, Palaeoclimatology, Palaeoecology*, 72:203–225.

Lear, C. H., Bailey, T. R., Pearson, P. N., Coxall, H. K., and Rosenthal, Y. (2008). Cooling and ice growth across the eocene-oligocene transition. *Geology*, 36(3):251–254.

Li, B. and Zhu, L. (2001). "greatest lake period" and its palaeo-environment on the tibetan plateau. *Journal of Geographical Sciences*, 11(1):34–42.

Li, G., Pettke, T., and Chen, J. (2011a). Increasing nd isotopic ratio of asian dust indicates progressive uplift of the north tibetan plateau since the middle miocene. *Geology*, 39(3):199–202.

Li, G., Rao, Z., Duan, Y., Xia, D., Wang, L., Madsen, D. B., Jia, J., Wei, H., Qiang, M., Chen, J., and Chen, F. (2016). Paleoenvironmental changes recorded in a luminescence dated loess/paleosol sequence from the tianshan mountains,

arid central asia, since the penultimate glaciation. *Earth and Planetary Science Letters*, 448:1–12.

Li, L., Fan, M., Davila, N., Jesmok, G., Mitsunaga, B., Tripati, A., and Orme, D. (2018). Carbonate stable and clumped isotopic evidence for late eocene moderate to high elevation of the east-central tibetan plateau and its geodynamic implications. *Geological Society of America Bulletin*.

Li, L. and Garzione, C. N. (2017). Spatial distribution and controlling factors of stable isotopes in meteoric waters on the tibetan plateau: Implications for paleoelevation reconstruction. *Earth and Planetary Science Letters*, 460:302–314.

Li, X., Zhao, K., Dodson, J., and Zhou, X. (2011b). Moisture dynamics in central asia for the last 15 kyr: new evidence from yili valley, xinjiang, nw china. *Quaternary Science Reviews*, 30(23-24):3457–3466.

Liu, X., Lipp, J. S., and Hinrichs, K.-U. (2011). Distribution of intact and core gdgts in marine sediments. *Organic Geochemistry*, 42(4):368–375.

Liu, Z., He, Y., Jiang, Y., Wang, H., Liu, W., Bohaty, S. M., and Wilson, P. A. (2018). Transient temperature asymmetry between hemispheres in the palaeogene atlantic ocean. *Nature Geoscience*, 11(9):656–+.

Liu, Z., Pagani, M., Zinniker, D., DeConto, R., Huber, M., Brinkhuis, H., Shah, S. R., Leckie, R. M., and Pearson, A. (2009). Global cooling during the eocene-oligocene climate transition. *Science*, 323(5918):1187–1190.

members, C. (1988). Climatic changes of the last 18,000 years: observations and model simulations. *Science*, pages 1043–1052.

Miller, K. G., Browning, J. V., Aubry, M. P., Wade, B. S., Katz, M. E., Kulpecz, A. A., and Wright, J. D. (2008). Eocene-oligocene global climate and sea-level changes: St. stephens quarry, alabama. *Geological Society of America Bulletin*, 120(1-2):34–53.

Mix, A. C., Bard, E., and Schneider, R. (2001). Environmental processes of the ice

age: land, oceans, glaciers (epilog). *Quaternary Science Reviews*, 20(4):627–657.

Mo, K. C. and Schemm, J. E. (2008). Relationships between enso and drought over the southeastern united states. *Geophysical Research Letters*, 35(15).

Molnar, P., Boos, W. R., and Battisti, D. S. (2010). Orographic controls on climate and paleoclimate of asia: thermal and mechanical roles for the tibetan plateau. *Annual Review of Earth and Planetary Sciences*, 38:77–102.

Oboh-Ikuenobe, F. E. and Jaramillo, C. A. J. F. G. t. I. T. M. E.-O. T. (2003). Palynological patterns in the uppermost eocene to lower oligocene sedimentary. page 269.

Ogg, J. G., Ogg, G., and Gradstein, F. M. (2016). *A concise geologic time scale: 2016*. Elsevier.

O'Leary, M. H. (1988). Carbon isotopes in photosynthesis. *Bioscience*, 38(5):328–336.

Oleson, K. W., Lawrence, D. M., Gordon, B., Flanner, M. G., Kluzek, E., Peter, J., Levis, S., Swenson, S. C., Thornton, E., and Feddema, J. (2010). *Technical description of version 4.0 of the Community Land Model (CLM)*.

Pagani, M., Huber, M., Liu, Z., Bohaty, S. M., Henderiks, J., Sijp, W., Krishnan, S., and DeConto, R. M. (2011). The role of carbon dioxide during the onset of antarctic glaciation. *Science*, 334(6060):1261–1264.

Pearson, P. N., Foster, G. L., and Wade, B. S. (2009). Atmospheric carbon dioxide through the eocene-oligocene climate transition. *Nature*, 461(7267):1110–U204.

Peltier, W. R., Argus, D. F., and Drummond, R. (2015). Space geodesy constrains ice age terminal deglaciation: The global ice-$6g_c(vm5a)model. Journal of Geophysical Research : Solid Earth, 120(1) : 450 – –487.$

Plancq, J., Mattioli, E., Pittet, B., Simon, L., and Grossi, V. (2014). Productivity

and sea-surface temperature changes recorded during the late eocene–early oligocene at dsdp site 511 (south atlantic). *Palaeogeography, Palaeoclimatology, Palaeoecology*, 407:34–44.

Polissar, P. J., Freeman, K. H., Rowley, D. B., McInerney, F. A., and Currie, B. S. (2009). Paleoaltimetry of the tibetan plateau from d/h ratios of lipid biomarkers. *Earth and Planetary Science Letters*, 287(1-2):64–76.

Porter, S. C. and An, Z. (1995). Correlation between climate events in the north atlantic and china during the last glaciation. *Nature*, 375(6529):305.

Prahl, F. G. and Wakeham, S. G. (1987). Calibration of unsaturation patterns in long-chain ketone compositions for palaeotemperature assessment. *Nature*, 330(6146):367.

Pullen, A., Kapp, P., McCallister, A. T., Chang, H., Gehrels, G. E., Garzione, C. N., Heermance, R. V., and Ding, L. (2011). Qaidam basin and northern tibetan plateau as dust sources for the chinese loess plateau and paleoclimatic implications. *Geology*, 39(11):1031–1034.

Rao, Z., Chen, F., Cheng, H., Liu, W., Wang, G., Lai, Z., and Bloemendal, J. (2013). High-resolution summer precipitation variations in the western chinese loess plateau during the last glacial. *Sci Rep*, 3:2785.

Rao, Z., Jia, G., Qiang, M., and Zhao, Y. (2014). Assessment of the difference between mid-and long chain compound specific δdn-alkanes values in lacustrine sediments as a paleoclimatic indicator. *Organic Geochemistry*, 76:104–117.

Rohrmann, A., Heermance, R., Kapp, P., and Cai, F. (2013). Wind as the primary driver of erosion in the qaidam basin, china. *Earth and Planetary Science Letters*, 374:1–10.

Sachse, D., Billault, I., Bowen, G. J., Chikaraishi, Y., Dawson, T. E., Feakins, S. J., Freeman, K. H., Magill, C. R., McInerney, F. A., van der Meer, M. T. J., Polissar, P., Robins, R. J., Sachs, J. P., Schmidt, H.-L., Sessions, A. L., White, J. W. C., West, J. B., and Kahmen, A. (2012). Molecular paleohydrology: Interpreting the hydrogen-isotopic composition of lipid biomarkers from photosynthesizing or-

ganisms. *Annual Review of Earth and Planetary Sciences*, 40(1):221–249.

Sawada, K., Handa, N., Shiraiwa, Y., Danbara, A., and Montani, S. (1996). Long-chain alkenones and alkyl alkenoates in the coastal and pelagic sediments of the northwest north pacific, with special reference to the reconstruction of emiliania huxleyi and gephyrocapsa oceanica ratios. *Organic Geochemistry*, 24(8-9):751–764.

Schimmelmann, A., Sessions, A. L., and Mastalerz, M. (2006). Hydrogen isotopic (d/h) composition of organic matter during diagenesis and thermal maturation. *Annual Review of Earth and Planetary Sciences*, 34:501–533.

Schouten, S., Hopmans, E. C., Schefuss, E., and Damste, J. S. S. (2002). Distributional variations in marine crenarchaeotal membrane lipids: a new tool for reconstructing ancient sea water temperatures? *Earth and Planetary Science Letters*, 204(1-2):265–274.

Sessions, A. L., Sylva, S. P., Summons, R. E., and Hayes, J. M. (2004). Isotopic exchange of carbon-bound hydrogen over geologic timescales 1 1associate editor: J. horita. *Geochimica et Cosmochimica Acta*, 68(7):1545–1559.

Shakun, J. D., Clark, P. U., He, F., Marcott, S. A., Mix, A. C., Liu, Z., Otto-Bliesner, B., Schmittner, A., and Bard, E. (2012). Global warming preceded by increasing carbon dioxide concentrations during the last deglaciation. *Nature*, 484(7392):49–54.

Sheldon, N. D., Grimes, S. T., Hooker, J. J., Collinson, M. E., Bugler, M. J., Hren, M. T., Price, G. D., and Sutton, P. A. (2016). Coupling of marine and continental oxygen isotope records during the eocene-oligocene transition. *Geological Society of America Bulletin*, 128(3-4):502–510.

Shi, Y., Yu, G., Liu, X., Li, B., and Yao, T. (2001). Reconstruction of the 30–40kabp enhanced indian monsoon climate based on geological records from the tibetan plateau. *Palaeogeography, Palaeoclimatology, Palaeoecology*, 169(1):69–83.

Slack, C. R. and Hatch, M. D. (1967). Comparative studies on the activity of carboxylases and other enzymes in relation to the new pathway of photosynthetic

carbon dioxide fixation in tropical grasses. *Biochemical Journal*, 103(3):660–665.

Sun, Y., Clemens, S. C., Morrill, C., Lin, X., Wang, X., and An, Z. (2012). Influence of atlantic meridional overturning circulation on the east asian winter monsoon. *Nature Geoscience*, 5(1):46.

Thomas, E. K., Huang, Y., Clemens, S. C., Colman, S. M., Morrill, C., Wegener, P., and Zhao, J. (2016). Changes in dominant moisture sources and the consequences for hydroclimate on the northeastern tibetan plateau during the past 32 kyr. *Quaternary Science Reviews*, 131:157–167.

Thompson, L. G., Yao, T., Davis, M. E., Henderson, K. A., MosleyThompson, E., Lin, P. N., Beer, J., Synal, H. A., ColeDai, J., and Bolzan, J. F. (1997). Tropical climate instability: The last glacial cycle from a qinghai-tibetan ice core. *Science*, 276(5320):1821–1825.

Thompson, L. o., Mosley-Thompson, E., Davis, M., Bolzan, J., Dai, J., Yao, T., Gundestrup, N., Wu, X., Klein, L., and Xie, Z. (1989). Holocene-late pleistocene climatic ice core records from qinghai-tibetan plateau. *Science*, 246(4929):474–477.

Tian, L., Masson-Delmotte, V., Stievenard, M., Yao, T., and Jouzel, J. (2001). Tibetan plateau summer monsoon northward extent revealed by measurements of water stable isotopes. *Journal of Geophysical Research: Atmospheres*, 106(D22):28081–28088.

Tian, L., Yao, T., Schuster, P. F., White, J. W. C., Ichiyanagi, K., Pendall, E., Pu, J., and Wu, Y. (2003). Oxygen-18 concentrations in recent precipitation and ice cores on the tibetan plateau. *Journal of Geophysical Research-Atmospheres*, 108(D9).

Tierney, J., Zhu, J., King, J., Malevich, S. B., Hakim, G., and Poulsen, C. (2019). Glacial cooling and climate sensitivity revisited.

Tierney, J. E. and Tingley, M. P. (2014). A bayesian, spatially-varying calibration model for the tex86 proxy. *Geochimica Et Cosmochimica Acta*, 127:83–106.

Tipple, B. J., Meyers, S. R., and Pagani, M. (2010). Carbon isotope ratio of cenozoic

co2: A comparative evaluation of available geochemical proxies. *Paleoceanography*, 25(3).

Tipple, B. J. and Pagani, M. (2007). The early origins of terrestrial c4 photosynthesis. *Annu. Rev. Earth Planet. Sci.*, 35:435–461.

Tipple, B. J. and Pagani, M. (2010). A 35myr north american leaf-wax compound-specific carbon and hydrogen isotope record: implications for c 4 grasslands and hydrologic cycle dynamics. *Earth and Planetary Science Letters*, 299(1):250–262.

Toggweiler, J. R. and Russell, J. (2008). Ocean circulation in a warming climate. *Nature*, 451(7176):286–288.

Torfstein, A., Goldstein, S. L., Stein, M., and Enzel, Y. (2013). Impacts of abrupt climate changes in the levant from last glacial dead sea levels. *Quaternary Science Reviews*, 69:1–7.

Tremblin, M., Hermoso, M., and Minoletti, F. (2016). Equatorial heat accumulation as a long-term trigger of permanent antarctic ice sheets during the cenozoic. *Proc Natl Acad Sci U S A*, 113(42):11782–11787.

Vachon, R. W., Welker, J. M., White, J. W. C., and Vaughn, B. H. (2010). Monthly precipitation isoscapes (delta o-18) of the united states: Connections with surface temperatures, moisture source conditions, and air mass trajectories. *Journal of Geophysical Research-Atmospheres*, 115.

Volkman, J. K., Barrerr, S. M., Blackburn, S. I., and Sikes, E. L. (1995). Alkenones in gephyrocapsa oceanica: Implications for studies of paleoclimate. *Geochimica et Cosmochimica Acta*, 59(3):513–520.

Volkman, J. K., Eglinton, G., CoRNER, E. D., and Forsberg, T. (1980). Long-chain alkenes and alkenones in the marine coccolithophorid emiliania huxleyi. *Phytochemistry*, 19(12):2619–2622.

Wade, B. S., Houben, A. J. P., Quaijtaal, W., Schouten, S., Rosenthal, Y., Miller, K. G., Katz, M. E., Wright, J. D., and Brinkhuis, H. (2012). Multiproxy record of abrupt sea-surface cooling across the eocene-oligocene transition in the gulf

of mexico. *Geology*, 40(2):159–162.

Wade, B. S. and Pearson, P. N. (2008). Planktonic foraminiferal turnover, diversity fluctuations and geochemical signals across the eocene/oligocene boundary in tanzania. *Marine Micropaleontology*, 68(3-4):244–255.

Wang, C. Z. and Enfield, D. B. (2001). The tropical western hemisphere warm pool. *Geophysical Research Letters*, 28(8):1635–1638.

Wang, N., Jiang, D., and Lang, X. (2018). Northern westerlies during the last glacial maximum: Results from cmip5 simulations. *Journal of Climate*, 31(3):1135–1153.

Wang, Y., Cheng, H., Edwards, R. L., Kong, X., Shao, X., Chen, S., Wu, J., Jiang, X., Wang, X., and An, Z. (2008). Millennial-and orbital-scale changes in the east asian monsoon over the past 224,000 years. *Nature*, 451(7182):1090.

Wang, Y., Herzschuh, U., Shumilovskikh, L. S., Mischke, S., Birks, H. J. B., Wischnewski, J., Böhner, J., Schlütz, F., Lehmkuhl, F., Diekmann, B., Wünnemann, B., and Zhang, C. (2014). Quantitative reconstruction of precipitation changes on the ne tibetan plateau since the last glacial maximum ndash; extending the concept of pollen source area to pollen-based climate reconstructions from large lakes. *Climate of the Past*, 10(1):21–39.

Wang, Z. and Liu, W. (2012). Calibration of the u 37 k index of long-chain alkenones with the in-situ water temperature in lake qinghai in the tibetan plateau. *Chinese Science Bulletin*, 58(7):803–808.

Wang, Z., Liu, W., Liu, Z., Wang, H., He, Y., and Zhang, F. (2013). A 1700-year n-alkanes hydrogen isotope record of moisture changes in sediments from lake sugan in the qaidam basin, northeastern tibetan plateau. *The Holocene*, 23(9):1350–1354.

Webster, P. J., Magana, V. O., Palmer, T., Shukla, J., Tomas, R., Yanai, M., and Yasunari, T. (1998). Monsoons: Processes, predictability, and the prospects for prediction. *Journal of Geophysical Research: Oceans*, 103(C7):14451–14510.

Weijers, J. W. H., Schouten, S., Spaargaren, O. C., and Damste, J. S. S. (2006). Occurrence and distribution of tetraether membrane lipids in soils: Implications for the use of the tex86 proxy and the bit index. *Organic Geochemistry*, 37(12):1680–1693.

Wu, G., Liu, Y., He, B., Bao, Q., Duan, A., and Jin, F.-F. (2012). Thermal controls on the asian summer monsoon. *Scientific reports*, 2:404.

Yang, B., Shi, Y., Braeuning, A., and Wang, J. (2004). Evidence for a warm-humid climate in arid northwestern china during 40–30 ka bp. *Quaternary Science Reviews*, 23(23-24):2537–2548.

Yao, T., Masson-Delmotte, V., Gao, J., Yu, W., Yang, X., Risi, C., Sturm, C., Werner, M., Zhao, H., and He, Y. (2013). A review of climatic controls on δ18o in precipitation over the tibetan plateau: Observations and simulations. *Reviews of Geophysics*, 51(4):525–548.

Yao, T., Thompson, L., Yang, W., Yu, W., Gao, Y., Guo, X., Yang, X., Duan, K., Zhao, H., Xu, B., Pu, J., Lu, A., Xiang, Y., Kattel, D. B., and Joswiak, D. (2012). Different glacier status with atmospheric circulations in tibetan plateau and surroundings. *Nature Climate Change*, 2(9):663–667.

Yu, G., Xue, B., Liu, J., and Chen, X. (2003). Lgm lake records from china and an analysis of climate dynamics using a modelling approach. *Global and Planetary Change*, 38(3-4):223–256.

Zanazzi, A., Kohn, M. J., MacFadden, B. J., and Terry, Dennis O., J. (2007). Large temperature drop across the eocene-oligocene transition in central north america. *Nature*, 445(7128):639–642.

Zhang, H.-C., Fan, H., Chang, F.-Q., Zhang, W.-X., Lei, G., Yang, M., Lei, Y., and Yang, L. (2008). Ams dating on the shell bar section from qaidam basin, ne tibetan plateau, china. *Radiocarbon*, 50(2):255–265.

Zhang, R. and Delworth, T. L. (2005). Simulated tropical response to a substantial weakening of the atlantic thermohaline circulation. *Journal of Climate*, 18(12):1853–1860.

Zhang, X., Xu, B., Günther, F., Mügler, I., Lange, M., Zhao, H., Li, J., and Gleixner, G. (2017). Hydrogen isotope ratios of terrestrial leaf wax n-alkanes from the tibetan plateau: controls on apparent enrichment factors, effect of vapor sources and implication for altimetry. *Geochimica et Cosmochimica Acta*.

Zhang, Y. G., Pagani, M., and Wang, Z. (2016). Ring index: A new strategy to evaluate the integrity of tex86paleothermometry. *Paleoceanography*, 31(2):220–232.

Zhang, Y. G., Zhang, C. L. L., Liu, X. L., Li, L., Hinrichs, K. U., and Noakes, J. E. (2011). Methane index: A tetraether archaeal lipid biomarker indicator for detecting the instability of marine gas hydrates. *Earth and Planetary Science Letters*, 307(3-4):525–534.

Zhou, A.-f., Chen, F.-h., Wang, Z.-l., Yang, M.-l., Qiang, M.-r., and Zhang, J.-w. (2009). Temporal change of radiocarbon reservoir effect in sugan lake, northwest china during the late holocene. *Radiocarbon*, 51(2):529–535.

Zhu, J., Liu, Z., Brady, E., Otto-Bliesner, B., Zhang, J., Noone, D., Tomas, R., Nusbaumer, J., Wong, T., Jahn, A., and Tabor, C. (2017). Reduced enso variability at the lgm revealed by an isotope-enabled earth system model. *Geophysical Research Letters*, 44(13):6984–6992.

Zhuang, G., Brandon, M. T., Pagani, M., and Krishnan, S. (2014). Leaf wax stable isotopes from northern tibetan plateau: Implications for uplift and climate since 15 ma. *Earth and Planetary Science Letters*, 390:186–198.

Vita

Mingqiu Hou was born in Shandong, China. She majored in geology at China university of Petroleum (Beijing) and Missouri University of Science and Technology and earned her bachelor's degree in May 2016. She joined the Geology and Geophysics department at Louisiana State University to pursue her Ph.D. degree in geology in August 2016.

She was actively involved in academic activities during her program as a graduate student. Her research focus on the evolution of paleoclimate and paleoecology in Central Asia and North America during the Cenozoic period. She was an active member in the Geological Society of America (GSA), American Geophysical Union (AGU), and American Association of Petroleum Geologist (AAPG). She presented her research work at the AGU annual meeting in 2017, 2018, and 2019. She served as a graduate teaching assistant at Louisiana State University from 2016 to 2020.

She anticipates receiving her Ph.D. degree in Geology and Geophysics from Louisiana State University in May 2021.